Thèse présentée pour obtenir le grade de
Docteur de l'Université Louis Pasteur
Strasbourg I

Discipline : Physique nucléaire
par Antoine Bacquias

Kinematical properties of spectator fragments in heavy-ion collisions at relativistic energies

Soutenue publiquement le 31 juillet 2008

Membres du jury

Directeur de thèse : Fouad Rami, IPHC Strasbourg
Co-directeur de thèse : Karl-Heinz Schmidt, GSI Darmstadt
Rapporteur Interne : Florent Haas
Rapporteur Externe : Helmut Oeschler
Rapporteur Externe : José Benlliure
Président du jury : Jerzy Dudek
Examinateur : Bertram Blank

Thanks

Dans quelle langue écrit-on les remerciements d'une thèse française écrite en anglais et effectuée au fin fond (si, si) de la campagne allemande ? Je n'en sais rien, alors on va panacher.

Je tiens tout d'abord à remercier les membres du jury, dont on trouve la liste sur la première page de ce document. Pour avoir eu la gentillesse d'écourter/modifier les vacances pour venir m'écouter présenter ce travail, pour l'effort de compréhension parfois induit par la langue et en tous cas pour avoir pris le temps de s'immerger dans mon domaine afin de me conseiller et confronter mes idées à d'autres opinions.

Un grand merci à Fouad Rami pour avoir conduit cet effort avec attention. La perspective depuis un domaine de physique complémentaire aura, je pense, été profitable. Outre les discussions concernant le manuscrit, je vous suis grandement reconnaissant pour m'avoir poussé à répéter et peaufiner l'exposé oral. Il est toujours important de savoir se faire comprendre et argumenter clairement ; vous m'y avez soigneusement préparé dans ces derniers jours fébriles de juillet.

Le guidage du travail a été effectué localement par Karl-Heinz Schmidt. Merci d'avoir su me transmettre un enthousiasme constructif dans le développement des idées. L'intuition d'un directeur de thèse est un puissant moteur pour le thésard qui débute, et un soutient fort appréciable tout au long du doctorat. Que ce soit autour d'un café dans le foyer de GSI ou sur le balcon à Erzhausen (le boulot à l'ombre du bouleau, un classique qui a fait ses preuves), les discussions m'ont toujours aidé, inspiré et éclairci dans un domaine où les idées foisonnent. Nochmal, ich bedanke mich.

Now, technically, every one knows that the boss of a group does not always show up, and that the technical support of every days ' life comes from post-docs. They come, they go, they sometimes obtain a permanent position, but they are always keen on giving advice to the novice. Aleksandra and Valentina, I thank you a lot. For pushing me and sometimes unsuccessfully trying to force me into presentations of my work; I may have played a bit with your nerves, but it never resulted in a fight, so I guess we were all conscious of the benefits of the stress inside the phd student. Thanks also for the kind discussions; about the thesis of course, with advice on the manuscript for example, but for the chit-chat as well (that one could actually play "boules" without drinking pastis, or that one could survive in the world of physics having children were some of the teaching you got me through).

I don't forget the post-docs that passed by during my stay (Strahinja -who brought us to badminton-, Lydie -who showed me the comic strip that enlighted all the mournful Thursday mornings: "piled, higher and deeper"-, Radek, Pavel...). This period almost did not overlap with the thesis of the couple Henzlovi, but they opened a way that led to my thesis, so I thank them as well.

Dear Ville, if you read this, you must be really desperately looking for something to distract your mind from the bloody data analysis or for delaying the writing of your own

Contents

List of Figures

List of Tables

Résumé

La matière nucléaire constitue l'essentiel de notre environnement. Pourtant, ses propriétés statiques et dynamiques, reliées dans son équation d'état (EoS), sont encore mal définies. Hormis l'observation d'objets célestes, l'étude de la matière nucléaire en laboratoire nécessite la collision de noyaux atomiques à diverses énergies selon l'aspect que l'on cherche à déterminer. Pour notre travail, nous nous plaçons dans le cadre d'énergies relativistes ; les données que nous utiliserons pour notre étude proviennent des résidus spectateurs de la réaction ^{136}Xe+Pb à une énergie de 1 GeV par nucléon. Etant bien au-delà de l'énergie de Fermi (aux alentours de 40 MeV), les effets collectifs entre constituants des noyaux sont réduits ; cela permet de déduire des propriétés générales de la matière nucléaire infinie, à partir des observations. Or, certains théoriciens prédisent une sensibilité des observables dynamiques des fragments spectateurs à la section efficace nucléon-nucléon [SDL01]. D'autre part, la multifragmentation des résidus spectateurs, qui semble être la signature d'une transition de phase de la matière nucléaire, est un processus complexe, et dont les influences sur la cinématique des fragments sont encore mal comprises. Nous nous proposons donc d'explorer les propriétés cinématiques des fragments spectateurs avec le plus de précision possible et pour un grand nombre de fragments, avec deux buts fondamentaux : faire de nos données de qualité une information comparable et utilisable par les modèles théoriques pour étudier la section efficace nucléon-nucléon ; caractériser les mécanismes de réaction, et notamment la multifragmentation. Notre étude présente également un intérêt pour des applications techniques (spécification de faisceaux secondaires, évaluation de dommages dans la cible de spallation de réacteurs hybrides).

Dans un premier temps, nous définirons le langage propre à notre domaine de recherche, et les mécanismes de réactions en jeu dans les collisions d'ions lourds aux énergies relativistes. L'abrasion constitue la première étape de formation des fragments. La géométrie de la collision, décrite par le paramètre d'impact, conditionne cette phase. La coupure engendrée par ce processus définit le fragment spectateur par rapport à la zone participante, correspondant au recouvrement des trajectoires des nucléons du projectile et de la cible. L'abrasion induit une énergie d'excitation dans le fragment spectateur. Cette énergie est donc disponible pour les étapes suivantes d'évolution du fragment. L'émission séquentielle de nucléons, de noyaux légers, voire de fragments de masse intermédiaire (IMFs), mais aussi la fission, constituent une étape importante de perte de masse. Nous verrons que la modélisation de l'émission séquentielle d'IMFs peut-être faite sur la base d'une évaporation ou d'une fission très asymétrique, sans grande incidence pour le système que nous nous proposons de prendre comme référence, à savoir le xénon ^{136}Xe. Dans les réactions

ayant induit une énergie d'excitation suffisante, le spectateur issu de l'abrasion se morcelle, donnant lieu à l'observation simultanée de plusieurs fragments de masse modeste. Parce qu'il est similaire à une transition de phase, ce régime d'évolution du fragment est d'intérêt primordial pour établir l'EoS de la matière nucléaire. Ce processus, pourtant largement étudié, est encore méconnu ; diverses hypothèses sont formulées pour le décrire, notamment dans son influence sur la cinématique des produits de multifragmentation.

Les données choisies pour cette étude ont été obtenues auprès du séparateur de fragments de GSI, à Darmstadt. Ce complexe accélérateur est détaillé, depuis la source d'ions utilisée lors de l'expérience, les cavités accélératrices et l'accélérateur linéaire UNILAC, jusqu'au synchrotron SIS18 et à ses spécificités techniques.

Notre principal outil, le séparateur de fragments FRS est présenté tout d'abord de façon générale. Le principe d'identification par temps de vol, rigidité magnétique et perte d'énergie, ainsi que la mesure de haute précision des vitesses longitudinales des fragments seront exposées. Chaque détecteur est décrit et son rôle est spécifié.

Les données étudiées et principalement utilisées pour la discussion physique sont issues d'une expérience ^{136}Xe+Pb à une énergie d'1 GeV par nucléon. Cette expérience fût réalisée en 2004 ; les sections efficaces de production des fragments ont été déterminées dans une étude précédente [Hen05b]. Notre étude connaît des exigences plus grandes quant à la précision des mesures. Ainsi, les diverses sources d'imprécisions seront envisagées. Leurs contributions dans les spectres en vitesse longitudinale seront évaluées. Même si les corrections à appliquer sont mineures et seront pour la plupart négligées, cette vérification s'impose pour s'assurer de la validité et de la qualité de nos données.

Les distributions en vitesse longitudinales, que nous présenterons systématiquement dans le repère du faisceau (dont la vitesse dans le repère du laboratoire est de l'ordre de 26 cm/ns) sont caractérisées par diverses quantités. Nous avons choisi de présenter les principaux moments des distributions, pour tous les fragments identifiés dans le FRS : valeur moyenne, écart-type et le coefficient d'asymétrie. Nous proposons donc des quantités objectives, libres de toute interprétation, à partir des spectres bruts tels qu'ils sont obtenus à la suite de la coupure en acceptance du FRS. Cette "matière première" pourra servir pour contraindre des modèles théoriques reproduisant les conditions spécifiques du FRS, selon l'interprétation propre à l'utilisateur. Une discussion qualitative sur ces mesures brutes terminera ce chapitre, soulignant que la valeur moyenne, la largeur et le degré d'asymétrie des spectres semblent décorrélés. Diverses méthodes d'ajustement de la forme des spectres par des distributions Gaussiennes seront testées. Nous verrons qu'alors que les fragments les plus lourds peuplent une simple distribution Gaussienne, les fragments les plus légers ont une distribution en vitesse qui dévie de cette distribution Gaussienne. Un simple ajustement, même multi-gaussien ne peut être satisfaisant pour comprendre la forme de ces spectres et en extraire des quantités physiques correctement attribuées à différents mécanismes de réaction. Ainsi, la nécessité d'une interprétation de la forme globale des spectres apparaît évidente.

Les fragments de masse proche de celle du projectile, qui sont donc les fragments les plus lourds observés dans l'expérience, suivent une distribution en vitesse longitudinale à caractère gaussien. Il n'y a là rien de surprenant ; par le théorème de la limite centrale,

nous savons que tout processus statistique donc chaque mesure est indépendante, tend à suivre, pour un grand nombre de mesures, une distribution gaussienne. Nous pouvons donc simplement conclure qu'il y a un processus dominant de formation des résidus lourds, que celui-ci connaît une fluctuation et qu'il n'est pas d'autre contribution de magnitude comparable qui entre en jeu dans la formation de ces résidus lourds et dans l'attribution de leur vitesse.

Il en va autrement pour les résidus légers. La forme des spectres est asymétrique et peut-être reproduite par chevauchement de deux gaussiennes. Toutefois, cet ajustement ne s'appuye sur aucune déduction physique et ne peut prétendre à la reproduction de mécanismes de réactions connus et identifiés. Au lieu de cela, nous proposons de tirer les enseignements d'autres expériences effectuées avec le FRS et dont les données présentent des similitudes avec celles que nous considérons. Dans les données obtenues auprès du FRS, la fission se traduit par la présence de deux pics dans les spectres en vitesse longitudinale : à partir de la séparation entre deux produits de fission, la répulsion coulombienne les repousse mutuellement, leur donnant une accélération dans deux directions opposées. Le phénomène, s'il est isotropique, conduit, après convolution avec l'acceptance du FRS (un mince cylindre est transmis) et projection sur une dimension, à l'apparition de deux pics, bien séparés en vitesse si aucun autre processus ne s'y ajoute. Cet effet est observé depuis longtemps dans le cas de la fission symétrique, mais les produits concernés sont bien plus lourds que dans notre cas. Les produits de fission asymétrique présentent également cette caractéristique, comme l'a montré par exemple l'étude menée par V. Ricciardi [RAB+06]. Toutefois, le xenon présente une barrière de fission beaucoup plus haute que l'énergie de séparation du neutron, contrairement à l'uranium, pour lequel ces deux quantités sont comparables. Néanmoins, avec l'augmentation en énergie d'excitation du préfragment issu de l'étape d'abrasion, les canaux de désexcitation par évaporation accessibles deviennent plus nombreux, et l'évaporation de noyaux de masse intermédiaire (IMF) n'est pas négligeable. Que l'on conçoive ce processus comme une évaporation d'IMF ou comme une fission très asymétrique n'a pas grande incidence sur nos observables dans le cas du xenon. Quoiqu'il en soit, ces évènements binaires conduisent à l'apparition de deux pics dans les distributions en vitesse longitudinale, ou en tous cas au peuplement d'une sphère dans l'espace des vitesses, une fois de plus par la répulsion coulombienne. Cette répulsion affecte principalement le partenaire léger de ce type de décroissance.

En effet, deux "bosses" sont bien visibles dans les données analysées par P. Napolitani de l'expérience ^{136}Xe+p à 1 GeV par nucléon [NSTG+07]. L'explication proposée est effectivement la décroissance binaire du préfragment issu de l'abrasion, la répulsion coulombienne donnant à la vitesse du fragment léger ces vitesses extrêmes. Pourtant, dans le cas de la cible de plomb, les formes des spectres ne sont pas aussi claires. Les données des expériences du détecteur à grande acceptance ALADiN sont cruciales pour la compréhension et la discussion de nos observations. En effet, les informations accumulées sur la multiplicité des fragments et leur masse dans des expériences comparables indiquent la transition entre deux états de la matière nucléaire composant les fragments spectateurs. Les mesures montrent qu'au-delà d'une certaine température critique atteinte par le préfragment (à relier avec la centralité de la collision et la magnitude du processus

d'abrasion), l'énergie d'excitation disponible est consumée sous forme d'expansion volumique du système de nucléons et dans la formation de multiples fragments. Pour les collisions relativement centrales ou semi-périphériques, la décroissance du préfragment en plusieurs fragments est la plus probable et conduit à des fragments de masses faibles ou intermédiaires.

Nous interprétons donc nos observations comme la superposition de deux processus de formation des fragments légers : d'une part la décroissance binaire asymétrique, où la répulsion coulombienne joue un rôle majeur, d'autre part la multifragmentation, dont les produits sont trop nombreux pour engendrer un effet dominant sur leur vitesse et peuplant donc une distribution gaussienne. Dans le cas de la cible d'hydrogène, l'énergie d'excitation induite n'est vraisemblablement pas suffisante pour engendrer la multifragmentation du système de nucléons. Les processus binaires sont la principale contribution aux spectres mesurés. Au contraire, la collision du xenon avec un noyau de plomb induit pour les collisions suffisamment centrales assez d'énergie d'excitation pour former plusieurs fragments. L'acceptance limitée de notre dispositif expérimental fait que la composante multifragmentation est mieux transmise à travers le spectromètre que la sphère coulombienne. Ainsi, la distribution liée à l'émission binaire de fragments légers est masquée par le pic gaussien dû à la multifragmentation. Toutefois, ces deux contributions ne semblent pas avoir la même vitesse moyenne, et l'un des deux pics coulombiens pourrait expliquer l'asymétrie marquée visible dans les spectres mesurés.

Nous verrons dans une discussion finale que ces aspects d'apparence simple constituent une trace unique de la centralité des évènements. Les produits légers de décroissance binaire sont distribués autour d'une valeur moyenne (centre de la sphère) qui reflète le recul du partenaire lourd. Or, nous verrons dans le chapitre suivant qu'il est possible de lier la vitesse d'un fragment lourd, et sa masse, au paramètre d'impact de la collision. Il ressortira que les fragments légers issus de processus binaires sont issus de collisions peu énergétiques et donc dans notre cas périphériques. Les produits de la multifragmentation quant-à-eux sont caractéristiques de réactions plus centrales.

Dans un article théorique, L. Shi et al. [SDL01] soulignent que le freinage des fragments spectateurs dans les collisions d'ions lourds dépend de l'interaction nucléon-nucléon lors de la première phase de la réaction, l'abrasion. La mesure de ce ralentissement des résidus par rapport à la vitesse initiale des ions entrant en collision permet donc en principe de contraindre la section efficace nucléon-nucléon en milieu nucléaire (*in-medium N-N cross-section*). Le FRS, offrant une grande précision dans la mesure de la vitesse longitudinale des fragments constitue donc un outil de choix pour fournir des données de qualité vis-à-vis de cet aspect fondamental.

Les modèles dynamiques de collisions nucléaires tels que BUU ou QMD sont délicats à coupler avec un code de désexcitation des préfragments, notamment parce que l'énergie acquise par les spectateurs durant l'étape d'abrasion est difficile à déterminer. En effet, chaque nucléon étant modélisé, la distinction entre nucléons participants et nucléons spectateurs n'est pas évidente. Or, un nucléon participant -donc de haute énergie- mal attribué contribuera grandement à l'excitation "artificielle" d'un fragment spectateur. Pour cette raison, il serait profitable de disposer de données qui ne dépendent pas de la phase

de désexcitation, ou de pouvoir exprimer nos observables en fonction d'une quantité liée seulement aux premiers instants de la collision : le paramètre d'impact.

Pour les collisions périphériques, l'abrasion engendre une énergie d'excitation sous le seuil critique pour la multifragmentation. Elle n'est donc suivie que par l'évaporation de particules légères, protons, neutrons, alpha... Cette excitation induite est déterminée par le nombre de nucléons arrachés lors de l'abrasion. A chaque nucléon arraché, l'énergie du spectateur augmente et les canaux préférentiels de désexcitation sont modifiés. Pour cette région en masse proche de celle du projectile, nous pouvons considérer que la masse perdue par abrasion détermine de manière unique la masse du fragment final. En d'autre termes, il est raisonnable de supposer que pour un paramètre d'impact donné (assez grand pour que la collision reste périphérique), la distribution en masse des fragments finaux est très étroite. Dans cette hypothèse, la masse arrachée par abrasion peut-être déterminée par des critères géométriques. Le modèle de Glauber [Gla59] permet de calculer la section efficace de production des préfragments en fonction du paramètre d'impact. En comparant la section efficace mesurée dans notre expérience pour le fragment le plus lourd avec la section intégrée de Glauber sur un intervalle extrême de paramètre d'impact, nous attribuerons un paramètre d'impact moyen conduisant à ce fragment final de masse donnée. La procédure étant réitérée pour la masse inférieure voisine, nous construirons pas-à-pas une dépendance moyenne de la masse du fragment final en fonction du paramètre d'impact de la collision.

Cette relation sera exploitée pour exprimer les vitesses moyennes longitudinales des fragments observés dans l'expérience en fonction du paramètre d'impact, les rendant plus aisément comparables avec les prédictions de modèles théoriques.

Il est également intéressant de s'intéresser à la largeur des distributions en vitesse ou en impulsion de fragments observés. La dispersion cinématique des produits de fragmentation joue un rôle déterminant dans la conception des installations à faisceau secondaire. En effet, le transport des produits de réaction doit être optimisé en fonction de l'émittance du faisceau obtenu ; cette émittance est directement liée à la dispersion cinématique des fragments produits lors de la collision. Le principe de fragmentation étant également à la base des réacteurs nucléaires hybrides (ADS), la dispersion en impulsion des fragments participe à la dégradation de la cible de spallation.

Outre ces aspects techniques, la largeur des spectres en vitesse ou en impulsion constitue une des observables disponibles dans les données accumulées auprès du FRS. Elle contribue avec la valeur moyenne à caractériser les distributions, et évolue avec la forme des spectres. La description de l'évolution de la largeur des spectres en fonction de la masse du fragment observé nécessite une grande compréhension des mécanismes de réaction en jeu et de leur influence sur la cinématique des fragments. Une telle étude possède donc un réel intérêt fondamental.

Plusieurs prédictions existent pour la déviation standard de l'impulsion des fragments. Morrissey [Mor89] a établi une systématique à partir de l'ensemble des données disponibles à cette époque. Cette formule ne s'appuie pas sur des considérations physiques ; elle est utilisable pour les collisions périphériques, produisant les fragments les plus lourds.

Le modèle de Goldhaber [Gol74] repose quant à lui sur le mouvement de Fermi des nucléons dans le projectile avant la phase d'abrasion. La déviation standard de l'impulsion

dans une dimension (longitudinale ou transverse) est liée à la perte de masse par abrasion, en fonction de la masse du projectile initiale ; l'impulsion de Fermi p_F entre explicitement dans la formule. Ce modèle reproduit qualitativement l'évolution de cette quantité en fonction de la masse du fragment. Pourtant, l'abrasion est un processus qui induit de l'énergie d'excitation dans le fragment spectateur ; cette énergie disponible favorise une perte de masse, via évaporation, fission ou multifragmentation. La formule de Goldhaber ne tient compte que du processus d'abrasion et ne peut être directement comparée aux données, puisqu'elle décrit la dispersion cinématique d'un préfragment (issu de l'abrasion).

Ainsi, les deux principales prédictions disponibles jusqu'à présent sont soit incomplètes dans un cas, ou ne reposent pas sur un modèle théorique dans l'autre. La nécessité de compiler les connaissances actuelles en termes de mécanismes de réaction nous pousse donc à établir un nouveau modèle pour décrire ces fluctuations dans la cinématique des fragments observés.

En préambule de cette discussion, nous résumerons les idées déjà avancées pour décrire notamment la cinématique des produits de multifragmentation. Le code de simulation SMM (Statistical Multifragmentation Model) [BBI+95] étant spécifiquement dédié au traitement de la multifragmentation, il offre plusieurs hypothèses qui serviront de base à la discussion. Ce modèle théorique part du principe que le système de nucléons entrant en phase de multifragmentation est thermalisé. Nous verrons que ce postulat n'est pas anodin, et peut être discuté. Le scénario opposé correspondrait à un morcellement très rapide du préfragment issu de l'abrasion, faisant du mouvement fermionique des nucléons la principale source de fluctuations cinématiques.

Les ingrédients de notre nouveau modèle sont les suivants. L'abrasion est décrite à la manière de Goldhaber, par une dispersion en impulsion en fonction de l'impulsion de Fermi et de la perte de masse engendrée par abrasion. Cette contribution à la dispersion cinématique est toujours ajoutée aux autres contributions. A la suite de l'abrasion, deux cas de figure peuvent se présenter: si l'énergie d'excitation est faible, le préfragment entre directement en phase d'évaporation (éventuellement fission) ; si l'énergie d'excitation induite est suffisante, le préfragment entre en phase de multifragmentation, avant de décroître par évaporation. La phase d'évaporation intervient dans les fluctuations cinématiques par son caractère séquentiel. Les nucléons et noyaux légers émis l'un après l'autre induisent un moment de recul du noyau mère. Ce recul est fonction de la charge de la particule émise, conditionnant son intéraction coulombienne avec le noyau émetteur, ainsi que du mouvement thermique au sein de ce noyau mère. La contribution issue de ce moment de recul est toujours présente en plus des fluctuations dues à la phase d'abrasion. Lors des collisions où l'énergie d'excitation acquise par le préfragment issu de l'abrasion est supérieure à un certain seuil, le système de nucléons entre en phase de multifragmentation. Nous présumons alors que le système réagit à cette augmentation d'énergie par une expansion volumique. Ceci se traduit par une diminution de l'impulsion de Fermi. Comme nous l'avons signalé plus haut, selon la rapidité du processus de morcellement, les produits de multifragmentation montreront un caractère thermal ou simplement un caractère fermionique dans leur cinématique. Nous appuyant sur un article de Bauer [Bau95], nous prendrons le mouvement thermique et le mouvement fermionique en considération

pour dresser une description complète de la dispersion cinématique des fragments. De plus, la répulsion coulombienne entre le fragment considéré et le noyau mère sera prise en compte, selon la prescription de Chung et al.[CDS87].

Après une présentation du code de simulation ABRABLA [GS91], nous discuterons succintement l'inclusion dans le code de la description de la cinématique des fragments que nous avons choisie. La simulation offre l'avantage de pouvoir contenir chaque mécanisme de réaction de façon détaillée. Elle est utile pour juger de l'importance des différents processus liés aux propriétés cinématiques des fragments, et estimer la pertinence des descriptions choisies, notamment en ce qui concerne l'influence de la multifragmentation sur la dispersion cinématique des fragments. Toutefois, pour les applications techniques, il est pratique d'établir une description analytique condensée, plus rapide à mettre en œuvre et facile à inclure dans un code optique qu'une simulation complète de type Monte-Carlo.

Les choix afférents à cette démarche seront détaillés. Les contributions de l'abrasion et de l'évaporation à la dispersion cinématique des fragments peuvent être formulées simplement, avec l'aide de peu de paramètres. L'influence de la multifragmentation est plus délicate à introduire. Pour calculer les contributions à la dispersion cinématique spécifiques de la multifragmentation, nous devons présumer de la nature (numéro atomique et masse) du noyau mère, au début de la phase de multifragmentation. Nous avons choisi de prendre systématiquement pour noyau mère le préfragment le plus massif issu de l'abrasion pouvant entrer en phase de multifragmentation. Les différents choix de description de la cinématique des produits de multifragmentation seront testés, et les résultats du modèle analytique établi seront comparés selon les valeurs des différents paramètres entrant dans la composition de ce modèle.

Les figures issues de cette discussion montrent une bonne capacité à reproduire les données pour une large gamme en masse.

Le bilan de notre étude des propriétés cinématiques des fragments spectateurs est positif. La combinaison des avantages spécifiques de notre dispositif expérimental, l'identification complète des fragments pour une large gamme en masse et la mesure précise de leur vitesse longitudinale sans seuil, a permis de proposer des données directement exploitables par les théoriciens, ouvrant la voie à une nouvelle approche de la section efficace nucléon-nucléon en milieu nucléaire. La détermination de cette dernière n'est pas immédiate ; les auteurs de codes dynamiques que nous avons contacté expriment des réserves quant à la précision numérique des versions actuelles de ces codes, principalement développés pour l'interprétation des expériences à grande acceptance mais faible résolution en vitesse.

La description globale (c'est-à-dire pour toute la gamme en masse observée) des mécanismes de réaction, et principalement leur dynamique, soutient parfaitement la comparaison avec les données disponibles et les effets cinématiques constatés. Cela valide notamment la grande influence du caractère fermionique des nucléons dans le noyau, non seulement dans la phase d'abrasion, mais aussi lors de la multifragmentation. L'expansion volumique et la thermalisation du système entrant en phase de multifragmentation sont également compatibles avec les observations.

La complémentarité de nos données avec les informations obtenues auprès de dispositifs à grande acceptance ouvre des perspectives prometteuses si des collaborations en ce sens

venaient à voir le jour.

Introduction

Nuclei are the most important constituents of our environment. It is therefore a very natural intellectual process to try to reach a deep comprehension of the properties of nuclear matter.

The properties of nuclear matter have determined the evolution of the universe after the big bang, at the time when it had cooled down enough so that the sub-nuclear degrees of freedom were frozen. They are also decisive for the processes occurring in the evolution of stars, from their ignition until their death. Supernova explosion and formation of neutron stars (even the conditions of their existence) are determined by some decisive properties of nuclear matter. For example, the incompressibility of nuclear matter is crucial for the determination of the largest mass a neutron star can have, before it collapses to a black hole.

The conditions of interest for astrophysics are extremely different from conditions of our immediate environment in terms of temperature, density and neutron-to-proton ratio.

Beside astrophysical observations, nuclear matter studies can take place in laboratories, under very different conditions. The unique tool at our disposal is the collision process of nuclei. Nuclei are far from the composition of neutron stars, but by choosing colliding nuclei with largely varying N/Z ratio, one may constrain theories on the role of this degree of freedom.

An important parameter for classifying these experiments is the energy per nucleon available in the centre of mass of the colliding system. Energies below about 5 MeV per nucleon are too low to overcome the long-range electrostatic repulsion; only above this energy the short-range nuclear forces become noticeable. Up to energies in the Fermi-energy regime, about 40 MeV per nucleon, the nuclei act rather as an entity in the reaction, because the energy of a single nucleon is small compared to the depth of the nuclear potential and because the de Broglie wavelength of a nucleon in the frame of the reaction partner is long or comparable with the size of the nucleus. By increasing the collision energy, the influence of collective phenomena decreases, and the observations better allow deducing some general properties of infinite nuclear matter. The threshold of the Delta (1232) resonance marks the gradual onset of sub-nucleonic degrees of freedom. In a projectile/target scenario, these considerations favor a beam energy of about 1000 MeV per nucleon, for investigating the properties of nuclear matter. The energy is ideal for minimizing the influence of the nuclear potential on one side and for not being affected so much by sub-nuclear degrees of freedom on the other side.

At present, the heavy-ion synchrotron SIS18 and some dedicated experimental equip-

ment establish GSI, Darmstadt, as the leading laboratory for studying heavy-ion collisions in the 1 A GeV energy regime. Energies reached at the exit of the SIS, ranging from 4,5 GeV for a proton beam up to 1 A GeV for uranium, allow to explore a rich domain of physics. In the case of heavy-ion collisions, there are very different directions in which one can pursue investigations on nuclear matter and its properties.

Collective expansion and flow measurements are the main tools to study the Equation of State of nuclear matter and in-medium effects (for a review at several energy regimes, see [RR97]). In a typical experiment (FOPI, for example), the attention is focused on central collisions to probe the hadrons under hot and dense conditions reached by the participant matter. Large-acceptance designs are essential for these studies.

On the contrary, some experiments are designed for the investigation of nuclear-matter properties thanks to the spectator matter. These experiments concentrate their selection on events of peripheral and mid-peripheral collisions. Spectator matter is not subject to compression; but it is highly excited. The first stage of the collision consists of a removal of nucleons spatially well defined but corresponding to various energy levels. This can result in the creation of holes in deep shells, that will free some energy for other degrees of freedom inside the nucleus. The excitation energy is partly consumed by the produced fragment in the early stages after the collision into expansion. Depending on the excitation energy reached by the spectator matter, this will constitute normal or diluted nuclear matter. The observables related to spectator fragments can then be used as probes on nuclear matter at low density in the case of mid-peripheral collisions.

Two different approaches for studying spectator matter have been pursued at GSI. ALADiN (A Large Acceptance Dipole magNet) and its large-acceptance detection system has access to information on the multiplicity and on the nuclear charge of fragments produced in the collision. The method is now well established, and successful experiments led to further knowledge on the phase transition of nuclear matter (similar to a liquid-gas phase transition) and on the symmetry-energy term in the EoS (see for example [TBBB$^+$07]).

The FRagment Separator (FRS) [GAB$^+$92], which is a high-resolution magnetic spectrometer, is in principle designed for secondary-beam production and delivery to further experimental areas. Recently, experiments with the FRS have proven to be suited for yielding valuable complementary information to spectator-matter studies [dSNPS06]. The benefit of using a high-resolution spectrometer for the detection of heavy residues of the projectile spectator is the full identification of the residues according to mass number A and atomic number Z, which has been achieved up to uranium [JdJC$^+$98], as well as a high-precision measurement of their kinematical properties [HGS$^+$93].

The present knowledge on the kinematical properties of fragmentation residues can be summarized as follows:

- mean values and fluctuations of the longitudinal momentum distributions of heavy residues very close to the projectile, respectively target, were compiled in 1989, and empirical parameterizations as a function of the residue mass were established [Mor89]

- a re-acceleration phenomenon was observed in mid-peripheral nucleus-nucleus collisions and related to the influence of the momentum-dependent nuclear forces [REP$^+$03, Hen05a]

- velocity distributions of lighter residues in proton-nucleus collisions with emission angles close to zero degrees with respect to the beam direction, showed complex shapes with up to three peaks [RAB$^+$06, NSB$^+$04, NSTG$^+$07], which were interpreted as signatures of different reaction mechanisms [NSB$^+$04]

In this context, we have good reasons to go on with researches that exploit the full possibilities of the FRS, taking profit from the uniquely large mass range of observed and fully identified fragments and from the very high-precision velocity information provided by the FRS, operated as a magnetic spectrometer.

The kinematical properties of spectator fragments in heavy-ion collisions constitute important observables for different fundamental aspects. In particular, some theoretical works in the frame of Boltzmann-Uehling-Uhlenbeck (BUU) calculations showed that the momentum change with the impact parameter offers a sensitivity to the in-medium nucleon-nucleon cross-section [SDL01]. To provide high-quality data on the kinematics and express them as a function of the impact parameter, to allow a comparison with theoretical models, will be one of the tasks of this thesis.

Another topic linked with the study of the kinematics of spectator matter retains our attention: the phase transition of nuclear matter. Its probable signature, the multifragmentation (or break-up) is a complex phenomenon; the kinematics of multifragmentation products is an essential observable to investigate the mechanisms of this process. It is then another aim of our work to investigate the reaction mechanisms, especially in the multifragmentation regime, with the fine informations on the kinematics provided by the FRS.

Beyond these theoretical motivations, the investigations we will conduct have some specific technical applications. Those are ADS reactor design studies (aging phenomena and radioactive inventory of the spallation source) but also secondary-beam characterization, where the fundamental principle is the fragmentation of a nucleus, and where the kinematics of the produced fragments is the main observable for the technical specifications of the device.

Therefore, we will make use of the FRS to get a global view on the phenomena which determine the kinematical properties of fragmentation residues. It is intended to provide, together with previous work, a systematic overview on the longitudinal velocities of the main remnants of the projectile spectator in heavy-ion collisions. More precisely, the main topics are:

- a study of the processes leading to the production of light residues

- a quantitative determination of the slowing down due to friction effects in peripheral nucleus-nucleus collisions as a function of the impact parameter

- a quantitative theoretical description of the width of the Gaussian component of the velocity distributions over the whole mass range

We will first give an overview of the types of reaction relevant for this study and the different features that condition the reaction mechanisms leading to fragmentation. In the second chapter, we will describe the experimental set-up used at the FRS and explain the role of each detector, in the frame of high-precision measurements, and the method to exploit these data at best. This will be the occasion to show examples of velocity spectra of the chosen experiment of interest. Experimental results come in chapter 4. They will be presented without being interpreted. The discussion is found in chapters 5, 6 and 7. We will first comment the shapes of the velocity spectra and discuss the link between observation and physical processes. The discussion about the mean velocity of the observed fragments will then be held, along with a comparison of theoretical predictions and our understanding of the data. The surprising fact that one has means to assess the centrality despite the low acceptance of the experimental set-up will be underlined. This new way of presenting the data will allow a new approach to the nucleon-nucleon cross-section, by making the comparison with theoretical models possible. Eventually, we will concentrate on the width of the velocity spectra. After going through previous models (e.g. Goldhaber [Gol74]) and predictions (Morrissey [Mor89]), we will present a new description of the reaction mechanisms and their influence on the kinematics of observed fragments, reliable for a very broad range of fragments. This model will allow us to exploit the measured velocity distributions for extracting new information on the dynamics of the break-up process leading to multifragmentation. We will profit from the unique quality of the data, which are characterized by kinematic measurements without any low-energy threshold and by full nuclide identification all over the range of produced fragments to verify the validity of substantially different model assumptions on the kinematical properties of multifragmentation products. This new description will be incorporated in a simulation code, but also, under certain approximations, reduced to an analytical formula, specifically adapted to technical applications.

Chapter 1

Reaction mechanisms

The reactions occurring in heavy-ion collisions are determined by several parameters. The beam energy is an important parameter, and different beam energies correspond to different regimes of reaction mechanisms. Very low energies are best suited to observe fusion reactions, for example on the track to discovery of superheavy elements. Fermi energies (around 40 MeV per nucleon) still allow deep-inelastic diffusions, when the reactions are mostly governed by the nuclear potential and the binding energies. Our study is based on heavy-ion collisions at beam energy well above the Fermi-energy regime.

At these relativistic energies, reaction mechanisms show a different aspect depending on the impact parameter of the collision. The degree of centrality of an event changes drastically the further evolution of the colliding system, as is schematically shown on figure 1.1.

Based on the different time scales of the reaction mechanisms observed in a relativistic heavy-ion collision, it is usually treated as a two-step process. The first step that is called fragmentation consists of collisions of individual nucleons. The de-excitation phase, where nuclear potential and binding energies are again important, forms the second step of the reaction.

We will employ the terms "projectile" and "target", as they were used in the GSI set-up. We will concentrate on the projectile, since the fragments observed through our main experimental tool, the FRS, are the so-called projectile-like fragments. This definition holds in the sense that given their relatively high longitudinal velocity, they are most probably remnants from the nuclei of the beam. The typical configuration of collision consists of a projectile hitting a target, with an impact parameter in principle different from zero, so that a piece of incoming nuclear matter continues its way, while the rest of the nucleons interact strongly with the nucleons of the target.

Depending on the initial conditions, nuclear reactions can show very different aspects. The problem is that we do not always have control on these initial conditions. Of course, the energy of the collision is defined by the user. But the energy of the collision is not the only parameter that will determine the future of the colliding systems. Most importantly, the impact parameter of the reaction, which defines the violence of the collision, is not an adjustable parameter. It means that observations will *a priori* reflect a mixture of different

mechanisms corresponding to different regimes of the nuclear reactions, accordingly to their centrality. Meanwhile, full-acceptance experiments have at their disposal some tools to estimate the centrality of a collision. Indeed, the main signature of this parameter is the multiplicity of fragments produced in the event.
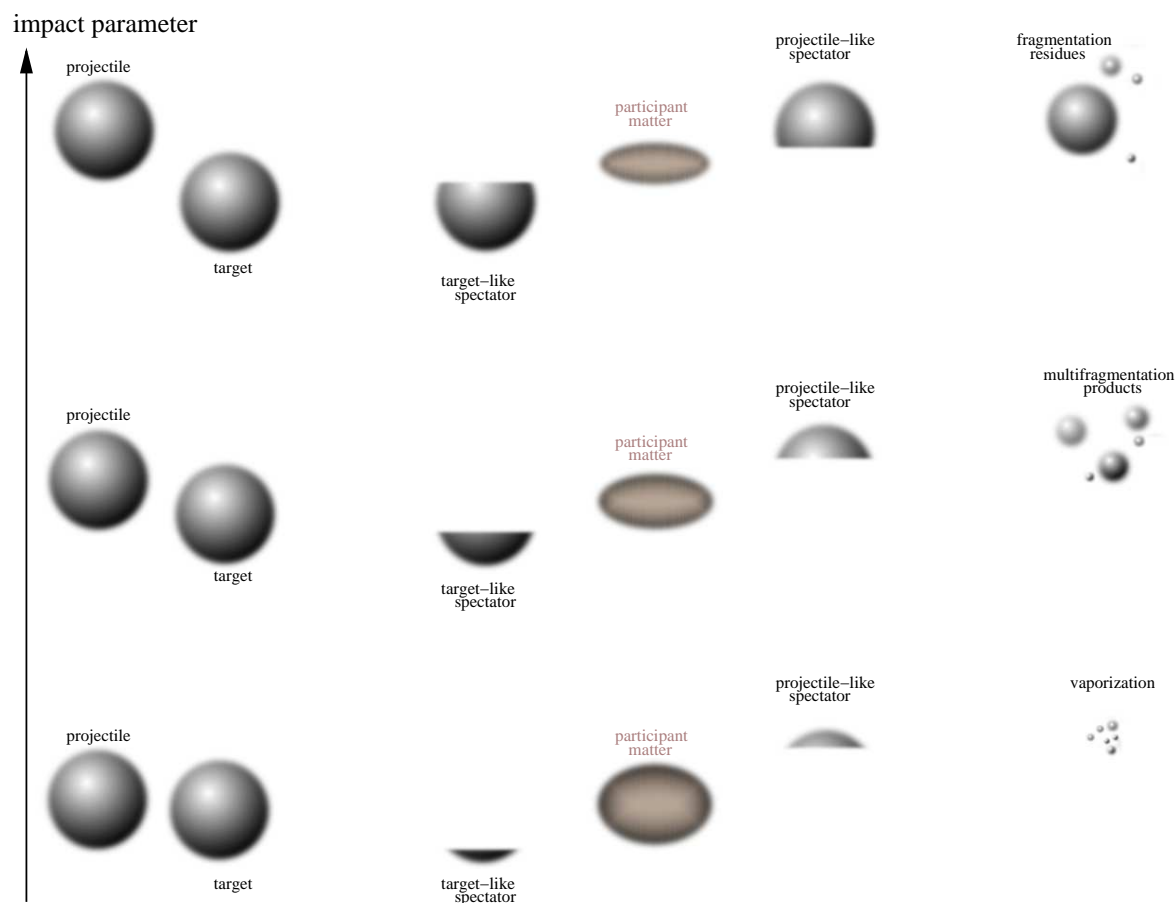
Figure 1.1: Scheme of different scenarii depending on the impact parameter, from a very peripheral collision producing a large spectator fragment and few nucleons, to a mid-peripheral collision where the spectator is multifragmented, down to a central collision where the small spectator matter is vaporized in single nucleons (only fragments with velocity close to the projectile are drawn in the last time sequence).

Let us now define and give already some hints about our comprehension of the different processes that are at play in our reactions of interest, with relativistic beam energy and peripheral collisions (no vaporization).

1.1 Abrasion

Abrasion is the first step in the nuclear reaction, in the sense that it is the first process resulting in removal of nuclear matter from the colliding nuclei, projectile and

target (see [Ser47]). The abrasion is the result of individual collisions between nucleons of the projectile and nucleons of the target nucleus. The spectator fragment surviving the fragmentation step is characterized by its mass, charge, excitation energy, angular momentum and velocity. The correlation between the parameters of the collision (incident energy, impact parameter...) and the features of the produced spectator fragment can be discussed through different descriptions of the reaction mechanisms.

There are several ways to model the fragmentation process: intranuclear cascade, BUU, Quantum Molecular Dynamics (QMD), geometrical abrasion model... In the abrasion model, it is seen as a geometrical cut, between spectator and participant matter, corresponding to the zone where nuclear trajectories overlap. This could act as a blade, shearing off some nucleons from the fragment without further interaction.
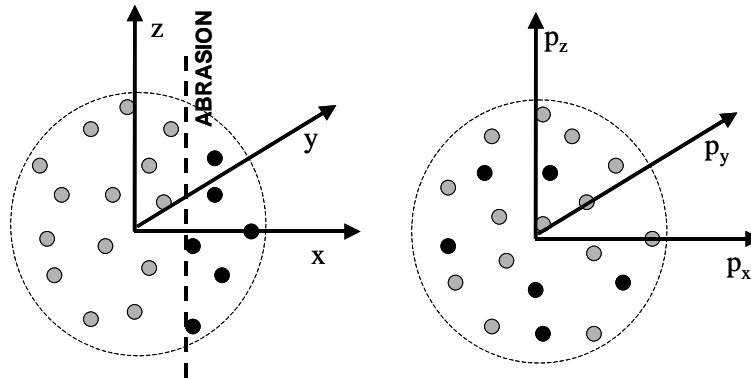
Figure 1.2: Nucleon removal during the abrasion stage. On the left, in position-space, the abraded nucleons (in black) correspond to a well-defined zone. The right picture shows that in momentum-space, they are randomly distributed within the frame of the Fermi-gas model.

The geometrical zone of overlap of nucleons from the projectile and the target is well defined. The abraded nucleons belong to that region, but -as is seen in figure 1.2- in phase-space, this nucleon removal is creating some holes, randomly distributed in the frame of the Fermi-gas model, where there is no correlation between the local position and the momentum of a nucleon. Some deeply bound nucleons can be removed, inducing some high excitation energy inside the spectator fragment.

We will see that this would be already sufficient to explain most of the features of the momentum distributions of the observed fragments, given the Fermi motion of the nucleons inside the colliding nuclei.

Yet, such a reaction leads forcefully to a rise in excitation energy in the bound nucleonic matter. Spectator fragments are not anymore just "spectators", but leave this reaction stage heated up, as in a friction phenomenon. The spectator matter is then excited and undergoes further evolution (mass loss) before being detected.

1.2   Evaporation

The single-particle degrees of freedom of the spectator residues are quickly thermalized (within a few 10^{-23}s), and in the next step, they may loose mass via different binary decay channels like particle evaporation and fission. The probabilities for the evaporation of different particles are described by different models. One can quote for example the models of Weisskopf-Ewing [WE40], or of Hauser-Feshbach [HF52].

Nucleon removal by abrasion is a step that does not leave the nucleus cold. It can be seen as a friction process, removing nucleons from the projectile, but also inducing high excitation energy in the remaining fragment.

This excitation energy extends to very high values. There the level densities that determine the probabilities of the different decay channels become comparable, and hence, these decay channels become available. The level density ρ of a given emission channel is related to the available energy (linked with the temperature of the prefragment) by the following, omitting pre-exponential factors and neglecting tunneling for this illustration:

$$\rho \propto e^{2\sqrt{a(E-B)}} \tag{1.1}$$

where a is known as the level-density parameter (approximately $A/11$, with A the mass of the daughter nucleus when excitations of the emitted fragment are neglected), and B is the barrier for a specific decay channel. The representation of $\ln \rho$ as a function of E helps understanding the evolution with high energies.

In the upper panel in figure 1.3, the two curves, corresponding to two different decay channels, become closer with the increase of excitation energy. The panel underneath shows that the ratio between the corresponding level-densities decreases very rapidly with the energy rise. At high energies, the ratio between level densities for different decay channels is approaching 1. This means that at high excitation energies, many binary decay modes tend to be equally probable.

This statement is comforted by the observation that in our experiment, the mass range from the lightest identified elements up to the projectile is continuously populated by reaction products.

If the prefragment produced by abrasion is fissile, fission constitutes a probable evolution of the system of nucleons. A further mass loss is induced by evaporation, which competes with fission. It consists of a sequential emission of nucleons and light nuclei.

In principle, the evaporation process explains mostly the production of light fragments (and their heavy partner, near the mass of the projectile). Symmetric fission allows for binary decay products with masses near half the mass of the projectile. Again, the observation of a continuous distribution of fragments along the mass range is an indication for a transition or continuity between the two processes.

Attempts have been made in the past to conciliate evaporation and fission models into a general description of the binary decays, but that theory is not yet fully developed (see for example the models of Moretto [Mor75], Swiatecki [Swi83] and the discussions of Richert and Wagner [RW92], Stokstad [Sto]).
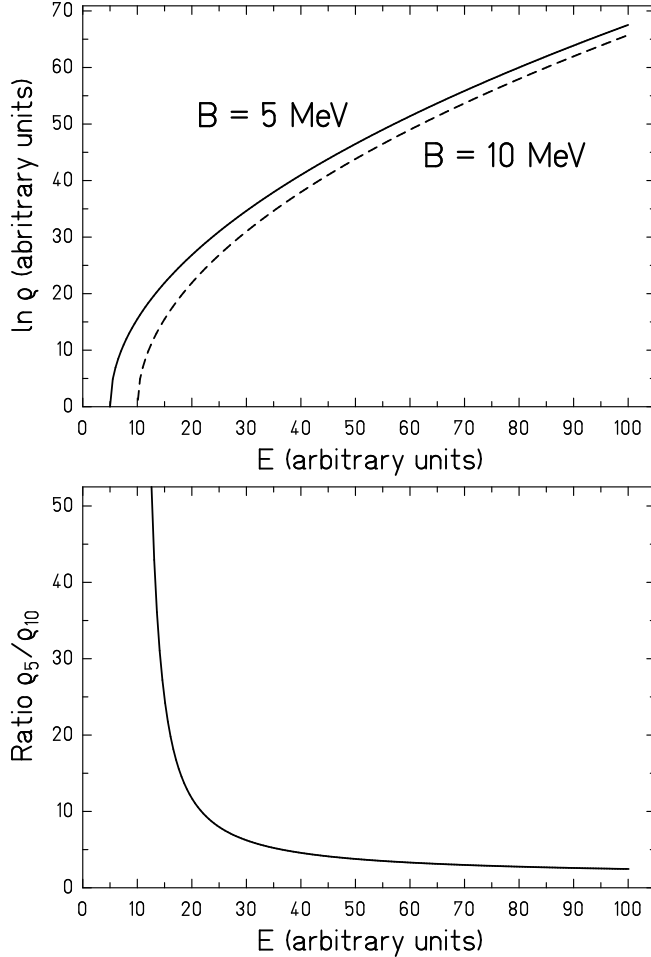
Figure 1.3: Up: calculated logarithm of level-densities for a mother nucleus $A = 132$ as a function of excitation energy; two different barriers were assumed: 5 MeV (plain line) and 10 MeV (dashed line). Down: ratio of the two level-densities as a function of excitation energy.

The treatment of the evaporation in a model supposes an ability to calculate decay probabilities for different channels, starting from an excited prefragment. Induced recoil and energy loss by evaporation depend strongly on the decay channel followed. This is why it is very important in the context of the present work to model it correctly.

The projectile-like spectator fragment acquires an angular momentum, partly due to the missing angular momentum of abraded nucleons [dJIS97], partly due to the friction force. While the first contribution is isotropic in space, the axis of the second contribution always lies in a plane perpendicular to the beam direction. The barrier of the decaying system is lowest when the fragments are emitted in a plane perpendicular to the angular-momentum axis, since the momentum of inertia is largest in this configuration. Therefore, there is an enhanced emission in forward and backward directions. However, this enhancement diminishes if the nuclear temperature becomes comparable with the

variation of the barrier as a function of orientation [KHSA07, VH93]. Since the angular momentum induced in the fragmentation process is rather low [dJIS97], and the excitation energy is rather high, the angular distribution of most binary-decay products is very close to be isotropic.

The model of Hauser and Feshbach [HF52] is taking angular momentum into account. Using the principle of the detailed balance, one can calculate the probability of absorption of one nucleon or fragment for different geometries of collision, characterized by impact parameter or corresponding angular momentum. This is representative for the probability of emission of the particle from a mother nucleus having this same angular momentum. An integration over all possible configurations or a Monte-Carlo simulation can be used to predict the emission probabilities, depending on the needs.

Weisskopf and Ewing did not explicitly consider the angular momentum in their model. The emission probability is also calculated by the inverse process of particle capture. Refinements in addition to pure geometrical cross-section are included, such as quantum-mechanical effects, but the impact parameter of the collision does not enter explicitly the description of the capture cross-section. This model can be used in our context since we have indications that angular momenta reached in our reactions are not very high (not exceeding 20 $\hbar$) ; see [dJIS97].

Particle emission can be seen in a general sense as a binary split. Two ways of describing this binary split can be used. The evaporation is usually modeled as the inverse process of fusion. It supposes that the evaporated fragment (or nucleon), formed inside the mother nucleus has a sufficiently high momentum to overcome the evaporation barrier. The evaporated fragment is thus emitted in the shape of its ground state, which is rather close to sphericity. It is used for the emission of protons, neutrons, alpha particles and other light nuclei.

The other picture is based on the formation of complex shapes of the compound (or here "mother") nucleus itself. This may lead to fission. For heavy nuclei, this process is favored in symmetric splits. In this case, the fission barrier is lower than the evaporation barrier. The shapes experienced in fission resemble more the shapes which appear when a honey drop falls from a spoon. A more or less long neck develops between the two fragments which are forming, until the rupture occurs. This process is fundamentally different from the evaporation described above.

Evaporation and fission barriers have been calculated for three different systems: ^{86}Kr, ^{136}Xe and ^{208}Pb. The results of these estimations are plotted in figure 1.4. Since we reach high excitation energies, we neglect shell effects and consider the nuclei on a macroscopic basis, using the liquid-drop model [MS67] to calculate Q-values of the decaying channels. To estimate the evaporation barrier, we consider the evaporation as the inverse of the fusion process. We use the nuclear potential which is described by Bass [Bas]. Additional contributions to the total potential are Coulomb forces (taken between point-like charges) and centrifugal forces.

Realistic calculations of the fission barrier are rather complex, and beyond the scope of this discussion, which is meant as a simple comparison between descriptions of binary decays. Using a few assumptions, one can realize a fair estimation of the fission barrier.

Wilkins et al. [WSC76] provide a formula for the potential energy of the system at the scission point. It is treated in this paper as the sum of the liquid-drop, the shell- and pairing-corrections for each fragment (spheroid), with Coulomb and nuclear potential terms describing the interaction between the two coaxial spheroids, whose tips are separated by a distance d:

$$
\begin{aligned}
V(N_1, Z_1, \beta_1, N_2, Z_2, \beta_2, \tau, d) = & \sum_{i=1,2} V_{LD_i}(N_i, Z_i, \beta_i) \\
& + \sum_{i=1,2} \left(S_i(N_i, \beta_i, \tau) + S_i(Z_i, \beta_i, \tau) \right) \\
& + \sum_{i=1,2} \left(P_i(N_i, \beta_i, \tau) + P_i(Z_i, \beta_i, \tau) \right) \\
& + V_C(N_1, Z_1, \beta_1, N_2, Z_2, \beta_2, d) \\
& + V_n(N_1, Z_1, \beta_1, N_2, Z_2, \beta_2, d)
\end{aligned}
\tag{1.2}
$$

According to Wilkins et al., the total kinetic energy of the two deformed products is given approximately by the Coulomb potential V_C. Omitting the form factor to account for the difference in Coulomb interaction between point-like charges and deformed spheroids, it can be written:

$$
V_C \approx \frac{Z_1 Z_2 e^2}{D}
\tag{1.3}
$$

where D is a function of the deformation of each product β_i and the distance d between them at scission:

$$
D \approx d + \sum_{i=1,2} r_0 A_i^{1/3} \left(1 + \frac{2\beta_i}{3} \right)
\tag{1.4}
$$

Under these conditions, i.e. the form factor and the volume conservation under the deformation not being explicitly written in the formula, the parameters of the Wilkins model (without shell- nor pairing-corrections) were adjusted by Böckstiegel et al. [BSB+97] to fit experimental data on the total kinetic energy of the fission fragments. The deformation factors of the two fission fragments were both set to $\beta_{1,2} = 0.625$; the tip distance d at scission of the two spheroids, used to simulate a neck, was assumed to be 2 fm.

The total kinetic energy of the two fission products is calculated with these values through the equation 1.3. It represents the kinetic energy of two deformed nuclei, due to Coulomb forces with an initial distance d. This initial situation is not exactly at the scission point because there is an additional pre-scission kinetic energy contributing to the kinetics of the products. A pre-scission kinetic energy T_{init} of about 13 MeV is subtracted to the value from equation 1.3 to obtain the energy difference between the deformed fission products and the system at scission.

From theoretical works by Asghar and Hasse [AH84], the potential difference ΔV between the saddle and the scission point can be determined.

The sum of ΔV and the corrected kinetic energy of the fission products corresponds to the height of the barrier, counted from the masses of the separated cold deformed

products with $\beta = 0.625$. The fission barrier relative to the ground state of the mother nucleus is obtained with the deduction of the Q-value of the reaction and the energy E_{def} that enters the deformation of the products.

Altogether, the fission barrier is expressed by:

$$B_{fiss} = V_C - T_{init} + \Delta V - |Q| + E_{def} \qquad (1.5)$$

In case of krypton, the evaporation and the fission barrier are almost the same along the whole mass range. They both reach a maximum at mid-range ; it means that the symmetric binary split is very unlikely, independently from the process.

With xenon as a mother nucleus, the fission barrier does not show anymore a clear maximum at middle mass-range. The curve is almost flat for most of the range. Nevertheless, very unlikely symmetric splits are described more realistically by the fission picture than by evaporation. Both evaporation and fission barriers decrease for asymmetric decays. There, even if evaporation is slightly favored, we can conclude that the way the binary split is described does not play a major role: both processes are comparably likely.

Finally, a heavy mother nucleus like lead has a fission barrier much below the evaporation barrier for almost any channel of binary decay. The fission barrier has a clear minimum for symmetric splits, which are then favored in this description of the binary decay.

The conclusion from this discussion about the ways to describe binary decays is the following. To be able to reproduce the data with a simulation code, both fission and evaporation processes must be included. Since no unified theory is available at present time, the choice is often made to treat the "wings" of the mass distribution with an evaporation code; beyond a certain threshold in emitted mass, fission description is preferred. This artificial transition occurs in the (small) mass range where the two models are in agreement. Such a combination is made for example in GEMINI or in ABRABLA [GS91] codes.

The magnitude of the evaporation is, as already underlined, directly correlated to the excitation energy available after the abrasion step and possible fission process. For non-fissile systems, it is reasonable to link the extent of the mass loss by evaporation to the energy rise due to abrasion, depending itself on the impact parameter of the collision.

1.3   Multifragmentation

We already mentioned abrasion, pure geometrical cut of the projectile and leading to a prefragment. This latter has then acquired some excitation energy directly linked to the "violence" of the abrasion (amount of nucleons abraded). Apart from possible fission, the basic process of de-excitation is a series of (small) mass losses by evaporation; the system emits nucleons or very light nuclei.

For smaller impact parameters, i.e. more central collisions, it has been shown that the excitation energy reached after the abrasion step is high enough so that the system is unstable and breaks into several pieces, possibly emitting some light nuclei (in addition
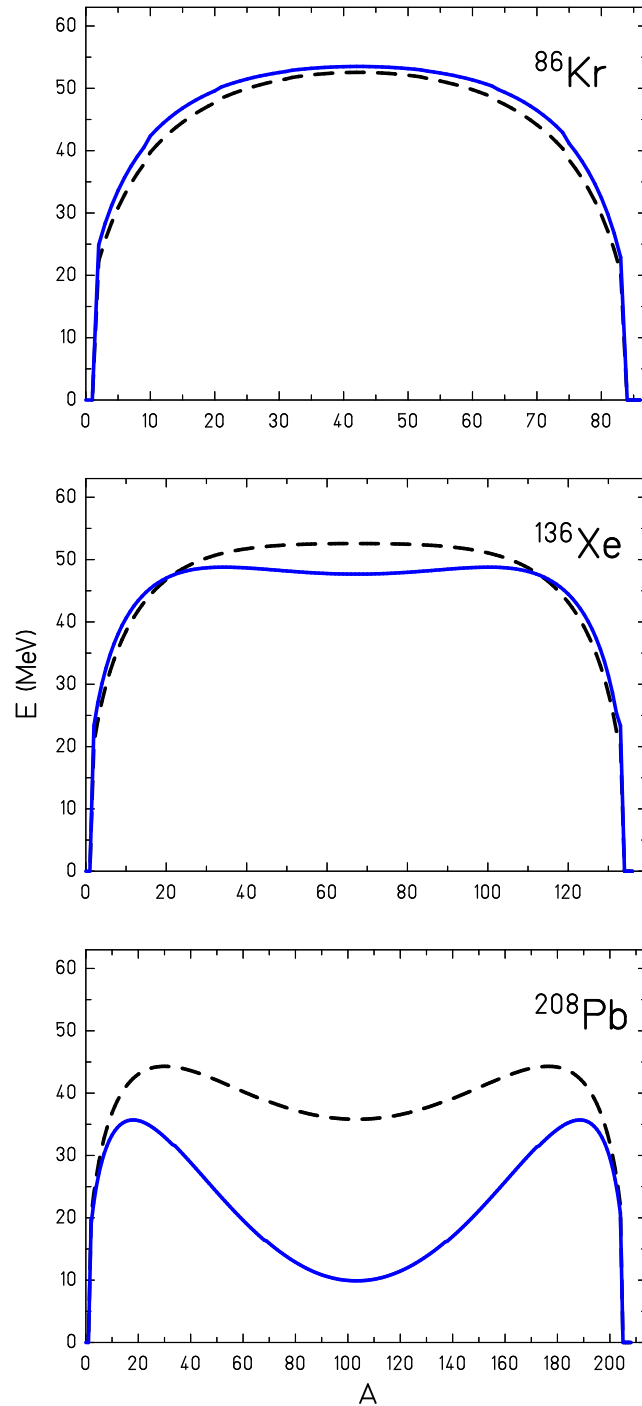
Figure 1.4: Calculated barriers for evaporation (black dashed line) and fission (blue line), for three different compound nuclei. A is the mass of the emitted fragment.

to the main fragments). The energy rise due to the abrasion allows the volume of the fragment to increase, weakening the binding energy of parts of the nucleus (see for example [OBBB+00]).

A large-acceptance set-up allows to study this break-up on the basis of information on the multiplicity of the event. The ALADiN collaboration mostly exploits this information to study phase-transition effects in nuclear matter.
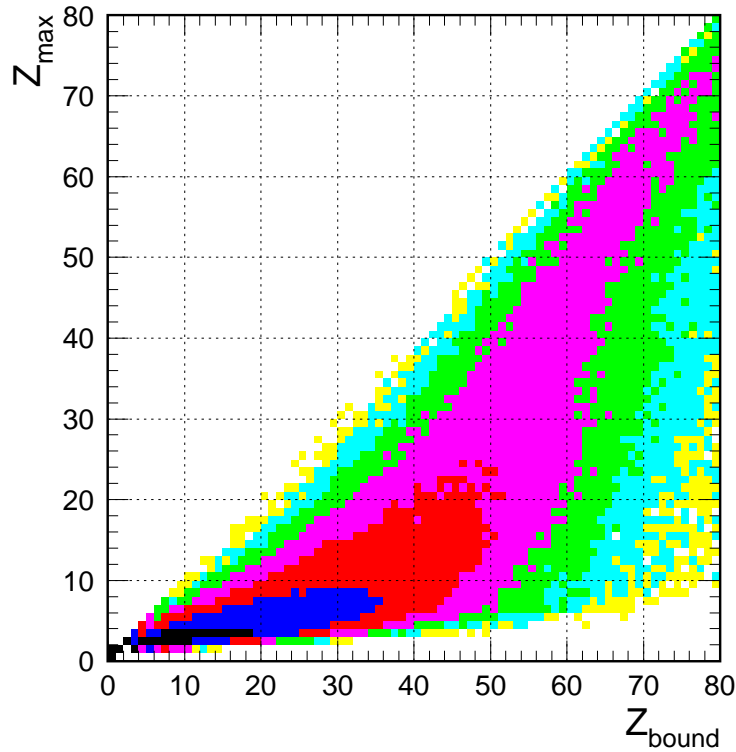
Figure 1.5: Zbound as a function of Zmax observed in Au+Au collisions with ALADiN.

Figure 1.5, obtained by the ALADiN collaboration and discussed for example in [TBBB+07], represents Z_{bound}, the sum of charges of observed fragments with an atomic number larger than 2, as a function of Z_{max}, the largest atomic number observed. Large Z_{bound} values correspond to peripheral collisions and low excitation energy. Most of the charge is contained in one large fragment. A drop occurs around $Z_{bound} = 50$, and under this charge, Z_{max} is much lower. This is an indication for a transition towards a regime where collisions induce more excitation energy, and the formation of several clusters of comparable size becomes dominant.

The modeling of the multifragmentation has been developed in several ways, statistical (SMM [BBI+95]) and dynamical (see for example Nörenberg et al. [NPR00]).

Independently from the type of model (statistical or dynamical), one can make different assumptions on the way the multifragmentation proceeds, and on the role of this process in the kinematics of the produced fragments. The time-scale of the break-up process is

decisive: if the fragments are formed and separated in a very short time, no equilibrium is reached by the system.

In the dedicated statistical model SMM, the prefragment is supposed to reach thermal equilibrium. It is then treated as a thermodynamical system, and a temperature can be defined. Each product of multifragmentation carries information on the temperature of the mother nucleus. In this picture, the kinematical properties of the produced fragments are governed by the thermal motion inside the breaking-system and the Coulomb repulsion at play between pieces. The kinematics of the fragments at freeze-out is assumed to be governed by Boltzmann statistics with a temperature parameter given by the freeze-out temperature. Any influence of the Fermi motion of the nucleons in the cracking system is not considered in SMM.

On the contrary, the break-up can be treated as a "spontaneous" or quick process, leaving no time for any equilibration of the prefragment. Then in principle, the kinematics of the pieces formed through this break-up is mostly determined by the Fermi motion in the mother nucleus. This picture is supported by the studies pursued by Odeh et al. [OBBB+00] and previously by [HBF+84].

However, the energy rise inside the prefragment due to abrasion has more complex consequences. In the Fermi gas model for an ensemble of nucleons of mass m, the level density can be expressed by:

$$\rho = V\sqrt{E} \cdot \frac{4\pi\sqrt{2m^3}}{h^3} \qquad (1.6)$$

The most probable configuration of the system of nucleons is given by the maximum of the entropy, proportional to the logarithm of the level density ρ. It can be calculated as a function of the excitation energy and the volume (in units of the normal volume); a graphic representation of this dependence is drawn in figure 1.6.
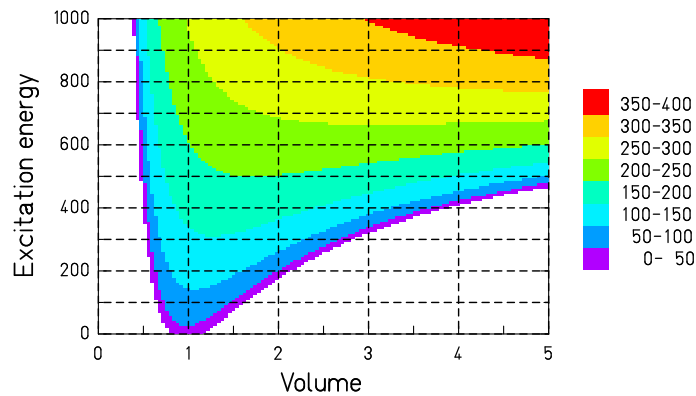
Figure 1.6: Schematic diagram of the evolution of the entropy of the system of nucleons as a function of the volume expansion.

The maximization of the entropy at a given excitation energy implies that the volume of the system increases with excitation energy. The prefragment produced by the abrasion

phase is highly excited; we can expect that this results in a volume expansion. The system of nucleons entering the multifragmentation phase is in this sense a dilute system. The expansion with excitation energy has been explored for example in [DSVC06].

If the volume increases, it means that the nucleonic matter expands, so that the pieces formed have a radial velocity outgoing the center of mass of the system. This contribution is probably small. Furthermore, since the Fermi motion is conditioned by the density of particles in the system, the dilution of the nucleons through the volumic expansion of the prefragment could play an important role in the description of the process.

Finally, the formed pieces at break-up are charged and Coulomb interactions contribute to the kinematics of the fragments. Although this interaction is known and easily theoretically described, its concrete implementation in a simulation code or in an analytical model needs assumptions. We will discuss that matter more extensively in the last chapter.

Chapter 2

Experiment

In this chapter, we will describe the facilities used at GSI (near Darmstadt, Germany) for our experiment. The experimental set-up will be presented, with a stress on the crucial detectors giving informations on the velocities of the fragments.

2.1 The accelerator facility

Let us explain step by step how the beam is delivered to the experimental area, at the fragment separator.

2.1.1 GSI

The global layout of the GSI laboratory is displayed in figure 2.1. The linear accelerator UNILAC, the synchrotron SIS and the storage ring ESR have been labeled, in addition to the fragments separator FRS, whose section is highlighted.

2.1.2 UNILAC

The linear accelerator UNILAC (see figure 2.2) is used as an injector for the synchrotron but also provides the low-energy experimental areas with a beam. Depending on the ion source, a section of preacceleration is used, before stripping the ions. The total length of the UNILAC is around 100 metres. The ion-source used was the PIG (Penning-Ionization-Gauge). After the preacceleration by the HSI (RFQ+IH1+IH2), the beam goes through a gas stripper. The Alvarez section accelerates then the beam from 1.4 A MeV to a standard value of about 11 A MeV for injection into the synchrotron SIS; at this point, the energy spread of the beam is within the requirement of $\pm 0.2\%$.

2.1.3 SIS18

The SIS18 is a heavy-ion synchrotron (*SchwerIonenSynchrotron* in German) of maximum bending power around 18 Tm. The characteristics of its accelerating devices and
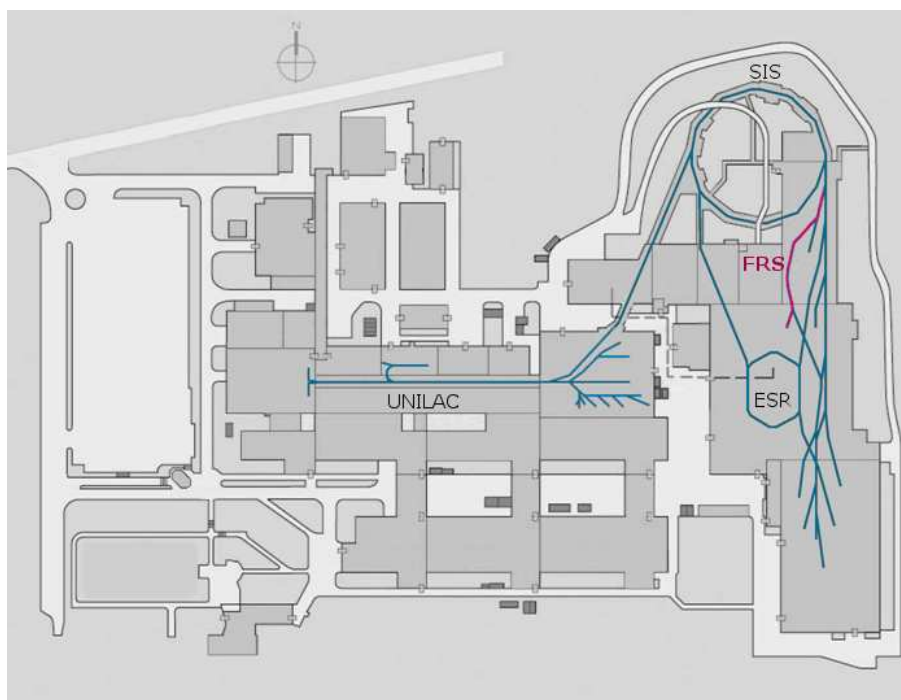
Figure 2.1: Layout of the GSI main facilities.
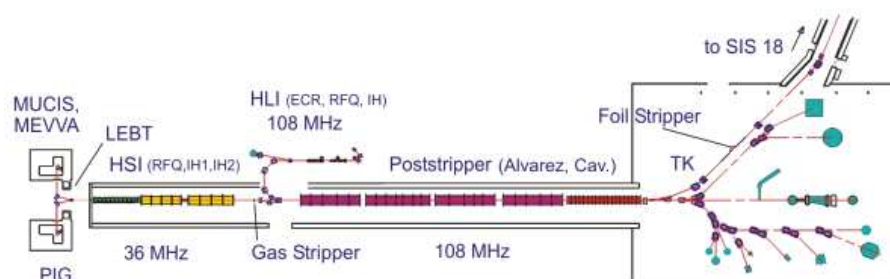
Figure 2.2: The linear accelerator UNILAC.

numerous magnets (dipoles, quadrupoles and sextupoles) are listed within figure 2.3. Even after extraction, the momentum spread of the delivered beam is rather small. The spatial spread (beam profile) at the entrance of the spectrometer is displayed in figure 2.4. It shows a small spread in x and y directions (in the order of 5 mm).

2.2   High resolution set-up: the FRS

The FRagment Separator (FRS) is a high-resolution magnetic spectrometer with an angular acceptance of about 15 mrad and a momentum acceptance around 3% ; it is
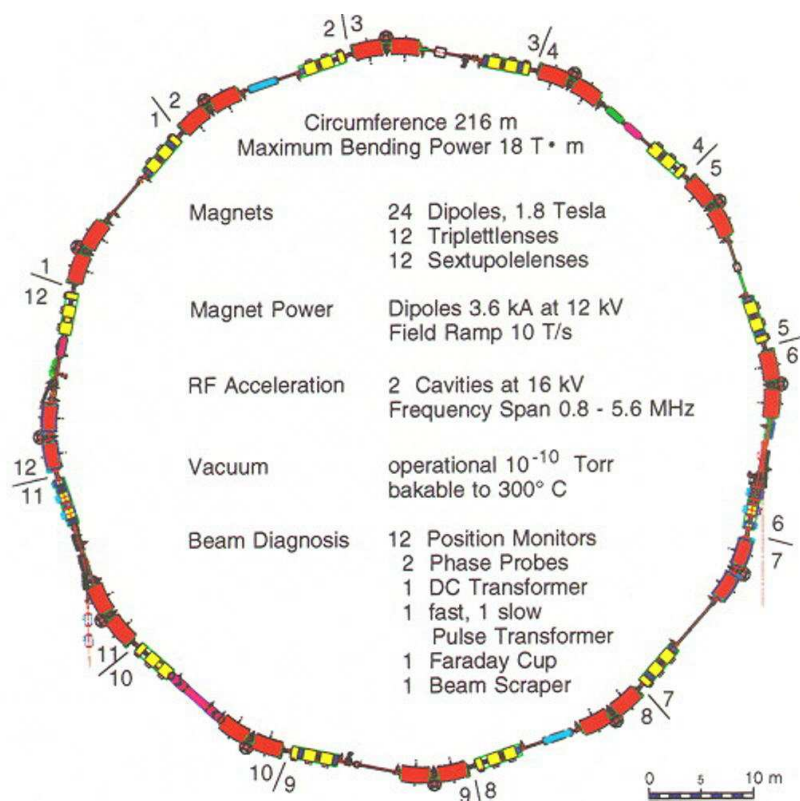
Figure 2.3: Specifications and layout of the SIS18.
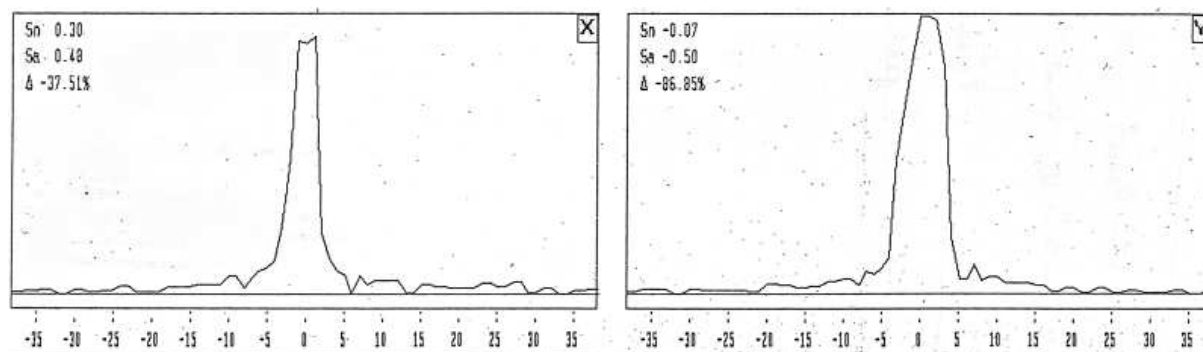
Figure 2.4: Scan from the log book of the experiment, showing the beam profile in x and y directions as seen in the current grid before the target. The unit is the millimeter.

represented in figure 2.5. The CHARMS group [1] makes it its specialty to exploit the resolution of the FRS at its best for fission and fragmentation production, as well as studies of reaction-mechanisms.

Full identification of the produced nuclides in the reaction should be achieved to reconstruct isotopic distributions and cross-sections. Furthermore, it should offer the

---

[1]http://www-w2k.gsi.de/charms/

possibility to measure the longitudinal velocity of transmitted fragments with a very high accuracy, taking advantage of the length of the spectrometer ($\sim 74m$), even though we use only half of it for time-of-flight measurements.

The price to pay for high precision is the lack of information on multiplicity and, *a priori*, on the impact parameter of each event. One also needs to make assumptions on the influence of the limited acceptance, and assumptions on the production mechanisms to link the observed data to real physics. They will indeed modify the shapes of the distributions.
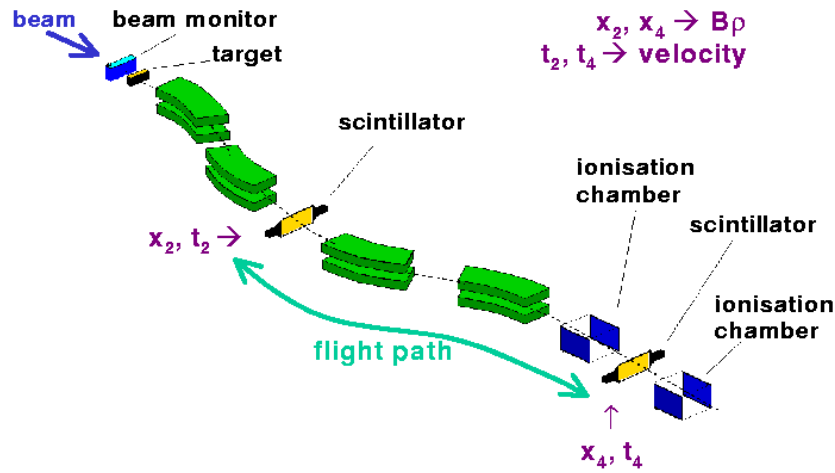
Figure 2.5: FRS schematic set-up.

The fragments produced by collision with the target continue their way along the beam axis and go through the FRS if they were emitted within its acceptance. Nuclei travel through dipole magnets who deflect them as a function of their momentum-over-charge ratio. Along their path, they traverse a series of detectors of different properties that shall be described in the following paragraphs.

2.2.1   Magnets

As already mentioned, the momentum acceptance of the FRS is very limited. A given combination of fields in the four dipoles calculated from ion-optics models corresponds to fragments in a certain range of magnetic rigidity that can travel through the whole spectrometer. Since the magnetic rigidity of a given fragment is linked with its velocity, it means that a setting of magnetic fields in the dipoles lets only a slice of the velocity distribution reach our detection systems at the exit of the FRS. The combination of successive magnetic settings (preferentially overlapping) will allow a complete reconstruction of the transmitted velocity spectra of the fragments.

The two halves of the magnetic spectrometer act as two different selections in the nuclear chart. As is schematically drawn in figure 2.6, the first half of the FRS up to

the dispersive image plane lets go through the fragments inside a conic selection of the nuclear chart. An energy degrader can be placed at the intermediate image plane, where the ions loose part of their energy according to their atomic charge. The energy loss in the intermediate degrader and the selection in the magnets of the second half of the FRS, between the intermediate image plane and the exit, couples with the first selection to keep only fragments in a given nuclear-charge range.
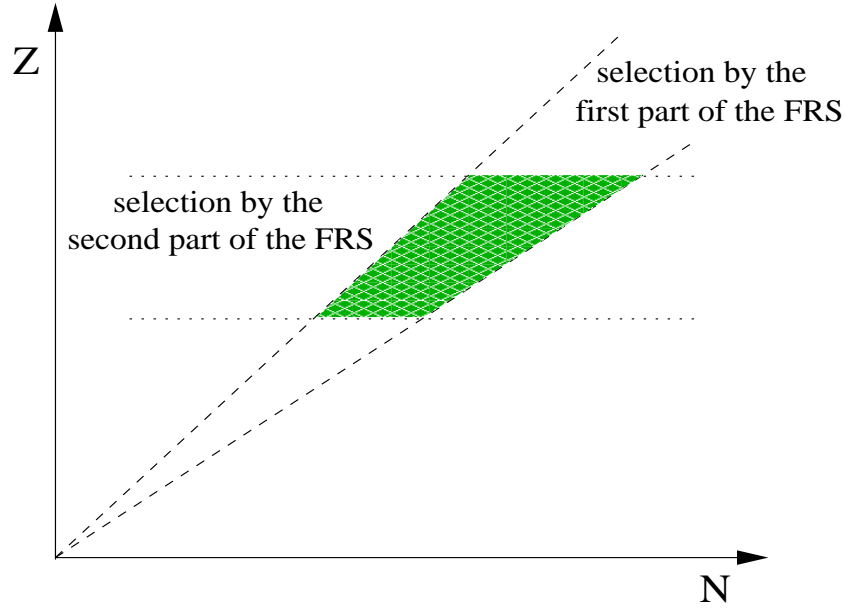
Figure 2.6: Principles of the selection of fragments in two steps by the magnetic settings of the first and second half of FRS. The region of the chart finally accepted is highlighted in green.

Nominal values of the magnetic fields are set by the FRS user; the effective values in the dipoles are measured by Hall probes and checked several times during the experiment by centering of the primary beam (of known rigidity).

Dispersion in each part $i = 2, 4$ of the FRS:

$$D_i = \frac{dx_i}{d(B\rho_i)/(B\rho_{icenter})} \quad (2.1)$$

Dispersions are expressed in cm/%; they represent, at S2 or at S4, the position shift on the horizontal axis if the magnetic rigidity of the considered fragment in the section is 1% higher or lower than the magnetic rigidity of the centered ion. Dispersion values are measured experimentally, typically using the beam as reference and varying the magnetic fields in the first or the second half of the FRS. Table 2.1 gives the values obtained for each section.

At the dispersive image plane S2, the horizontal position x_2 in the scintillator gives the magnetic rigidity of the fragment for a given setting in magnetic field B_{12}:

$$B_{12}\rho_{12} = B_{12}\rho_{12}(central) \cdot \left(1 + \frac{x_2}{D_2}\right) \quad (2.2)$$

D2(cm/%)	D4(cm/%)
6.72$\pm$ 0.03	8.79$\pm$ 0.06

Table 2.1: Dispersion measured from the position in the target area and at the intermediate image plane for D_2, and between intermediate and final image plane for D_4.

The expression of the magnetic rigidity in the second part of the FRS is slightly more complex because the ion can originate from a broad distribution in x_2. Since the full spectrometer is achromatic, the magnification between S2 and the final focal plane S4 is given by $M = D_4/D_2$:

$$B_{34}\rho_{34} = B_{34}\rho_{34}(central) \cdot \left(1 + \frac{x_4 - Mx_2}{D_4}\right) \tag{2.3}$$

The focalization and defocalization of the beam is achieved by quadrupole triplets. Each quadrupole is focalizing the beam in one plane. The combination of x-focusing, y-focusing and again x-focusing magnets achieves the focalization in space.

In addition, each dipole is immediately preceded and succeeded by a sextupole magnet to correct second-order ion-optical aberrations.

2.2.2 Scintillators

The measurement of the velocity of the nuclei flying through the FRS is deduced from the time of flight. The times at which fragments are passing by S2 and S4 are exploited as start and stop. We use scintillators that feature a good time response and allow position detection in the x direction (perpendicular to the beam). The scintillators used are made of plastic BC420, and they provide signals with a rise-time of around 1.5 ns.

Their thicknesses are chosen according to foreseen energy loss, straggling and secondary-reaction. The thinner would be the better (it would reduce the amount of secondary-reactions), if it did not lower the light signal at the same time, hence decreasing the signal-to-noise ratio. The thicker the scintillator, the greater height of the signal but also the more effect on the spectra. One has to find a compromise between these two.

Let us comment figure 2.7. Some fragments may reach the scintillator at S2 (SCI2) but then, due to the selection in magnetic rigidity, be lost on their way through the second section of the spectrometer. On the contrary, a fragment detected by the scintillator at S4 (SCI4) has forcefully hit SCI2. The triggering of the data acquisition will be based on the SCI4 signal for a start, the SCI2 signal being delayed and used as a stop time.

The signal itself is preprocessed. The scintillation light due to a traversing fragment is collected by photomultipliers placed at each edge of the slat. The amplified output of the PM enters a Constant Fraction Discriminator (CFD) which produces a digital signal when 10% of the amplitude of the analog input is reached. This time marker is provided for SCI2 and SCI4 from left- and right-hand sides.

For each scintillator, the time information from one side is delayed (on the scheme, the right side). The interval between sides is converted by a Time to Amplitude Converter
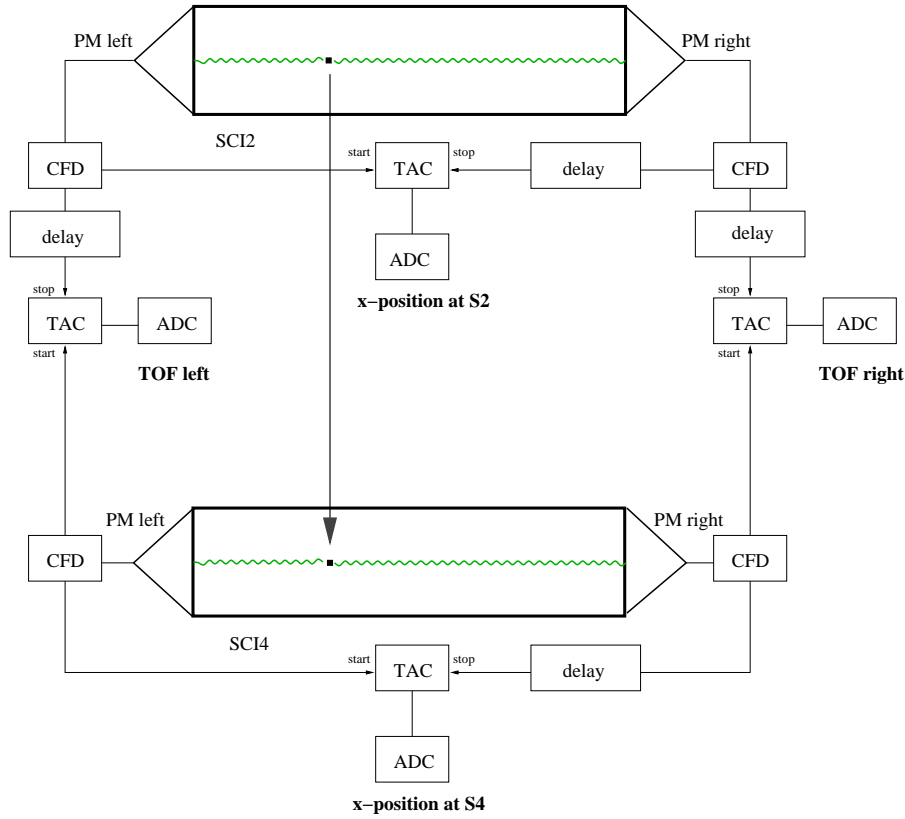
Figure 2.7: Scheme of the TOF signal treatment.

(TAC) and an Analog to Digital Converter (ADC) into a signal directly measuring the position of the hit on the x-axis (main axis of the slat, perpendicular to the beam axis). By a similar process, the left times -or right times- from SCI2 (delayed) and SCI4 are providing a time interval that gives the Time of Flight for each side (TOF left and right).

The main source of uncertainty on the time of flight is the fluctuation of the time signal from the CFDs. And the jitter on this time comes from the fluctuations during the rise of the analog signal coming from the scintillator. One improvement is obtained by increasing the amplitude of the signal by the use of a thicker scintillator; but we have seen that it induces more secondary-reactions. Another solution is to increase the stiffness of the slope of the signal and shorten the rise-time of the analog signal. This is concretely achieved by the application of a larger voltage on the photomultipliers. The amplification is effective on the signal and the noise, but the signal pulse becomes shorter as well, and the rise-time is shorter.

The PMs used in CHARMS experiments at the dispersive image plane S2 are specifically designed to sustain a high-current regime. Large current variations are induced by large rates of ions passing by. To face these intensity variations, specifically low resistors are mounted in between dynodes, so that current variations do not translate into large voltage variations; the PMs gain in stability.

2.2.3   Ionization chambers

The active volume of the two ionization chambers placed at S4 is of around 40x27x15 cm^3. It is filled with P10 gas (90% argon, 10% methane) and kept under normal conditions. Their designation is MUSICs, which stands for MUlti-Sampling Ionization Chambers, referring to the four independent anodes used to measure energy losses and drift-times along the trajectory of incoming charged particles.
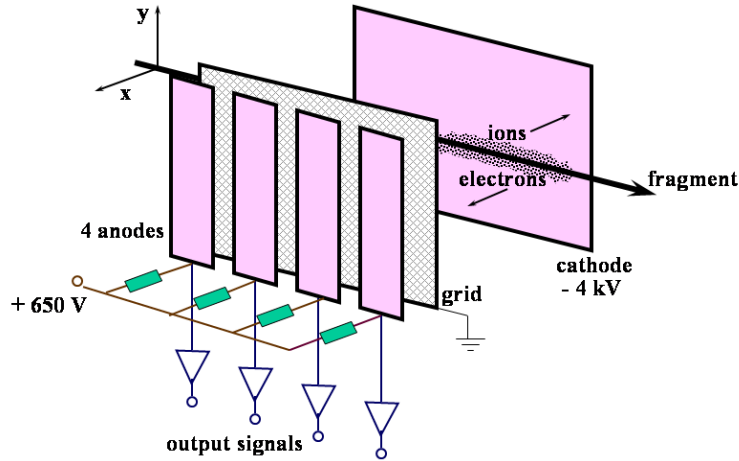
Figure 2.8: Active volume of a MUSIC.

Signals coming from the preamplifiers are sent to two different channels, to treat specifically the information to extract energy-loss and drift-time.

Energy channel

One signal is passing by the main amplifier. Bipolar signals have proven to be more handy than unipolar signals for further treatment, therefore our main amplifier is set on bipolar mode. It is then transformed by an ADC to be used for the energy-loss determination. The functioning of this ADC module is chosen so that it returns the amplitude of the signal at its maximum, during the time-gate defined by our main gate generator. This gate has to be properly adjusted to contain the signal for the whole drift-time range.

The charge of the fragments is related to the energy-loss signal of the MUSIC, which is approximately described by the Bethe-Bloch equation:

$$-\frac{dE}{dx} = \frac{4\pi N Z}{(4\pi\epsilon_0)^2} \cdot \frac{z^2 e^4}{m_e v^2} \left[ln\left(\frac{2m_e v^2}{I}\right) - ln(1-\beta^2) - \beta^2 - \frac{c_k}{Z} \right] \qquad (2.4)$$

The Z-calibration is technically performed by counting the peaks in the spectrum, starting from the known Z of the projectile.

When an ion is traversing the chamber, it interacts by Coulomb force with electrons of the gas near its trajectory. Electrons very close to this trajectory can receive a large

amount of kinetic energy. These electrons with a large velocity are few because they need to be very close to the trajectory of the ion, but they will populate a wide distribution in space. The drift is set on the x-axis so it will be seen as a wide distribution in x-position. Electrons located further from the trajectory of the ion will get a smaller velocity from the interaction; it means that they populate a rather restrained spatial distribution. A larger number of electrons will then stay in the zone of the interaction with the ion, i.e. near its trajectory. x-position of the electrons are deduced from the observed drift-times. The rare high-energy electrons, strongly kicked by the traversing ion, populate a broad drift-time distribution. After a subsequent charge amplification, each high-energy electron produces a relatively high signal and is therefore inducing large statistical fluctuations on the total energy-loss determination. The corresponding charge flux has a low frequency in the Fourier analysis. On the contrary, low-energy electrons are numerous and confined into a limited region of the active volume around the ion trajectory. The corresponding contribution to the charge-flux signal is a peak of small time-spread. Hence, this peak is described by a high-frequency function in the Fourier analysis.

The main amplifiers that we use are operating the Fourier-transform and act as a selective filter in frequency. Indeed, only signals of the appropriate frequency selected by the filter in the main amplifier are amplified. Therefore, the frequency is set to select the main peak of the signal, corresponding to low-energy electrons, in order to take profit from the greater statistics. The fluctuations event-by-event of the main-amplifier output for a same ion traversing the MUSIC are then reduced, compared to the total energy-loss of the ion in the gas.

The speed of drifting electrons in the chamber is around 5 cm/μs. The distance between the Frisch grid and the anodes is 5 mm, which take then 0.1 μs for electrons to travel. The optimum time-constant for the main amplifier is probably a bit larger, but should be around this value. The amplifiers are not build in-house, so that we could not optimize the shaping-time accordingly. They were tuned to a time-constant of 0.5 μs, which was the shortest available on our amplifiers.

For a given setting of the FRS dipoles, the sum over each anode of the distribution in amplitude of the signals is stored. It shows several peaks, rather well separated. From a setting where the beam is the main ion passing through the chamber, one can identify easily the corresponding peak in amplitude. The next lower charge is contributing to the peak immediately at the left side of the beam-charge peak (a lower charge induces a lower ionization, hence lower amplitude of the signal). The identification procedure goes on peak by peak down to the lowest observed charge for this setting. In the next setting, there should be an overlap of charge-range observed. The matching is not perfect, because the energy-loss is dependent on the ion velocity. The alignment of the peaks between neighboring settings is correcting this velocity-dependence, as well as correcting for small deviations due to temperature or pressure changes in the chamber. Over all settings, we complete a Z-identification of all produced fragments, with a better resolution than the theoretically achievable precision of the total energy-loss. The resolution will be discussed in the chapter 3.

Time channel

The signal dedicated to the drift-time information goes through a fast amplifier, then is treated by a CFD module before being sent to the TDC as a stop signal. The start signal is given as for other TDCs by scintillator SCI4.

The output signal of the fast amplifier is unipolar and negative. Due to some electronic effects (some internal reflections) in this set-up, noise-signal is always observed with an amplitude of the order of 10% of the main signal. To avoid the triggering of the CFD on this noise, one sets a threshold accordingly high (in amplitude). On the other hand, the CFD can handle only signal of amplitude lower than ± 5V. The amplification is limited so that -5V is not reached. These two conditions define the limits of the usable dynamic range per CFD.

This is why the segmentation of the anode of each MUSIC is very important. The segmentation of the anode panel into slats allows to put different detection thresholds on the outgoing channels. There are six slats, but the first and last ones are only used for homogeneity of the field inside the chamber (their signal is not exploited). The four anodes implemented in the data acquisition are subject to individual thresholds in their corresponding CFD to cover different charge ranges: lower charges loose less energy in the gas and produce a smaller signal; the noise-signal is also lower and the threshold can be tuned very close to zero. One can calculate the relative energy loss as a function of the charge, divide the charge range in four intervals and estimate the expected thresholds needed to combine these intervals and cover the whole charge range produced in the experiment. The four thresholds found by this operation are applied on the two MUSICs, so that, for a given fragment charge, there is always one anode from MUSIC1 and one anode from MUSIC2 usable to determine the drift-time.

The combined information on drift-times is used to reconstruct the trajectory's angle in the horizontal plane for spectator fragments.

2.2.4   MultiWire Proportional Chambers

Multiwire proportional chambers (MWPC) are used to check regularly the position of the beam or the centered isotope of interest for a given magnetic setting. This is done to comfort the validity and reliability of the Hall probes given by the dipoles. More specifically, the MWPCs placed at S1 and S3 are used to center the beam, while the ones at the dispersive plane S2 are also required for the SCI2 scintillator calibration. The detectors are not in the beam line during data acquisition, except for the last MWPCs, placed at S4. The interactions with the fragments (energy-loss) would indeed be too important and not easily defined, due to the inhomogeneity of these detectors (caused by the wires). The energy loss would change the trajectory of the fragments in the dipoles. The MWPCs placed at S4 are constantly monitored to track particles, exploiting also their very good stability to correct other detection systems more sensitive to the operation conditions (temperature, pressure, humidity...).

The MWPC is relying on the same principle as the MUSIC, the fact that an ion
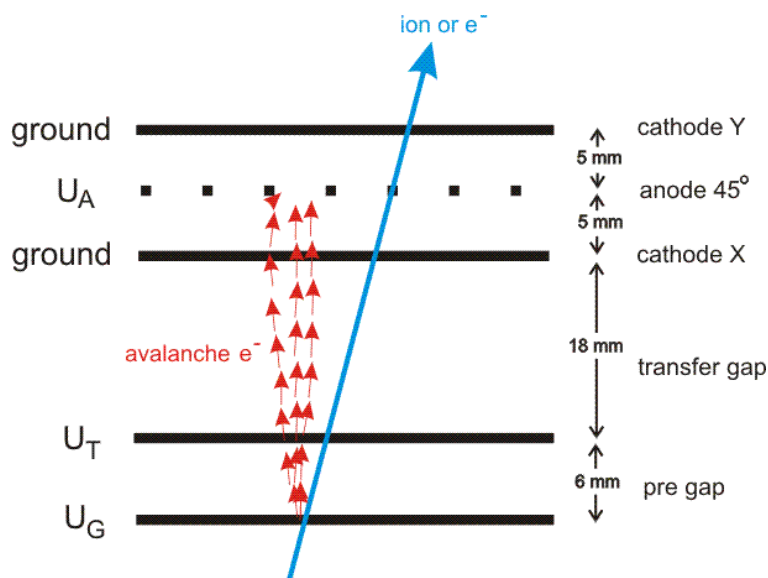
Figure 2.9: Cross-section of a MWPC.

traveling through the volume filled with gas ionizes the atoms of that gas around its trajectory. A schematic view is drawn in figure 2.9. A voltage is applied between anode wires and cathode planes. In fact, cathode planes, surrounding the anodes are also made of parallel wires. One cathode is oriented in x-direction, the other one is perpendicular, all wires being aligned with the y-axis. The wires of the anode are oriented at 45° compared to x or y-axis. The electrons produced along the trajectory of the traversing ion are drifting towards the anode wires. The technical design of these chambers allows to operate a first amplification of the signal by creation of an electron avalanche during the drift. It is the consequence of a high voltage applied in a first stage of the chamber. In our case, fragments are sufficiently charged so that no amplification is needed at this point. This pre-acceleration of the electrons is not turned on in our experiment; we rely only on the main amplification of the MWPC multiplication of electrons near the wires as is explained in the following. Near each anode wire, the electric potential is so that it increases very rapidly with proximity. The incoming electrons are strongly accelerated in these small zones around each wire. They are sufficiently energetic to ionize nearby atoms; this results in the creation of an electron cloud around the wire. This high charge-rise on the anode plane is seen in both cathodes, not through direct hits by the electrons, but by electric induction. This creates the signals in the nearby cathode wires, which provide the information on the x and y position of the ion.

Chapter 3

Data analysis

We concentrated our efforts on data from a ^{136}Xe+Pb experiment at the energy of 1 GeV per nucleon. The measurements took place in February 2004, and the production cross-sections of the projectile-like fragments have already been determined in a previous work [Hen05b]. The aim of that work was the determination of the freeze-out temperature by isospin thermometer method [HAB$^+$05].

The present work is intended as a study of the kinematics and extraction of physical knowledge, from the large number of nuclides produced in the heavy-ion collision (represented in figure 3.1).

We carefully analyzed the data, this time focalizing on our goal of precise velocity studies. Independently from the identification method, there are some specific corrections that are of crucial importance for careful velocity measurements.

3.1   Identification of the fragments

3.1.1   Procedure

The principles of the usage of the FRS to extract high-precision measurements are the following.

The mass-over-charge ratio of an ion flying through a dipole is given by equation 3.1 as a function of quantities that are measured in the experiment:

$$\frac{A}{Z} = \frac{e}{u \cdot c} \frac{B\rho}{\beta\gamma} \tag{3.1}$$

where e is the elementary electric charge, u the atomic mass unit and c the speed of light. B is given by Hall probes, and the radius ρ of the trajectory in the dipole is deduced from the measured position at S2 and S4. This relation is true in each section of the FRS: between S0 and S2, and between S2 and S4. As we will see, we will indeed use this equation in each of the two halves of the spectrometer, with two different purposes.

As already described in the preceding section, the essential information is provided by:
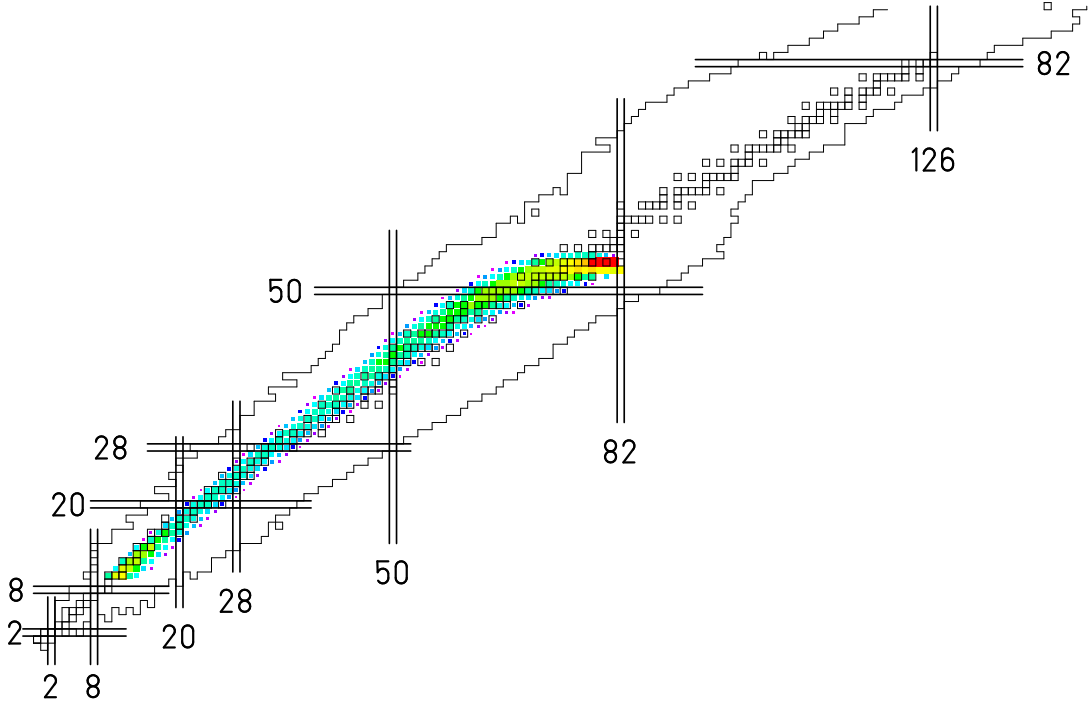
Figure 3.1: Produced nuclides in the reaction ^{136}Xe+Pb at 1 GeV per nucleon in the nuclear chart. Colors indicate the production cross-sections, determined by D. Henzlova. [HSR$^+$]

- the magnetic rigidity in the first section $B_{12}\rho_{12}$ (see equation 2.2)

- the magnetic rigidity in the second section $B_{34}\rho_{34}$ (see equation 2.3)

- the time-of-flight on the section from S2 to S4

- the energy loss in the ionization chamber

By combining the last three pieces of information, it is possible to deduce the nuclear charge Z and the mass number A of every reaction product. The identification proceeds only with the second half of the spectrometer.

The path followed by a given fragment can be corrected for the angle measured with the ionization chambers. The time of flight is known from start and stop detections in the scintillators at S2 and S4 respectively. This information allows us to determine the velocity of the fragment. The term $\beta\gamma$ is then calculated. All necessary quantities entering equation 3.1 are determined, so that one deduces a first estimation of the A/Z ratio of the fragment.

Meanwhile, thanks to the energy deposition in the MUSICs by ionization of the gas described by the Bethe-Bloch equation (see equation 2.4), Z is also determined.

One can build an identification pattern, displaying Z (or the square-root of the energy-loss) as a function of A/Z. The 2-dimensional identification pattern of ^{136}Xe+Pb is shown in figure 3.2, from reference [HSR$^+$].
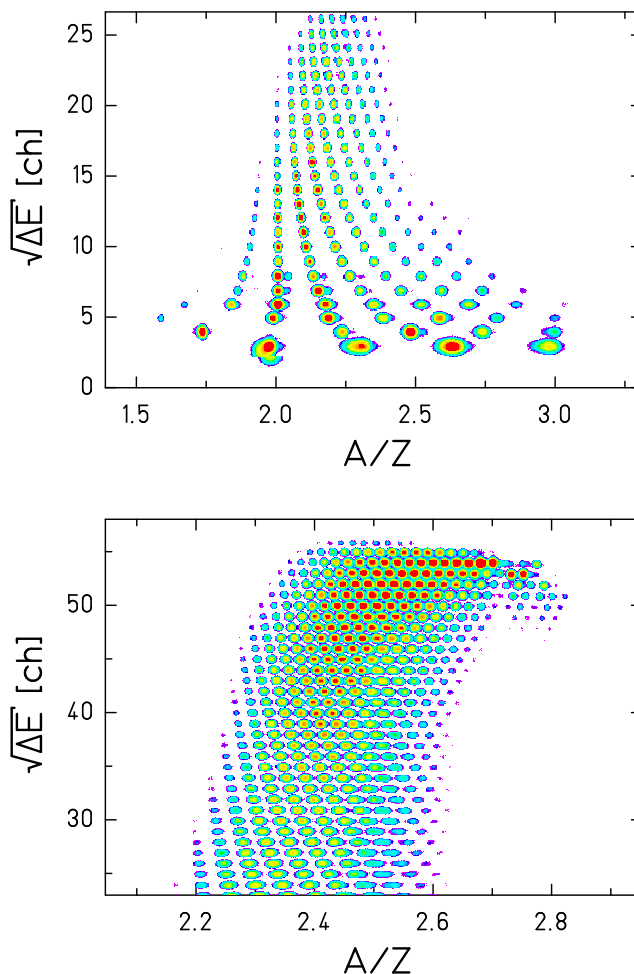
Figure 3.2: Identification pattern obtained with the representation of Z versus A/Z. The upper panel is dedicated to lightest fragments, and the lower panel corresponds to the heavy fragments. Figure for the reaction ^{136}Xe+Pb at 1 GeV per nucleon, taken from [HSR$^+$].

It illustrates that the different nuclides are well separated. The resolution in Z amounts to $\Delta Z = 0.4$ and $A/\Delta A = 400$ (FWHM).

By definition, A and Z are integer numbers. One can from these independent evaluations give them their exact value (by selection of each individual "blob" on the identification pattern). The fragments are then fully identified in atomic number and nuclear charge.

3.1.2 Sources of misidentification

By nature Z and A are integer numbers. Therefore, values ranging from $Z - 0.5$ to $Z + 0.5$ and $A - 0.5$ to $A + 0.5$ are attributed to the nuclide with atomic number Z and mass number A. However, due to the finite resolution, the events in the tails of the distributions of the neighboring peaks in A and Z are misidentified by this procedure.
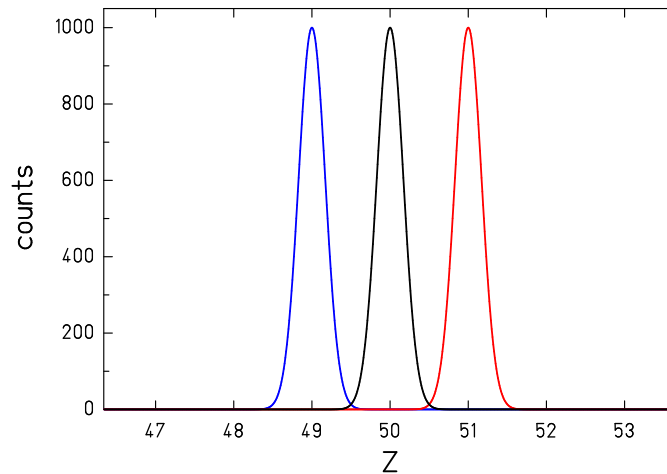
Figure 3.3: Simulation of the Z-resolution of the MUSIC signal, with an assumed FWHM of 0.4.

The probability of misidentification can be estimated by integrating the Gaussian peaks over an interval around the element of interest ($Z = 50$ in the example drawn in figure 3.3). This estimate yields the following results:

The contribution from neighboring elements is independent from Z and amounts to $3\ 10^{-3}$ if they are produced with the same cross section as the element of interest. The contribution from neighboring masses depends on the mass number. For $A = 130$, which is close to the most critical case, the contribution from neighboring masses amounts to $3\ 10^{-4}$. Thus, the main source for misidentification stems from the Z resolution rather than from the A resolution.

3.2 Velocity distributions

3.2.1 Analysis method

In the present work, we will investigate the momentum distributions of the projectile-like reaction products, which are the residues of the projectile spectator. Their velocities are very close to those of the projectile. Therefore, we prefer to express all kinematic quantities in the projectile frame. This makes the discussion more transparent and avoids the complications of the relativistic transformations.

(E/A)lab	ToF	v(lab)	v(proj)
1000 MeV	140.8853 ns	26.2625 cm/ns	0 cm/ns
995.494 MeV	140.9853 ns	26.2439 cm/ns	-0.0800 cm/ns

Table 3.1: Estimated velocity resolution in the projectile frame based on the time-of-flight measurement for a TOF-resolution of 100 ps (see text).

Z	A	(E/A)lab	Brho	v(proj)
54	136	1000	14.2146	0 cm/ns
54	136	999.112	14.2061	-0.0157 cm/ns

Table 3.2: Estimated velocity resolution in the projectile frame based on the magnetic-rigidity measurement (see text).

There are two measured quantities which could be used to deduce the momentum of the reaction products. The most direct one is the time-of-flight (ToF) on the flight path s of about 37 m from S2 to S4. The velocity is given by $v = s/ToF$. We estimate the resolution in velocity in the projectile frame by considering two cases: One product leaves the target with the beam velocity, a second one differs in its time-of-flight by 100 ps, which corresponds to the resolution of the time-of-flight set-up [VBC+95]. The numerical results of this method are listed in table 3.1.

Thus, the time-of-flight resolution of 100 ps results in an uncertainty in the velocity in the projectile frame of 0.0800 cm/ns.

The second procedure relies on the magnetic-rigidity measurement from S0 to S2 and takes profit from the identification in mass and charge of the reaction products (using the other half of the FRS), described in the preceding section. This time, we calculate the velocity difference in the projectile frame between the projectile with a magnetic rigidity corresponding to the beam energy and another projectile with a slightly reduced magnetic rigidity. The difference in magnetic rigidity corresponds to the resolution, which is mainly determined by the position resolution Δx_2 of the scintillator at S2. A maximum value of $\Delta x_2 = 4$ mm (from [VBC+95]) and a dispersion of $D_2 = 6.7$ cm/% (determined during the experiment) was assumed.

The result of the numerical calculation is listed in table 3.2. Obviously, the resolution of the second method, based on the magnetic rigidity, is better by about a factor of five compared to the first method, which exploits the time-of-flight measurement. Therefore, all kinematical properties of the reaction products given in this thesis are deduced from the measured magnetic rigidities of the reaction products in the first section of the spectrometer.

One should mention that this method has a drawback. In the case when the identification in Z and A of the reaction product is not correct, the resulting kinematical properties are erroneous too. The typical error in the velocity of a product with $Z = 54$, $A = 136$ with an energy of 1000 A MeV, erroneously attributed to $Z = 53$, $A = 136$, amounts to $\Delta v(proj) = 0.49$ cm/ns. Fortunately, the fraction of these events is so small that this is

not a severe problem.

Another characteristics of this method is that the magnetic field strength B_{12} enters into the absolute values of the magnetic rigidities:

$$B_{12}\rho_{12} = B_{12}\rho_{12}(central) \cdot (1 + x_2/D_2) \tag{3.2}$$

where ρ_{12} is the radius of the central ion trajectory, x_2 is the horizontal position at S2, and D_2 is the dispersion at S2. For each field strength B_{12} only the ions which fall into the accepted rigidity range of about 3% can be measured. If the momentum range of a specific product is broader than that, the full distribution is obtained by juxtaposition of the different slices of the momentum distributions measured one after the other.

The relativistic kinematical parameter $\beta\gamma$ is then given by the following relation:

$$\beta\gamma = \frac{e}{u \cdot c} \cdot \frac{Z}{A} \cdot B\rho \tag{3.3}$$

which means that the transformation of a given measured value of x_2 scales with the magnetic field strength B_0 and with the ratio Z/A.

The velocity in the projectile frame is obtained by a Lorentz transformation. The full velocity distribution of ^{32}S obtained by this procedure is shown in figure 3.4 together with their individual contributions measured in the different field settings.
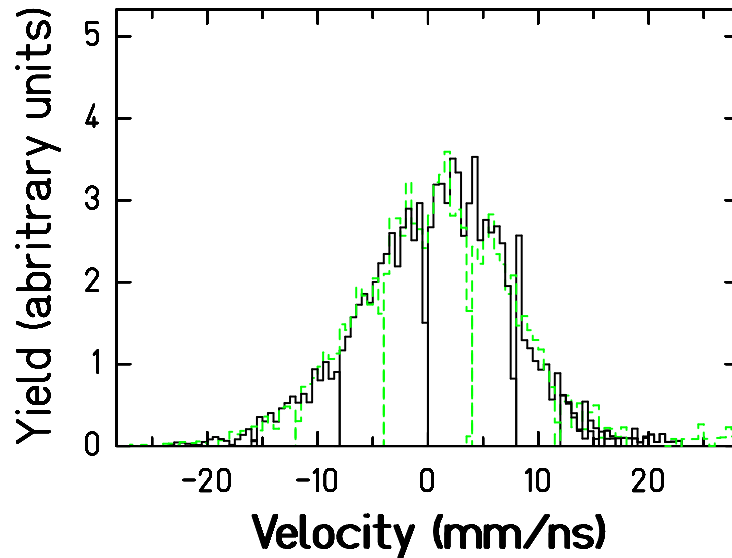
Figure 3.4: Slices of the velocity distribution superimposed from different magnetic settings to reproduce the entire distribution of ^{32}S.

3.2.2 Technical limitations

The velocities in the projectile frame obtained from the relations (3.1), (3.2) and the Lorentz transformation deviate from the original velocity distributions induced in the reaction for several reasons. In the present section we will explore the different effects which add some fluctuations or even shifts to the original velocity values.

Momentum spread of the beam

The projectiles in the SIS18 accelerator occupy a finite volume in phase space. The momentum distribution of the beam has been measured by M. Steiner et al. [SBC+92] under operation conditions similar to the ones used in the present experiment with slow extraction. They obtained a relative momentum width of $4 \cdot 10^{-4}$ at a given moment. In addition, the mean value of the momentum increases by about 10^{-3} from the beginning to the end of the extraction period. The velocity or momentum distribution of all observed fragments are convoluted with the beam velocity (respectively momentum) distribution.

Spatial spread of the beam

The finite emittance of the beam also leads to a finite size of the beam spot on the target. The beam profile is measured by current grids, which are mounted close to the target position. Typically, the size of the beam spot amounts to about 5 mm FWHM. The magnification factor between the target area S0 and the dispersive image plane S2 is around 0.73. From a beam spot of 5 mm FWHM at S0, it reduces to around 3.65 mm in S2.

Energy loss

There are three layers mounted in the target area: the SIS vacuum window, the beam monitor SEETRAM (beam monitor) and the target. As demonstrated by table 3.3, both the energy loss and the nuclear reactions are dominated by the lead target. Therefore, the vacuum window and the SEETRAM will be neglected in the following.

Although the target thickness is rather small, it has to be taken into account for energy-loss corrections. The most accurate method to evaluate the energy loss in the target is to run a simulation code which considers the residue production along the target depth and the corresponding energy loss of projectile and the residue before and after the reaction. One can obtain an approximation with global considerations.

Due to the small target thickness, it is sufficient to neglect the variation of the production cross section and the variation of the specific energy loss along the target depth. Within this approximation, the mean shift of the velocity by the energy loss is taken into account in the analysis program event by event, assuming that the reaction takes place in the middle of the target.

The interactions with the layers of material on the beam axis induces energy loss for all fragments. It results in a shift of their velocity spectrum towards lower values. This is

also true for our reference, the velocity of the beam which loses velocity not only in the target but also in the vacuum window at the exit of the synchrotron and also in the beam monitor (SEETRAM). The impact of the material layers in the beam line on the mean velocities is schematically shown in figure 3.5.
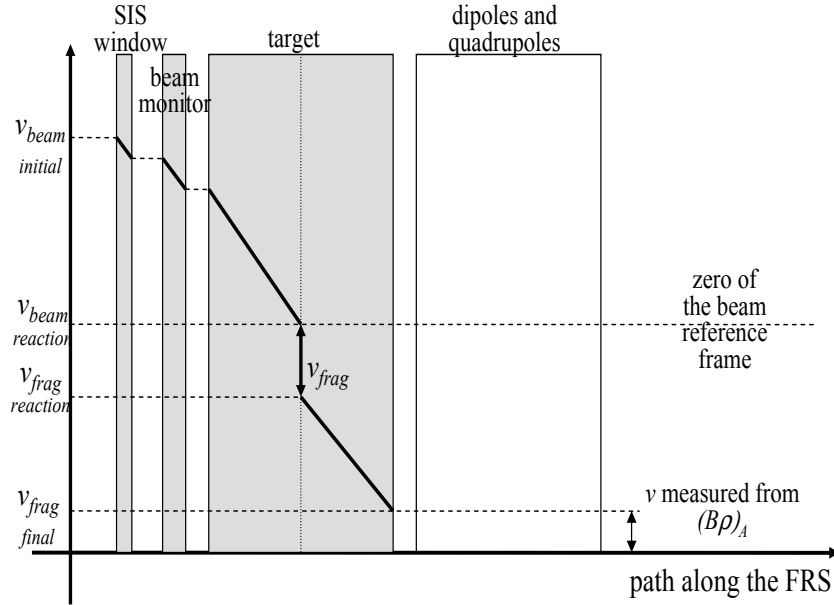
Figure 3.5: Schematic view of the shift in velocity for the beam and fragments due to material layers and target thickness.

Let us consider two specific cases: first, a reaction residue is produced with the same specific energy loss as the beam. In this case, the slope of the velocity decrease of the projectile before the reaction is identical to the slope of the velocity decrease of the residue. This only results in a shift in velocity of the residues behind the target without inducing any fluctuation. Secondly, the produced residue has a different specific energy loss than the beam. In this case, the slopes are different. The extreme case is realized if the residue is very light so that its specific energy loss is negligible compared to the projectile. In this case, even without any velocity change induced in the reaction, the residues populate a rectangular distribution in velocity, covering the whole velocity range of the projectiles inside the target. Under the conditions of the present experiment, this leads to a width in velocity in the beam frame of 0.309 cm/ns. The corresponding values for the residues ^{51}Cr and ^{101}Pd, taken as examples, would be 0.15 cm/ns and 0.0093 cm/ns, respectively. A comparison with the standard deviation of the measured distributions (figure 4.2) reveals that a correction for this broadening never exceeds the 1 percent range. Thus, the broadening of the velocity distributions of the reaction residues due to the energy loss along the target can be neglected. On the contrary, the shift in mean velocity is corrected.

Layer	SIS window	SEETRAM	target
Material	(C)	titanium	lead
Thickness	35 μg/cm^2	13.5 mg/cm^2	635 mg/cm^2
P_{nuc}	4.8 10^{-6}	6.8 10^{-4}	1.204 10^{-2}
ΔE	0.2 MeV	66 MeV	2360 MeV

Table 3.3: Layers of matter in the target area. P_{nuc} the probability of nuclear reactions and ΔE the energy-loss, are given for each layer.

Energy-loss straggling

The energy loss of projectile and residue in the target is subject to fluctuations. This energy-loss straggling is due to statistical different interactions of the traversing ion with the electrons of the material. The result is a conical spread along the mean "trajectory" in figure 3.5. The largest straggling is produced with the heaviest residue. We performed calculations with the program ATIMA, treating the interaction of charged particles with atomic matter. The calculated energy-loss straggling at the output of the lead-target layer amounts to 0.16664 A MeV for the beam isotope itself. Such a shift in energy results in a velocity spread of ± 0.003 cm/ns in the projectile frame. It is thus negligible for our analysis.

Secondary reactions

Projectile-like fragments, produced in the target, may undergo subsequent reactions in the last part of the target. The probability for a nuclear reaction of the projectile (^{136}Xe at an energy of 1 A GeV) in the target (635 mg/cm^2 of lead) is about 1.2% (see table 3.3). On average, this nuclear reaction occurs in the middle of the target-thickness. The probability for a two-step reaction is then 0.0072% if the primary product is close to the projectile and even lower for lighter products. Thus, secondary reactions can be disregarded.

Response of the scintillators

As already mentioned, the position information from the scintillators is provided with an uncertainty of 2 to 4 mm (FWHM), depending on the nuclear charge of the ion [VBC$^+$95]. This translates into a contribution to the relative resolution of the magnetic rigidity of $3 \cdot 10^{-4}$ to $6 \cdot 10^{-4}$. This corresponds to the resolution in magnetic rigidity of the spectrometer.

Chapter 4

Experimental results

In this chapter, we will present the measured longitudinal velocity distributions, in the beam frame, for the most strongly produced nuclides as they are obtained in the experiment. The main aim in this chapter is to provide raw material for comparisons with theoretical models, independently from the interpretation given later in the present work. We shall therefore provide the data without any interpretation. The velocity distributions are directly deduced from the magnetic rigidities for a number of nuclides, which are completely identified in atomic number Z and mass number A.

Let us draw the attention on the fact that the identification and the velocity measurement can only operate on the transmitted fragments. It means that these raw data comprise only those ions which are emitted inside a cone of about 15 mrad with respect to the beam axis, corresponding to the acceptance of the FRS. This geometrical acceptance of the FRS acts as a kinematical cut on the velocity spectra. Thus, the data represent the velocity distributions of the projectile-like fragments under the condition of a kinematical cut. The comparison with a model must take this limited acceptance into account, by application of the same simple and well-defined cut within the simulation.

We chose to characterize the kinematics of the observed fragments through three quantities, in addition to the raw spectra. Of course, we will give some short comments on the characteristics of the measured velocity spectra, and on the chosen parameters to describe them.

4.1 Global variations of the velocity distributions

The great force of these data on the kinematics of projectile-like fragments comes from the choice (and technical possibility) to study the reaction in "inverse kinematics". Due to accelerator limitations, experiments were restricted for long times to the study of target-like reaction products. The available projectiles were limited to light elements, and the study of the fragmentation of various (heavy) elements was done with target-like spectators, changing the nature of the target according to the desired subject of fragmentation. The major drawback is that the fragments need to have a kinetic energy beyond a

certain threshold to escape the target material. Therefore, this type of experiments where calorimeters are placed around the target area provide data with a low-energy threshold.

The heavy-ion synchrotron allows to accelerate many nuclides, that are afterwards fragmented by collision with the target at the entrance of the FRS. Projectile-like spectators have a velocity close to the velocity of the beam. Their escape out of the target material is beyond the threshold (in other words, the target is sufficiently thin so that it is small compared to the mean path of the produced fragments). Thus, our data do not suffer from any low-energy threshold, that would result in a hole in the velocity distributions. Therefore, it makes sense to present the measurements as complete velocity spectra.

Figure 4.1 shows a superposition of the longitudinal velocity distributions in the beam frame for many fragments, selected for their high number of counts. We chose to represent only one isotope for each mass. The evolution from heavy to low mass goes along with a change in shape of the velocity spectra (width, mean value, symmetry) that we shall discuss in the following paragraphs.

4.2   Quantitative analysis of the moments

As a quantitative way to describe, or characterize, the longitudinal velocity spectra, we will present three parameters directly linked with the moments of the first three orders of the distributions. These are objective quantities, calculated with the distributions as they are observed based on their statistical definition. They represent the distributions, without any assumption on the mathematical nature of the distributions. The interpretation on more complex features will be kept for the next chapter. Beside the first moment of the distribution μ which is the mean value, let us remind the definition of central moments of order $n \geq 2$ of the probability distribution of a random variable X:

$$\mu_n = \mathbb{E}([X - \mu]^n) \tag{4.1}$$

$\mathbb{E}$ stands for the expectancy. Let us discuss and comment shortly these first three moments (or related quantities) of the distributions as they are displayed in figure 4.2. We treated most of the distributions, without any requirement on the statistics. This explains that some points show a rather large scattering, reflecting their large statistical uncertainties. Still, the majority of the points lie in narrow bands and show clear tendencies. Error bars are not shown in order not to overload the figure.

4.2.1   Mean value

The mean value of the distributions as a function of the observed fragment mass is drawn on the upper panel of figure 4.2. Due to the slight enhancement of fragments emitted in forward direction compared to backward-emitted fragments by the kinematical cut of the FRS, the mean velocity values of the full distribution are slightly larger than the directly measured values given here. However, this effect is very small and is comparable
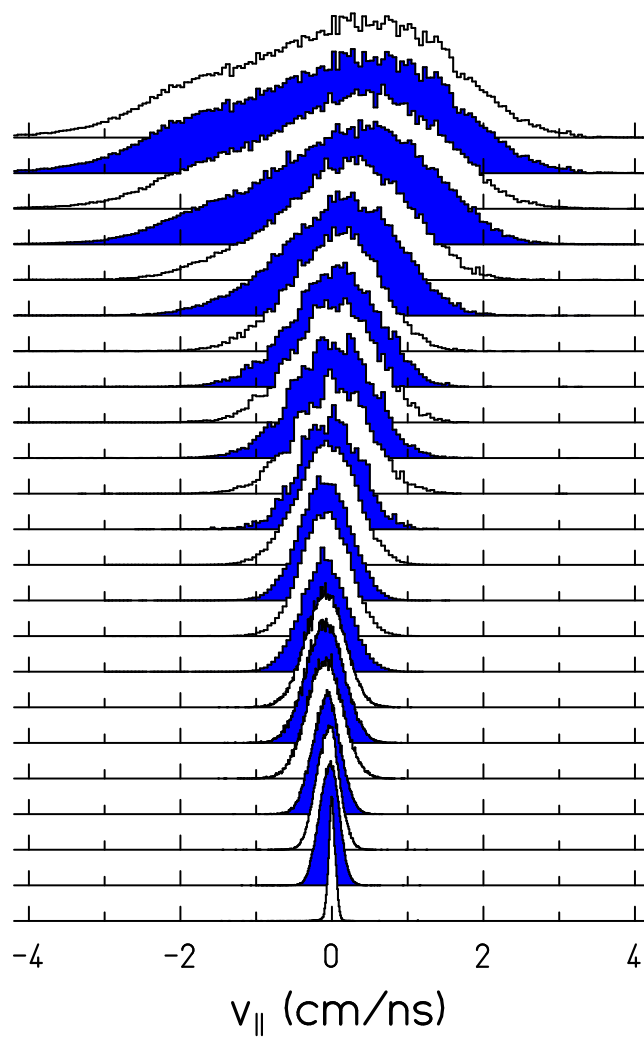
Figure 4.1: Longitudinal velocity spectra, in the beam frame, of the predominantly produced fragments in the reaction ^{136}Xe+Pb at 1 GeV per nucleon ; the lightest fragment is on top ($A = 11$), the heaviest is down ($A = 132$).

with the uncertainty of the data points [Ric04]. The global tendency of the mean value is rather clear, although some fluctuations remain visible, since distributions with low statistics are also included. The values stay in a general sense rather close to zero, which is the velocity of the projectile, by choice of our reference frame. The small variation will need a discussion in the upcoming chapters: the lower values of the mean velocity are reached in the region of half the mass of the projectile. Light fragments seem to have a mean velocity close to the one of the beam, but we will see that the mean value gives only a gross view on the physics, in view of the broad shapes of the velocity distributions of light fragments.

4.2.2   Standard deviation

The standard deviation $\sigma = \sqrt{\mu_2}$ is shown in the middle panel of figure 4.2. Going down in mass, this "width" of the distributions develops in a very regular way. Above a mass $A = 60$, it shows a linear dependence on the mass. Below, the increase gets stronger. The broadest distributions are measured for the lightest fragments.

4.2.3   Relative skewness

The last panel is dedicated to the relative skewness. The skewness is a function of the third-order moment and constitutes a measure of the degree of symmetry of the distribution around the mean value. The relative skewness is relative to the width of the distribution:

$$\gamma = \frac{\mu_3}{\sigma^3} \tag{4.2}$$

Some large fluctuations are observed for the heavy residues. Further investigations should be pursued to check for isotopic effects; mass may not be the best variable for this quantity. Most of the values are anyway very close to zero for intermediate and heavy fragments. On the way to lowest masses, the relative skewness appear to be slightly negative, which corresponds to an asymmetry in favor of low (negative) velocities. This asymmetry could find its origin in a tail of the distributions on the negative side of velocities. We will see in the next chapter that this asymmetry, more pronounced for the very lightest residues, could hint the presence of another process of production.

4.2.4   Discussion

The data presented as they are in this chapter are free of interpretation. They come from raw results provided by our measurement set-up. It is meant as a raw experimental material, to be exploited for comparisons with model calculations, providing the application of the same acceptance in the simulation. We will not stick to these results and provide in the following chapters our own understanding of the observations, and use them to complete our knowledge in this domain.

As a general comment on these raw observables, we can state the following. Although the variations are very small on the first moment, the high-resolution set-up allows to
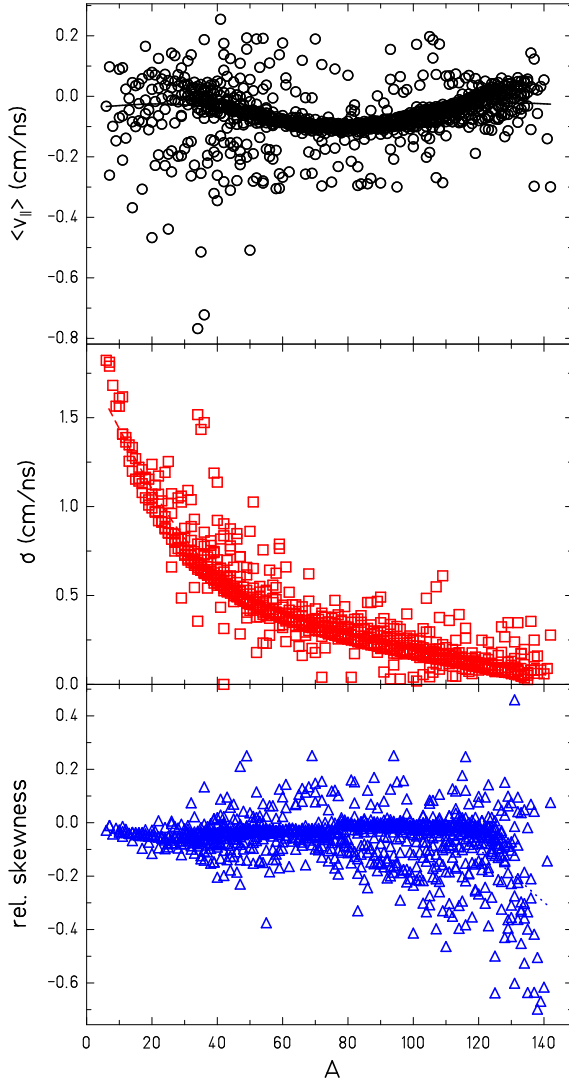
Figure 4.2: Moments of the first three orders of the velocity distributions in the beam frame, as a function of the mass of the identified fragment. Going down from the upper panel, one can see the evolution as a function of mass of the mean value, the standard deviation and the relative skewness.

see two tendencies. From the heavy masses, going down in mass, lighter fragments are slowed down; this systematic slowing down is not followed anymore below masses around $A = 100$ and a second tendency takes over, an acceleration as a function of mass decrease. The second moment does not show the same evolution at all. One can also see two regions in mass where the behavior is different; but the separation does not occur at the same mass. In this case it would rather be around $A = 60$. Finally, the relative skewness presented seems to be almost constant over all the mass range of observed fragments. No strong systematic tendency is to be noted.

These three quantities related to the first moments of the velocity distributions seem quite uncorrelated. It probably means that each of them is not affected the same way by the reaction mechanisms. If these follow different regimes, as is generally accepted (transi-

tion to multifragmentation), they do not translate into universal signatures of transitions and do not touch our observables in all aspects.

To proceed with a physical interpretation of the data, we will need to investigate the variations of the observables with the observed mass.

The mass is the main parameter that drives the evolution of the shapes of the spectra. Some differences between isotopes are seen, especially for light fragments, but the low production cross-sections of these elements also plays a role. This is illustrated by figure 4.3: carbon isotopes show a small variation in width and mean value, but that comes along with a progressively lower statistics. Silicon isotopes seem to populate very similar distributions.
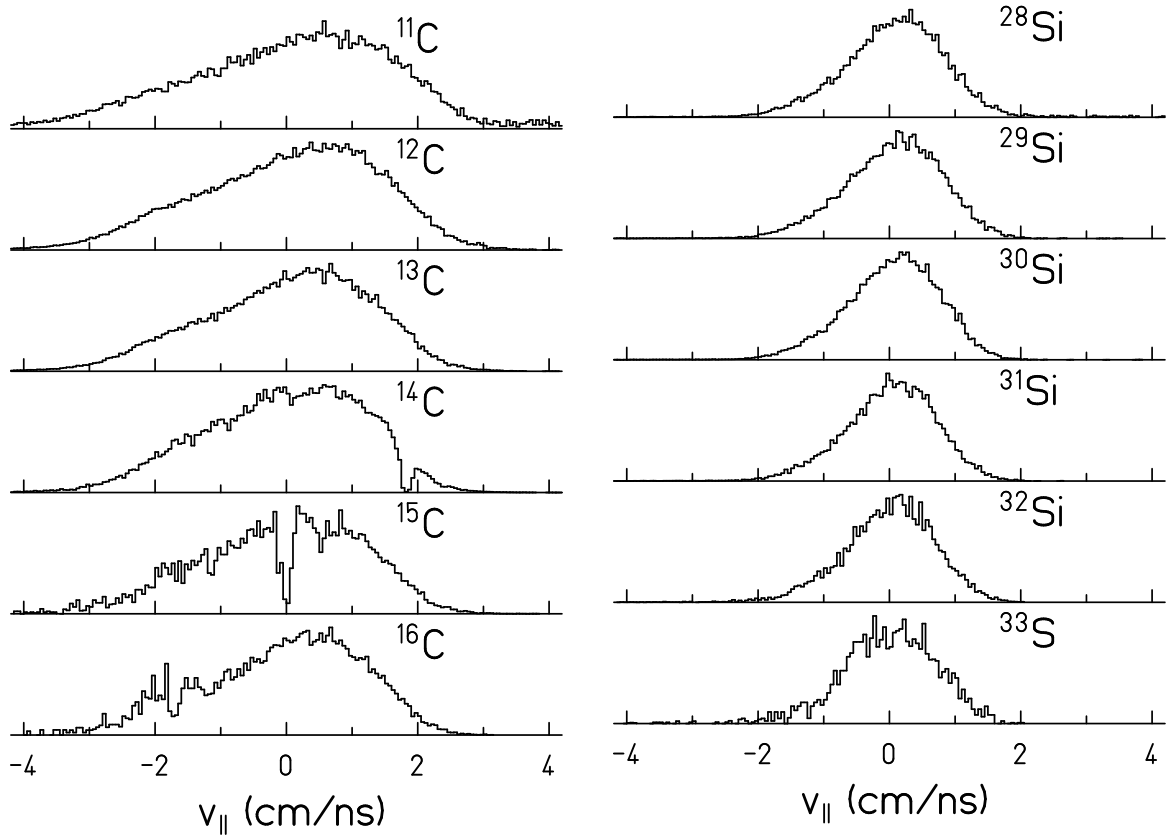
Figure 4.3: Longitudinal velocity spectra for carbon and silicon isotopes.

Therefore, we will consider and try to explain the variations of the longitudinal velocity spectra only on the basis of the mass of the observed fragments. Examples of spectra that will be taken further in this text correspond to fully-identified isotopes, and hence will be labeled as such, but these specific isotopes (e.g. ^{13}C) are chosen for their good

statistics rather than for their charge. The full identification is important, as was already mentioned, for the cross-sections and high-precision velocity determinations.

The spectra show a progression with the mass that does not reflect clearly in the observables shown in this chapter. Lightest residues seem to populate broad, asymmetric shapes that forcefully need interpretations before further treatment. That is why considerations on the global shapes of the distributions are the first task that we will proceed with, in the next chapter.

4.3 Fit procedures

Since the shapes of the velocity distributions of the lightest residues are not sufficiently well characterized by the moment analysis presented in the preceding section, it is the aim of the present section to represent the full line shape by an analytical function. This attempt is pursued for ^{13}C, which is a typical case for the complexity, that the velocity distributions develop for the light residues.

4.3.1 Single-Gaussian fit

A least-squares fit with a single Gaussian curve is chosen as the simplest way to represent the measured velocity distribution by an analytical function. In case of heavy residues, this method gave nice results, as is shown in figure 4.4.
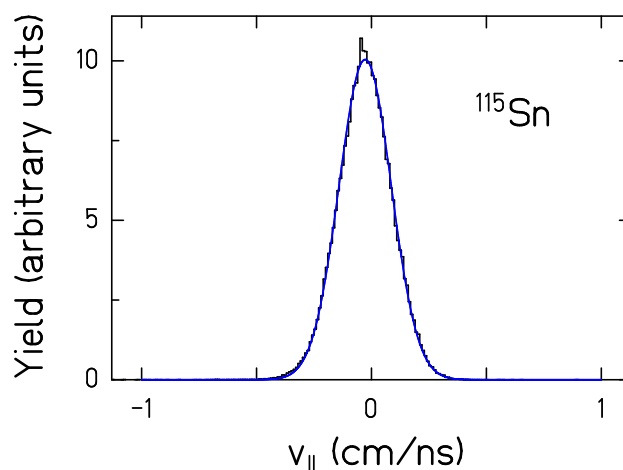
Figure 4.4: Longitudinal velocity distribution of ^{115}Sn fitted with one Gaussian function.

The result for ^{13}C is shown in figure 4.5. The mean value and the standard deviation of the fit curve are very close to the corresponding results of the moment analysis of the measured distributions, see table 4.1. However, it is obvious from the figure and

# Gauss	area	err($+$/-)	center	err($+$/-)	σ	err($+$/-)	χ^2
1	30.5	1.8	0.05	0.08	1.27	0.07	8.87
1	10.4	7.2	-1.2	0.7	0.96	0.37	1.06
2	20.5	7.3	0.6	0.3	0.86	0.18	

Table 4.1: Comparison of parameters obtained as a function of the number of Gaussian distributions assumed for ^{13}C. Velocity values are given in cm/ns.

clearly seen by the large reduced χ^2 value that the Gaussian function is not appropriate to reproduce the line shape. This is no surprise, because the measured distribution is clearly asymmetric.
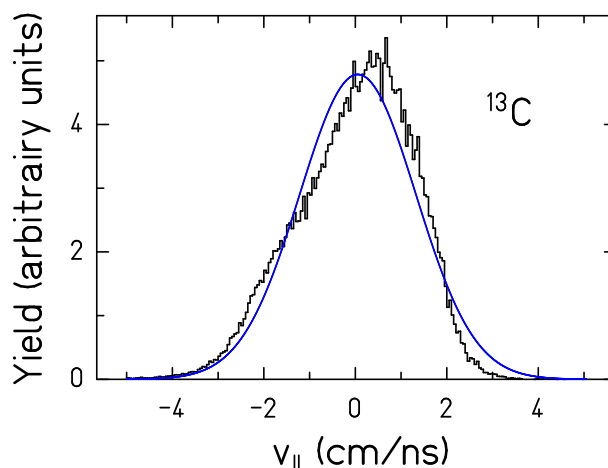
Figure 4.5: Longitudinal velocity distribution of ^{13}C fitted with one Gaussian function.

4.3.2 Double-Gaussian fit

It is tempting to achieve a better reproduction of the measured velocity distribution by choosing a more complex fit function. In particular, the left wing of the distribution hints to the presence of at least one other component, which may be represented by a second Gaussian function. This assumption does not rely on any physical ground, but it is rather intuitive. The parameters after convergence are listed in table 4.1. It is seen by the very good reproduction of the line shape, shown in figure 4.6, and by the value of the reduced χ^2 in table 4.1 which is close to one, that the measured spectrum is very satisfactorily reproduced in this way.

As has already been said, this chapter was meant to provide experimental data, without assumptions, so that anybody interested into this type of reaction products can apply
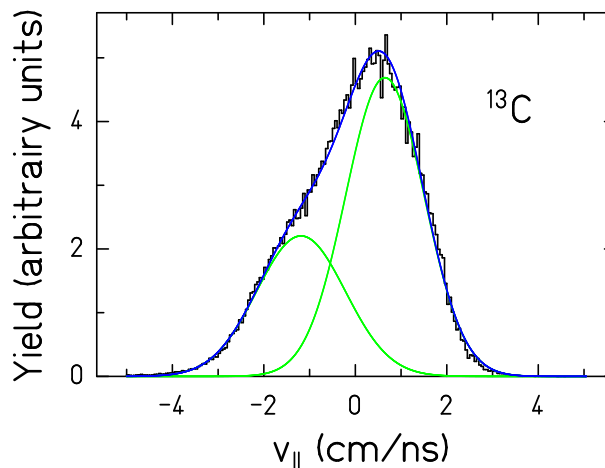
Figure 4.6: Longitudinal velocity distribution of ^{13}C fitted with two Gaussian distributions.

his own interpretation to the available data or can easily simulate the same conditions of our experimental set-up and compare with dedicated models.

In order to enter into the physics discussion and try to extract further knowledge from these data, we can not stay on this level of comprehension. Therefore, in the following chapter, we will follow a complementary approach to the one adopted in the present chapter. It will consist of exploiting the information of the present experiment together with findings from other experiments in order to make a reasonable guess on the properties of the fragments outside the angular acceptance of the FRS. We will see, that this approach leads us to very interesting conclusions, although we are forced to make a few assumptions.

Chapter 5

Interpretation of the global shapes of the velocity spectra

With this chapter, we enter the physics discussion of the experimental results. The shapes of the measured velocity spectra reflect the processes of formation of the fragments. The understanding of the reaction mechanisms and the search for an explanation of the distributions are interconnected.

Figure 5.1 represents the longitudinal velocity spectra of three different fragments, quite representative for the shapes observed in their mass domain. Heavy residues like tin isotopes populate a sharp peak, while lighter residues show more and more variations. For heavy residues, distributions are Gaussian and three parameters are sufficient to define them: the mean value, the width and the integral. The integrals were exploited to deduce the cross-sections by D. Henzlova [Hen05b].

For lighter ones, like ^{13}C in our example, the shape of the distribution looks more complex. The lighter the fragment, the more asymmetric is the distribution, finally revealing a slight hump on the left side for the lightest elements measured.
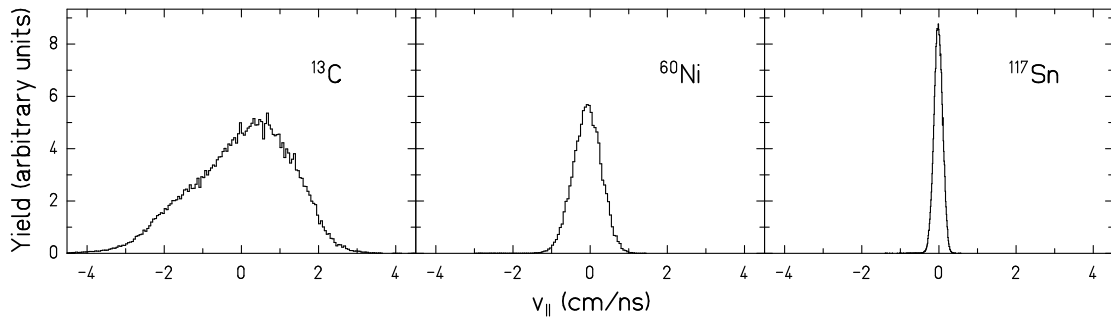
Figure 5.1: Longitudinal velocity spectra in the beam frame for three different fragments.

It is crucial to understand the broadening and the complex shapes of the longitudinal velocity distributions for very light residues to extract properly the physics behind the

mean value and the width of these distributions. There are two ways to extract physics from these observations. Either one is able to distinguish the contributions from known processes and attribute a mean value and a standard deviation to be related only with these known processes. In this case, one can still compare with existing models and predictions.

Or one is even able to address a description of the different mechanisms contributing to the observed shapes and reproduce the spectra. These two options are obviously linked. As soon as the different peaks merge into one complex shape, the understanding of the reaction mechanisms is needed to properly extract the different components.

One aspect of the evolution of the standard deviation of the longitudinal velocity spectra from heavy residues towards lower masses consists of a progressive enlargement. This enlargement is accompanied by a change in the spectral shape, with the appearance of a small second hump for the very lightest fragments identified.

The temptation is great to attribute to these humps two different processes, leading to two different kinds of contribution. Before entering any interpretation, let us consider the knowledge brought by other experiments sharing some features with these observations.

5.1 Aspects of longitudinal velocity spectra of fission products

Naively rather than intuitively, one could make a link between a two-peak distribution and the observations of fission products. One can consider for example ^{238}U+Pb data (energy of 1 A GeV) analyzed by T. Enqvist [EBF$^+$99]. Double-humped distributions are
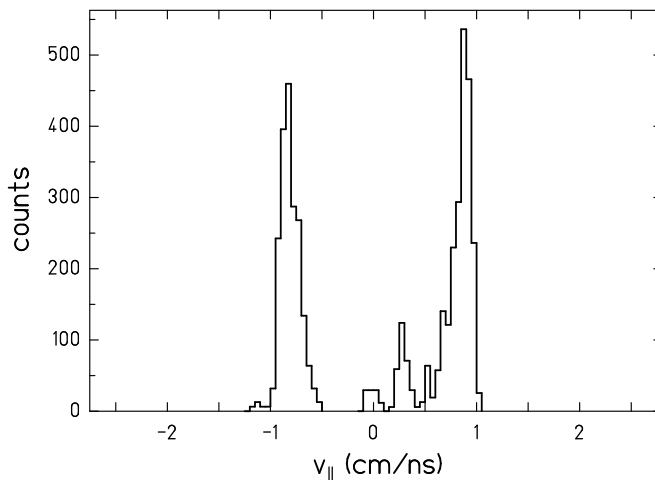
Figure 5.2: Longitudinal velocity spectrum of ^{143}Cs from ^{238}U+Pb at 1 GeV per nucleon.

populated by fragments of mass near half the mass of the fissile nucleus of uranium, like

^{143}Cs as is shown in figure 5.2. These fragments are attributed to symmetric fission events, where the mother nucleus splits into nearly equally massive products. These daughter nuclei are repulsed by Coulomb interaction according to their charges. It induces a shift in their velocity; if they are emitted along the same axis as the beam, one can say that one fission product is accelerated and one is slowed down by the same amount, in the beam frame.

This process is populating a bubble-shaped distribution in velocity space. The selection of a channel of observation around a given angle allows to see, as in the figure 5.2, two peaks in the longitudinal velocity distribution, rather well separated.

5.2   Light residues of very asymmetric fission

Our observations concern exclusively light fragments; it somehow differs strongly from the symmetric fission case. But double-humped structures have already been observed in longitudinal velocity spectra of light residues. Indeed, the analysis of light residues of ^{238}U+p performed by V. Ricciardi [RAB$^+$06] revealed comparable shapes in the spectra. The target was actually composed of liquid H_2 contained between titanium windows; an example of longitudinal velocity spectrum is displayed in figure 5.3.
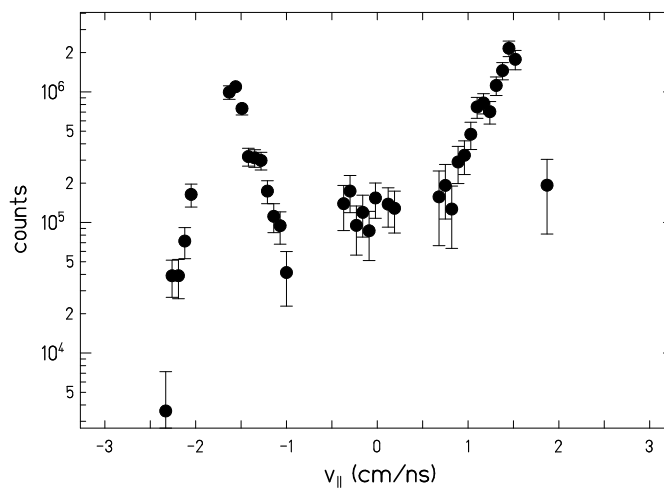
Figure 5.3: Longitudinal velocity spectrum of ^{59}Fe from ^{238}U+H,Ti at 1 GeV per nucleon.

In that figure, the central contribution comes from the reactions with the titanium, while the side peaks are mainly produced by the reactions with hydrogen. We can see that the distance between the two peaks is different than in the symmetric fission. These features for light residues are attributed to very asymmetric fission events. The light nucleus is pushed away by its heavy companion. It offers probably a great similarity with the emission of a light nucleus by the compound system. This asymmetric fission process

is therefore seen by some physicists as a transition regime between evaporation and fission in its classical meaning.

Let us say again that these considerations are only meant to give tracks for the understanding of the observations in our case. Of course, the ^{136}Xe nucleus is much less inclined to fission than ^{238}U. The expected most probable production mechanism for residues is fragmentation-evaporation, in the xenon case. Also, we do not observe, as in the uranium case, two clearly separated peaks in the longitudinal velocity distributions. But let us not forget that the fragmentation-evaporation is also a frequent process in the spallation of uranium.

5.3   Lesson from multiplicity measurements: two production processes

Multiplicity informations on the reaction, as provides for example ALADiN, are of great interest to specify the production mechanism of a given fragment. This type of experiment, with a large acceptance, proves to be a crucial tool for the evaluation of the fragmentation effects on velocity spectra of light fragments. The representation of the cross-sections of the first and the second-most charged nuclei observed in the experiment, displayed in correlation, allows to spot a specific regime of fragmentation: the multifragmentation. Aside from symmetric fission, where both residues are of nearly equal mass
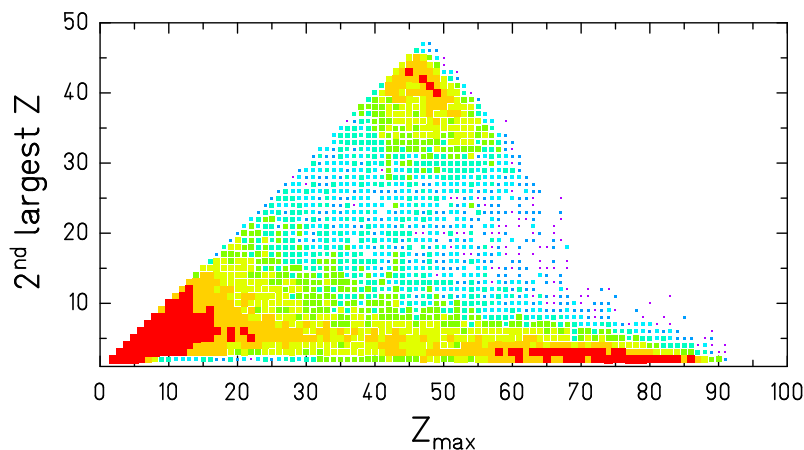
Figure 5.4: Second largest atomic number as a function of the largest atomic number Z_{max} observed in ALADiN experiment for the reaction ^{238}U+Cu at 1 A GeV. Colors depict the relative cross-sections, in logarithmic scale. Figure taken from [Ric04].

(populating the summit of the "pyramid" in figure 5.4), two other types of final configuration are to be seen. First, one can note that in each of these main configurations, light residues are observed. In other words, there are two main processes resulting in

the production of light residues. The lower-right corner of this triangular distribution corresponds to cases when the most charged fragment is heavy, close to the mass -or at least the charge- of the initial projectile. In conjunction to this very heavy residue, there is a very light partner. This constitutes most probably a signature for asymmetric fission events, or more generally speaking an asymmetric binary mass splits.

There is also a concentration of events in the lower-left corner of figure 5.4. This means that a substantial amount of events result in the observation of several light residues, with no large charge. This process type of events is known as multifragmentation.

5.4   Conclusions from xenon spallation reactions

The formation of multiple fragments has a great cost in energy, needed for the surface increase. This phenomenon should appear mostly in rather central collisions, for reactions inducing large amount of excitation energies. In the reaction ^{136}Xe+Pb, this is certainly the main process of formation of light residues compared to a hypothetical asymmetric fission. Yet, this latter contribution can not be completely neglected, as it has been shown by ^{136}Xe+p observations. ^{136}Xe+p data at the same xenon beam energy of 1 GeV per nucleon were analyzed by P. Napolitani [NSTG$^+$07]. As is underlined in Napolitani's work on this reaction, the excitation energy induced by the spallation process (collision with a single nucleon) is much lower than with a lead target nucleus. The geometry of the interaction scheme is also very different. The direct consequence is that multifragmentation is less likely to occur than in the collision with a lead nucleus. Nevertheless, very light fragments are observed. Intermediate Mass Fragments (IMF) emission or fission-like events (with a strong Coulomb repulsion at play) are then the dominant production mechanisms.

Two velocity ranges are populated, giving a two-peaks structure to the velocity spectra as is shown on figure 5.5.

The shape of the longitudinal velocity spectra shows clearly three peaks. It can be understood as a superposition of the two main production mechanisms: multifragmentation and asymmetric fission (or evaporation of a light nucleus).

5.5   Knowledge from re-acceleration observations

Why would the longitudinal spectra in ^{136}Xe+Pb show only two peaks, then, if they are supposed to be three? The major difference is the induced excitation energy by the collision. We said it already, this is higher than in the spallation reaction. The relative importance of the multifragmentation reaction is greater. This would simply lead in a larger central peak, or if the domination was really large, in the disappearance of the side peaks. This conclusion would be true if the mean velocity of the light fragments was the same than the mother nucleus of the binary-decay products, which means in the middle of the gap between the side peaks.

Studies of the mean longitudinal velocity of fragmentation products pursued by V. Ricciardi [REP$^+$03] and later V. Henzl [Hen05a] have shown that very light residues
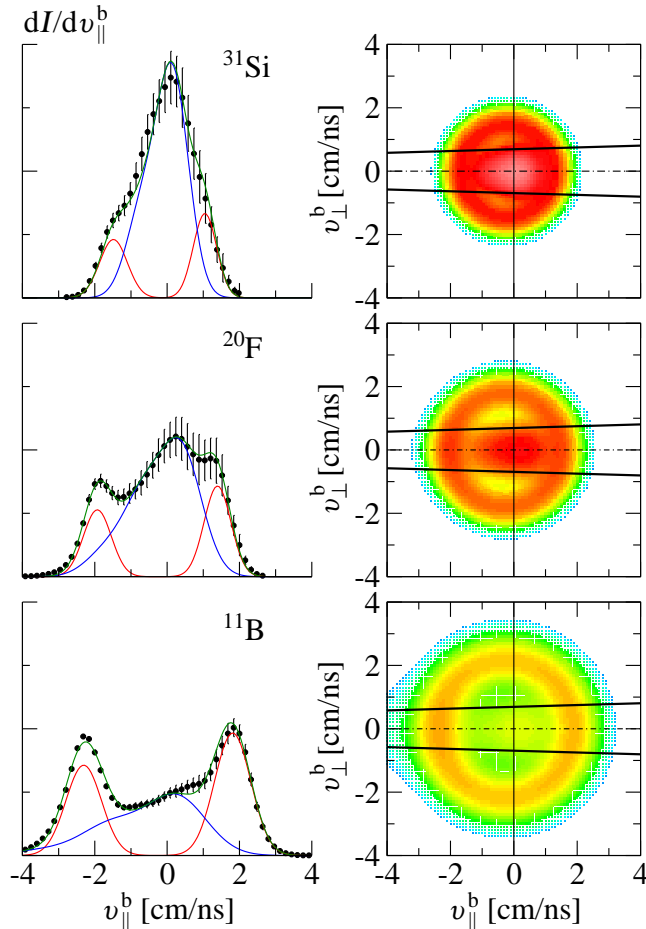
Figure 5.5: Velocity spectra in the beam frame for three different fragments in the reaction ^{136}Xe + p (1 GeV per nucleon). The corresponding (expected) global distributions in the $(\vec{v_\perp}; \vec{v_\parallel})$ plane and the limits of the FRS acceptance are displayed on the right. Taken from [NSTG$^+$07]

of fragmentation are accelerated. The mean longitudinal velocity of such fragments are indeed -very slightly- shifted towards positive values in the beam frame. This contribution is certainly overlapping with the "forward" component of the Coulomb shell induced by asymmetric charge partition. The additional fact that multifragmentation is the dominant process is probably sufficient to justify that, if there is a forward peak populated due to strong Coulomb repulsion, it can not be observed, hidden in the largest peak.

5.6   Simulation with a Monte-Carlo code

In order to evaluate the degree of validity of the considerations proposed above, we dedicated a small simulation code based on Monte-Carlo procedure to generate some velocity spectra. Again the main idea is to assume that in reality, not only two, but three peaks compose the observed spectra. A central component that would correspond to (multi)fragmentation events, plus a "Coulomb shell" populated by very asymmetric fission-like events. Using the parameters set by the user, these distributions are generated in space. A cut is then applied, according to the acceptance of the FRS. In this way,

v_1	σ_1	v_2	v_3	σ_3	w_1	w_{23}
0.2	1	-3	2	0.5	1	1.5

Table 5.1: List of the parameters used for the reproduction of the ^{13}C spectrum as in figure 5.6.

the influence of the set-up is applied to the "original" spectra. Our objective is to show that within our assumptions, the simulated global distribution of produced residues can lead to very similar shapes to what is actually measured in the FRS. The parameters are chosen as follows:

- in accordance with re-acceleration observations, the mean value of the multifragmentation peak is close to zero, slightly positive

- mean velocity of the supposed backward and forward peak so that the mean velocity of the mother nucleus is close to zero or slightly negative

All other parameters (width of the central peak σ_1, thickness of the Coulomb shell σ_3, relative weight of the two process w_1,w_3) are guessed, by small and progressive modifications.

The mathematical description of the central component, is given by the following function, for each coordinate i:

$$\frac{\mathrm{dP}(\overrightarrow{v})}{\mathrm{d}\overrightarrow{v}} = \left(\frac{1}{\sigma_1\sqrt{2\pi}}\right)^3 e^{-\frac{(v_z-v_1)^2+v_x^2+v_y^2}{2\sigma_1^2}} \tag{5.1}$$

The Coulomb-shell component is slightly more complex, and one has to calculate the centroid of the shell and its radius from the given parameters. The position of the centroid is given by:

$$v_{\mathrm{mean}} = \frac{v_2 + v_3}{2} \tag{5.2}$$

The radius of this shell is defined by the following probability density function:

$$\frac{\mathrm{dP}(r)}{\mathrm{d}||v||} = \frac{v_3 - v_2}{2} \exp\left(\frac{1}{\sigma_3\sqrt{2\pi}}e^{-\frac{r^2}{2\sigma_3^2}}\right) \tag{5.3}$$

Let us remain with the example of the spectrum of ^{13}C. After some variations, we could reproduce in a rather convincing way the measured longitudinal velocity distribution, as is shown in figure 5.6.

The values of the parameters used for this simulation are listed in table 5.1.

Due to the geometry of the FRS acceptance, a greater part of the Coulomb shell is transmitted among the forward velocities than in the backward part. This results in a forward peak slightly larger than the backward peak. This inherited asymmetry would never have been sufficient to explain the shape of the observed spectrum in ^{136}Xe+Pb. The position of the fragmentation peak is a much stronger reason for the observed asymmetry;
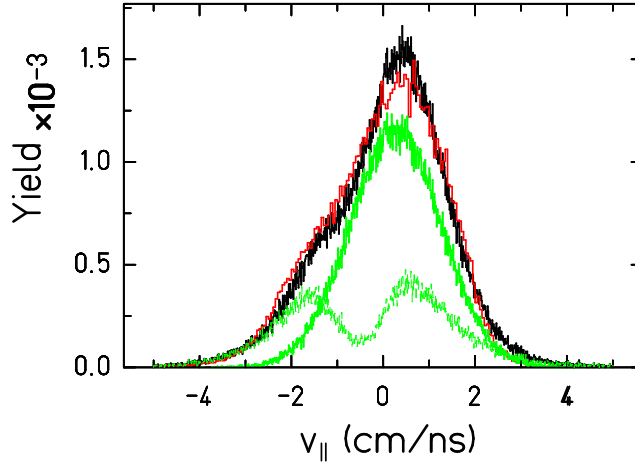
Figure 5.6: Generated longitudinal velocity spectrum (black) adjusted to reproduce qualitatively the measured spectrum (red). The assumed components of the global distribution are displayed in green.

this participates, along with the relative weight, to hiding the forward peak from clear observation.

Slices of the full generated distributions in the plane $(\overrightarrow{v_T}; \overrightarrow{v_\parallel})$ are represented in figure 5.7. The Coulomb shell has a clear ring-shape, that disappears in the sum with the multifragmentation distribution. As a consequence, a large-acceptance detection set-up that would not have access on the emission angle would observe the projection on the longitudinal axis of the total distribution. The result of this projection, which does not contain any cut, is displayed in figure 5.8.

In his PhD thesis, Lindenstruth [Lin93] did not mention any re-acceleration of the light residues. The experiment was performed with ALADiN detector. We have reasons to believe that no deviation from a single Gaussian could be observed in this experiment, and that the mean value determined for light residues is the weighted average of the two processes, asymmetric fission and multifragmentation. The re-acceleration phenomenon in multifragmentation is thus masked to a great extent. Indeed, apart from a slight asymmetry towards negative velocities in the beam frame, the shape in figure 5.8 (projection of the whole distribution on the longitudinal axis) is very similar to longitudinal velocity spectra of heavier residues.

As already pointed out several times, the FRS has a low angular acceptance of 15 mrad. This forced selection on the angle range of observation allows us to study the details of the distributions' shape. The projection on the longitudinal axis of a more significant portion of the global space distribution would hinder the detection of several contributions to the distribution. A large-acceptance set-up that offers an angular segmentation should observe these shapes for a selection within a small range. The present experiment provided longitudinal velocity spectra for fully identified isotopes, of mass and charge larger than what is available from large-acceptance experiments. Therefore, we could not make the

comparison.

We can conclude that, at least on a qualitative level, the assumption of a central (Gaussian) component superposed to a Coulomb shell is sufficient to generate shapes close to observations.

The next two chapters will be dedicated to more specific quantities, the mean value and the width of the distributions. The hints on the reaction mechanisms revealed in the present chapter will not be directly used in the next chapter. The complexity of the spectra of the lightest fragments constrains us to exclude them from our discussion on the mean longitudinal velocity. But it will serve the discussion on the width of chapter 7, providing indications on the reaction mechanisms that also happen for the production of larger fragments. We will finally realize that the knowledge acquired in the present chapter, taken as a model assumption, fits into an intellectual process linking it with the upcoming knowledge of the next two chapters to open new horizons into the comprehension and determination of the reaction mechanisms in heavy-ion collisions at relativistic energies.
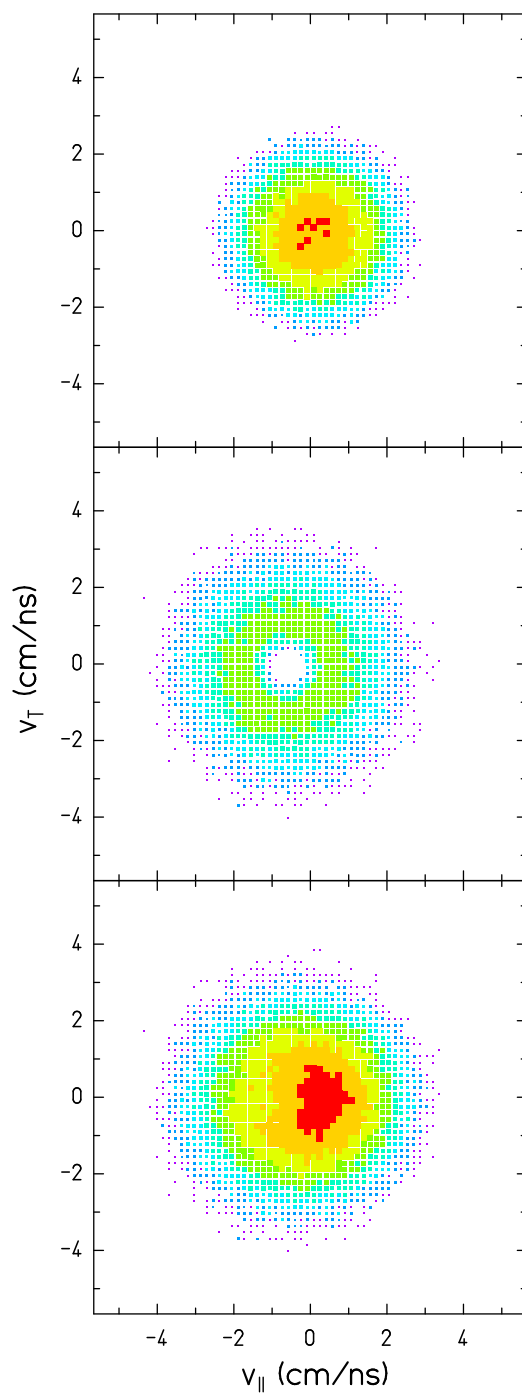
Figure 5.7: Generated distributions with the same parameters (see table 5.1), but without acceptance cut. This time the invariant cross-sections are displayed in the plane $(\overrightarrow{v_T};\overrightarrow{v_\parallel})$. The upper panel corresponds to the central Gaussian component; the middle panel shows the Coulomb shell; the sum is displayed in the last panel (down).
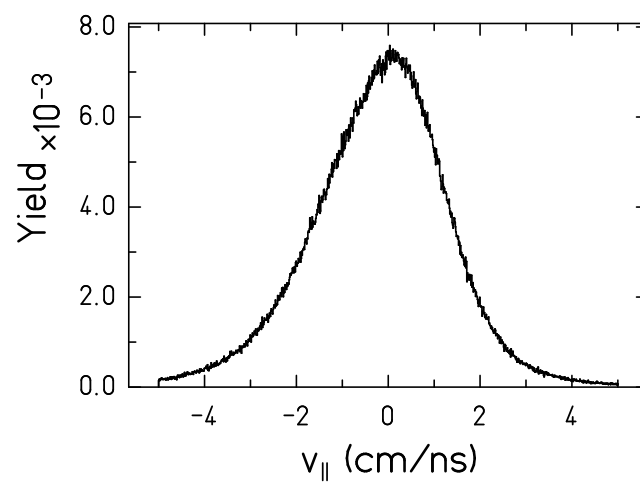
Figure 5.8: Generated longitudinal velocity distribution with the same parameters (see table 5.1), without acceptance cut.

Chapter 6

Mean longitudinal velocity

The mean longitudinal velocity is a sensitive observable to the in-medium nucleon-nucleon cross-section [SDL01]. It is therefore the aim of this chapter to treat the high-quality data obtained with the FRS, in order to offer suitable experimental informations for a direct comparison with dynamical models. Before entering this new treatment of the data, let us present the main observations and knowledge on the features of available data.

As a guide-line for this chapter, we will use the figure 6.1 where the mean longitudinal velocity (in the beam-frame) of the observed fragments is drawn as a function of their mass. The mean value is extracted after a fit of the distribution by one Gaussian. As was underlined in previous chapters, this method is reliable for heavy fragments; therefore, we limited our method to masses above $A = 30$, where the distributions begin to be asymmetric (see figure 6.2). The progression from very peripheral collisions towards more central collisions can be followed from right to left, starting from masses close to the projectile (here 136). Going down in mass is equivalent to going down in impact parameter, and one can intuitively understand that the velocity is decreasing with the observed mass. The collision is more central, so that the overlap between the two nuclei grows, and the spectator residues of this process are more slowed down. This behavior is in agreement with our intuition, considering that the incoming nuclei are bound matter, independently from the actual picture of the reaction, if one thinks in terms of nucleon-nucleon collisions or hydrodynamics.

As one can see in figure 6.1, intuition does not serve the physics all along the mass range: beyond a certain centrality, i.e. beyond a certain mass-loss, the mean longitudinal velocity of observed fragments departs from the first trend of slowing down. It is even clear that the lighter the final fragment is, the greater is its velocity, finally reaching and even exceeding the beam velocity.

One can then divide the behavior of the fragments into two regions, one where a process similar to friction is observed, one where there is a re-acceleration of the spectators.
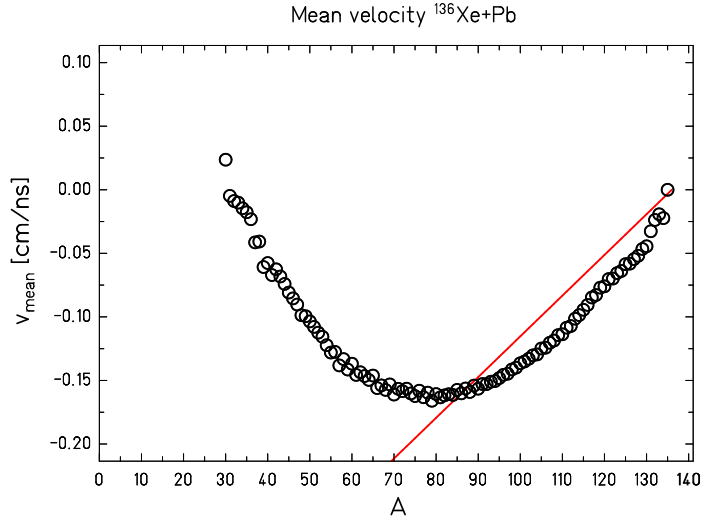
Figure 6.1: Mean longitudinal velocity of observed fragments as a function of mass compared to Morrissey's systematics (red line). The data points represent the weighted average values of the different isobars; the statistical error is of the order of the size of the points.

6.1 Previous use of data on $< v_\parallel >$

6.1.1 Morrissey's systematics for longitudinal velocity

The slope of the right part of picture 6.1 is well described -at least qualitatively- by Morrissey's systematics. In reference [Mor89], Morrissey compiled all available experimental data to compare them in a unique set of units. The author determined an empirical dependence between the momentum shift induced by the collision to the spectator fragment and the mass removal from the original projectile nucleus. In the laboratory frame, he established a best fit of the data for the relation:

$$< P_\parallel >= -8\Delta A \tag{6.1}$$

Transformed into the projectile frame and expressed for velocity, it becomes:

$$< v_\parallel >= -8\Delta A \frac{1 + \gamma_p}{m_p \beta_p \gamma_p} \cdot c \tag{6.2}$$

where m_p is the mass of the projectile, β_p and γ_p are the relativistic factors for the projectile velocity.

6.1.2 Re-acceleration

As seen on picture 6.1, from around one third of the mass of the projectile removed, the data show strong deviations from friction predictions or the Morrissey systematics. Beyond this mass removal, the lighter the observed fragment, the larger again is its velocity, reaching and even topping the beam velocity for the very lightest residues. This
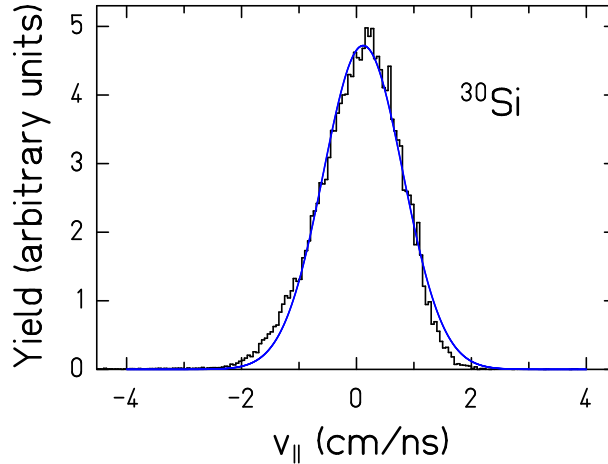
Figure 6.2: Longitudinal velocity distribution of ^{30}Si fitted with one Gaussian.

re-acceleration effect has been first pointed out in reference [REP$^+$03], as an indication of the spectator's response to the participant blast. But the reasons and mechanisms responsible for this effect were explored later on. This very rich physics led to collaboration between our group and theoreticians (namely, Danielewicz).

The re-acceleration is not yet fully understood. It is connected with studies on the Equation of State (EoS), and the global behavior could be reproduced for certain sets of parameters. Momentum-dependent nuclear mean-field seems to be the main ingredient required, in the frame of BUU calculations. It has been the main topic of V. Henzl's PhD thesis [Hen05a].

6.1.3   Velocity reduction for heavy fragments: the friction process

As has already be mentioned in the beginning of this thesis, the idea of a two-step description of the heavy-ion collisions as abrasion-ablation was first stated by Bowman et al. [BST73]. General ideas inspiring Hüfner and collaborators [HSS75] are based on this report. Their model for the friction process in peripheral collisions is one of the earliest, and agrees with measured velocities. The starting point of this model is Glauber's formalism, treating abrasion as a true inelastic process. Glauber's multiple scattering theory [Gla59] was rather convincing and much more competitive than eventual attempts for molecular dynamics, regarding computation times.

It was the intention of the authors to develop a friction model that relies on solid bases and, with the help of very few and reasonable assumptions, provides expressions for abrasion cross-sections as well as mean abrasion-induced excitation energies. No free adjustable parameter is introduced to reproduce the data with formulas that are not dependent from any nuclear model.

The amount of excitation energy introduced in the abrasion process was at that times not well known. It is rather problematic, if the de-excitation stage is not well defined: it is possible to reproduce the data with a too large friction and a too long evaporation chain or vice versa. To their own accord, some systematic discrepancies remain, going beyond the simple abrasion-ablation model. Final state interaction (FSI) is also investigated but the complexity of such considerations does not allow to draw final conclusions other than it is a promising perspective for further developments of the abrasion-ablation model.

With time, some authors proposed evolutions of the friction model, developing further ideas around the FSI. Oliveira et al. [ODR79] compared data with calculations with and without FSI (which they introduced explicitly in their case as "Frictional Spectator Interaction" process) to study its importance and relevance to describe experimental results.

The reaction taken for the investigations in reference [HSS75] is the production of carbon isotopes, whose features (intensities and energy spectra) are compared to the model calculations. The authors speak of a typical excitation energy range due to abrasion between 5 and 15 MeV. We will see in the next section that we have reasons to believe that these estimations give values which are much too small.

Empirical measure of the excitation induced by abrasion

Several authors have underlined a need for higher excitation energies than what is provided by Hüfner's friction model: [Har92], [SBC$^+$93], [Car95].

In Harvey's publication [Har92], the author puts the light on the fact that to reproduce the data with his own Monte-Carlo simulation code [HCLC89], he needs a much higher excitation energy due to abrasion than evoked in the original friction model of Hüfner et al. He refers to 25 MeV per abraded nucleon and compares it with the energy released by the knock out of a 1s-shell nucleon (around 20 MeV).

Using Ir and Pt isotopic distributions produced in the fragmentation of gold, Schmidt et al. developed a now called isospin-thermometer method [SBC$^+$93]. The authors compared cross-section data with different model predictions; among their choices, they tried different excitation energies in the statistical abrasion-ablation model ABRABLA [GS91]. The sensitivity of this model to excitation energies is much higher on the neutron-rich side of the isotopic distributions than on the neutron-deficient side. Events populating the most neutron-rich side of the isotopic distributions correspond to low excitation channels, so to say (cold fragmentation, as referred in [HGS$^+$93]); these correspond to the lower tail of the excitation energy distribution. These cross-sections can then be used as a thermometer to evaluate the excitation energy acquired during the abrasion stage of the collision. The average value lays around 27 MeV per abraded nucleon.

In [HKL$^+$92], there is also mention of excitation energy due to abrasion, and values used in BUU and in the intranuclear cascade code ISABEL [YF79] are given: 28 MeV. But in the calculations named in this article, this quantity is dependent on the centrality of the collision, because different impact parameters lead to different densities of the spectator matter.

All the ideas described in this section point one fact: it is hard to extract deeper knowledge on a selective reaction mechanism (here the first step, the abrasion) from direct results of observations. The experimental data contain potentially coupled signatures of both reaction mechanisms, abrasion and de-excitation processes altogether. We propose a change in the direction of the effort to be put on this matter: instead of refining more and more the models of each reaction mechanism, which are anyway always tributary of an adjustment with data, why not explore ways of presenting the experimental data in a handy way for comparisons with selective theoretical models? Let us explore such a possibility with FRS data, combining for the first time high-precision velocities and production cross-sections over the whole mass range.

6.2 New experimental approach to the nucleon-nucleon cross-section

6.2.1 Motivation

As underlined Zhang et al. [ZLD07], some flow observables determining the nuclear EoS are correlated with the nucleon-nucleon cross-section. Although the nucleon-nucleon cross-section is one of the two main ingredients of the nuclear transport (along with the nucleonic mean field), most studies are dedicated to the mean field. Yet, the nucleon-nucleon cross-section is an important parameter, connected with the nuclear viscosity. It has been shown that dynamical observables, such as linear-momentum transfer, are sensitive to the nucleon-nucleon cross-section, and that this latter varies with impinging energy [Dan02]. Concerning more directly the subject of our work, i.e. the kinematics of spectator fragments, we can refer to a publication of Shi et al. [SDL01]. This article features a study of the change of momentum per nucleon of spectator fragments produced in peripheral heavy-ion collisions in the 1 GeV regime in the frame of BUU calculations. According to the authors, the change in momentum might be considered as a measure of the friction process (which we observe for large fragments). It led to an important observation: the momentum change, dominated by the change in longitudinal direction, is dependent on the nucleon-nucleon cross-section.

In figure 6.3, taken from reference [SDL01], several options are considered for the nuclear EoS inside the BUU model. But what we want to point out with this illustration is that depending on the nucleon-nucleon cross-section, free or reduced to account for in-medium effects, the predictions on the kinematics are different.

The nucleon-nucleon cross-section is an important parameter in the description of the interaction between constituents of the spectator and the participant matter. In particular, it seems that the kinematics of abrasion residues are sensitive to the in-medium cross-section of interaction between nucleons in the overlap zone.

To provide quality data on the longitudinal velocity or momentum of spectator fragments, especially in reactions where the friction process seems to be dominant, is then of great interest for theoretical studies on the nucleon-nucleon cross-section and its reduction
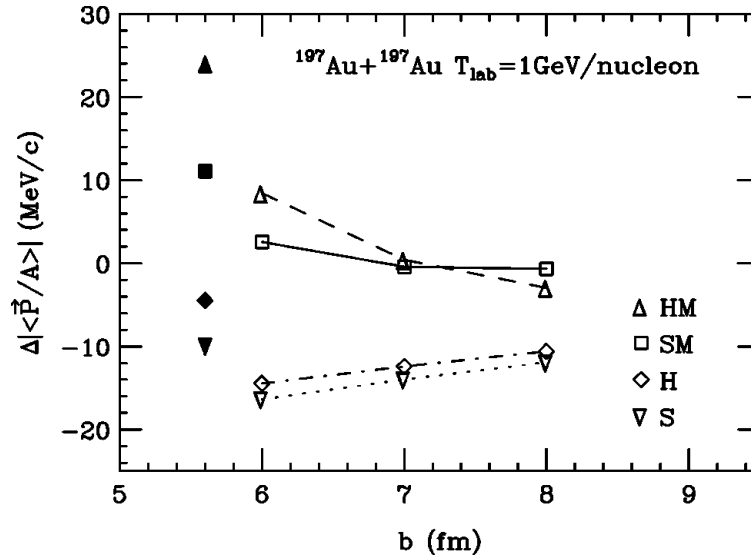
Figure 6.3: Change in the net average momentum per nucleon in the center-of-mass as a function of the impact parameter for different EoS in the frame of the BUU model (S stands for soft, H for hard nuclear matter; M denotes the momentum-dependence of the nuclear mean field). Open symbols are obtained with a reduced in-medium nucleon-nucleon cross-section, while filled symbols are calculated for $b = 6$fm with free cross-sections. Figure taken from [SDL01].

with in-medium effects.

Yet, the available data are not directly suitable for a comparison with theoretical predictions provided by dynamical codes like BUU or QMD. Indeed, these simulations are meant to describe the first step of the collision only. The "output" of such programs is an ensemble of reaction products, including target-like and projectile-like spectators, whose kinematics and excitation energies are given by the interaction process. The precise determination of the excitation energy of the projectile-like spectator, which is of main interest for our study, is not an easy task, because it depends strongly on the definition of spectator and participant matter. The spectator fragments are the pieces of bound nuclear matter that keep, after the collision, a velocity close to their original velocity. The distinction among nucleons can be made easily at large evolution times, i.e. after several 100 fm/c ; the problem is that in these dynamical codes, nuclei can not stand the Fermi motion very long and decay spontaneously after a short while. The distinction between participant and spectator matter must be done rather early, inducing some large uncertainties: nucleons from the participant zone have a large kinetic energy that will increase very strongly the excitation energy of the spectator matter if it is wrongly attributed. Altogether, it makes it rather complex to couple a dynamical description of the first stage of the collision with a de-excitation code.

In this context, we think that searching for a mean to present the experimental informations on the first stage of the collision exclusively is an important and interesting task. The objective of the present chapter is to provide experimental results (mainly mean velocities of projectile-like spectator fragments) as a function of the impact parameter,

a quantity that determines uniquely the first stage of the collision in the frame of the Glauber theory.

6.2.2 Determination of the impact parameter

The slowing down of the heavy spectator fragments, which at first increases with the mass loss, is most probably due to processes happening during the abrasion step. Meanwhile, observed fragments, as we have seen, undergo other decays like evaporation, fission or multifragmentation. The description of these processes is also subject to models and hence assumptions. If we want to be independent from the way these steps are modelized and concentrate on effects mainly due to abrasion, we have to be able to attribute the corresponding impact parameter to the observed fragment. The impact parameter is indeed the key parameter of the abrasion process, defining the overlap between the colliding nuclei. Of course, the observed fragments have undergone at least evaporation, and their mass is not the same as the prefragment outgoing abrasion. But there is a strong correlation, and we assume that for peripheral collisions, the final mass is uniquely linked to a prefragment mass and hence, a certain impact parameter range.

Relation between observed mass and impact parameter

The probabilities of interaction depending on the centrality of the collision can be simply calculated from geometrical considerations. The Glauber model is used to predict the fragmentation cross-sections, as a function of the impact parameter. A density profile for the nucleus has to be chosen to reflect as much as possible our knowledge. A smooth distribution for the nucleus is chosen.

On the other hand, the data on the production cross-sections as a function of mass have been obtained by Henzlova [Hen05b]. These experimental data will be used with Glauber's predictions to build the link between the final observed mass A and the impact parameter b.

One has to be aware that the colliding nuclei may interact in other ways than by purely nuclear interaction. Neutron removal channels by electromagnetic excitation of ^{136}Xe by the Pb nucleus are rather substantial. Yet, these electromagnetic interactions are not considered in Glauber theory. The EM interaction cross-sections were estimated using the simulation code ABRABLA (see figure 6.4). This contribution was subtracted from the measured cross-sections, in order to compare only nuclear interaction products with Glauber's predictions.

The main idea is that for peripheral collisions, where abrasion is a dominant process and evaporation is limited to single nucleons, one can attribute a preferred output channel (final mass) to a given impact-parameter range. To say it in other words, we can assume that there is a bijection between the domain of large impact parameters and the ensemble of heaviest observed fragments.

On one hand, Glauber theory gives a density of probability of nuclear interaction as a function of the impact parameter. The integration of this density function over a defined
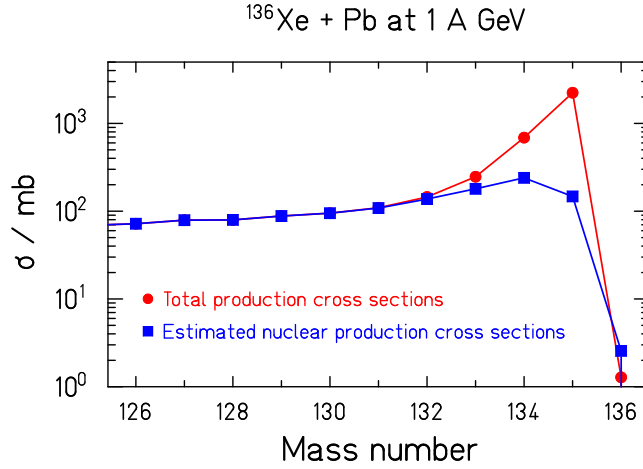
Figure 6.4: Total production cross-sections as observed in the experiment (red line) compared to exclusively nuclear reaction cross-sections (blue line) close to the projectile mass; for the latter, the simulation code ABRABLA was used.

range, let's say for example between 8 and 9 fm, accounts for the interaction cross-section for this domain of centrality.

The common point of these two ideas is at the very heaviest fragment: it is rather surely the one finally produced (after evaporation) from the most peripheral collisions (starting from the largest impact parameter, where the nuclear interaction sets in). This means that within a small range of extreme impact parameters, Glauber theory provides a certain interaction probability that should account for the observed cross-section of the heaviest final residue.

This is why, if we chose the impact parameter interval over which we integrate Glauber's prediction in order to match the observed cross-sections of the final residue, we will be able to link the final observed mass to an impact-parameter range.

Let us give the details of the method. Since we are mostly interested in very peripheral collisions, it is critical to employ a realistic diffuse-surface geometrical cross-section model. In the Glauber approach, the thickness function $Q(b,z)$ is defined as the probability of interaction per unit path length between z and $z + dz$, along the beam axis:

$$Q(b,z)dz = \overline{\sigma}P(b,z)dz \tag{6.3}$$

Here, $\overline{\sigma}$ is the average nucleon-nucleon collision cross-section for the given system, according to [Kar75]. $P(b,z)$ is the overlap of nuclear density distributions of target and projectile for a given impact parameter b and position z along the z-axis. It can be written as follows:

$$P(b,z) = \int \rho_T(b,z,\vec{r})\rho_P(b,z,\vec{r})d\vec{r} \tag{6.4}$$

Here, $\rho_T(b,z,\vec{r})$ and $\rho_P(b,z,\vec{r})$ are nuclear density distributions of the target and projectile, respectively, at the given point in space $\vec{r}$, where the origin of the system of

coordinates is at the target center, and projectile center position is defined by b and z. The probability that the projectile undergoes no interaction at impact parameter b is calculated by:

$$T(b) = exp\left(-\int_{-\infty}^{+\infty} Q(b,z)dz\right) \tag{6.5}$$

The differential cross-section with respect to b is then given by

$$\frac{d\sigma}{db} = 2b\pi[1 - T(b)] \tag{6.6}$$

The shape of ρ_T and ρ_P around the surface of each nucleus is of prime importance for our analysis of peripheral collisions. It is chosen in a way that it closely approximates the charge distribution determined from electron scattering and muonic atom experiments, while allowing an analytical solution for the reaction cross section [Kar75].

Our method is relying on a recursion. For each step (i.e. each mass A), we require:

$$\int_{b_{min}^A}^{b_{max}^A} \frac{d\sigma_G}{db}db = \sigma_A \tag{6.7}$$

For the first step, the upper bound b_{max}^A of the integral of Glauber's prediction is fixed to the largest impact parameter with non-zero interaction cross-section. We apply a variation on the lower bound of the integral (b_{min}^A) down to the value for which the integral matches the experimental value σ_A. This lower bound of impact-parameter range will serve as the upper bound for the next lighter fragment mass $A - 1$, while the lower bound of the integral will be again tuned to match the nuclear cross-section of this next nucleus.

Altogether, this recursive method gives the possibility to establish the dependence between final observed mass and the impact parameter of the collision, down to a certain limit.

The validity of this description is endangered when the strong correlation between b and the final mass is lost. This is certainly the case when fission or multifragmentation sets in.

Our reconstructed dependence between the mass of the final fragment and the impact parameter is drawn as a plain line in figure 6.5. As expected, the largest fragments are produced in very peripheral collisions, above 13 fm. Most part of the mass range is populated by mid-peripheral collisions, with an impact parameter between 10 and 12 fm.

Cross-check with ALADiN data

Large-acceptance settings like ALADiN can deduce the impact parameter from observables like multiplicity of the particles. The ideal domain for this study is mid-peripheral collisions; very peripheral collisions lead to small scattering and some particles, too close to the beam trajectory, are not registered by the set-up. In order to check the validity of
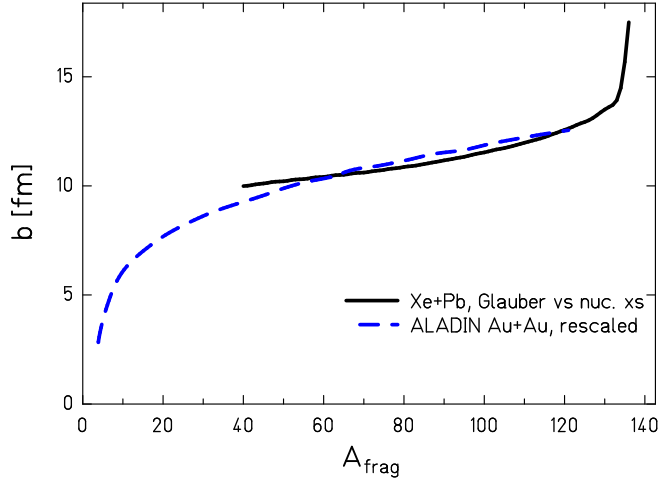
Figure 6.5: Deduced impact parameter as a function of the mass of the fragment. The plain line is our reconstruction of this correlation from Glauber theory and experimental cross-sections. The dashed line corresponds to the correlation established by ALADiN from ^{197}Au+Au data; it was scaled in mass to compare with our system.

our assumption and "reconstruction" of the impact parameter, we have looked for similar data in ALADiN. Alas, ^{136}Xe + Pb has not been studied there and we could only use ^{197}Au + Au data. Actually, we used ALADiN's value of Z_{max}, the atomic number of the most charged fragment observed and after scaling it by a factor 54/79, we attributed the most probable mass corresponding to this atomic number.

The result of this procedure is shown as the dashed line in the figure 6.5. Even if the obtained curve is not exactly matching our estimation for peripheral collisions, it is nonetheless compatible. The slope of the correlation deduced from ALADiN data is close to ours. Below the mass 50, the impact parameter decreases more steeply. Fragments with masses below 20 seem to originate from collisions of small impact parameter, below 7 fm (which is about the radius of the lead target nucleus).

6.2.3   Mean velocity as a function of the impact parameter

Comparison with models

The Quantum-Molecular Dynamics (QMD) model can give predictions on the velocity of spectator fragments. We chose it for our comparison according to the short computation-times (compared to BUU). The centrality of the collision is an input parameter for this simulation, that does not treat evaporation. This model makes assumptions on the nucleon-nucleon interaction cross-sections that may characterize the slowing of the spectators by abrasion. Thanks to our procedure to estimate the impact parameter of the reactions, we can compare QMD calculations with observed velocities as a function of the impact parameter. We also compared the data with the results of the intranuclear

cascade code ISABEL [YF79]. This is shown in figure 6.6.
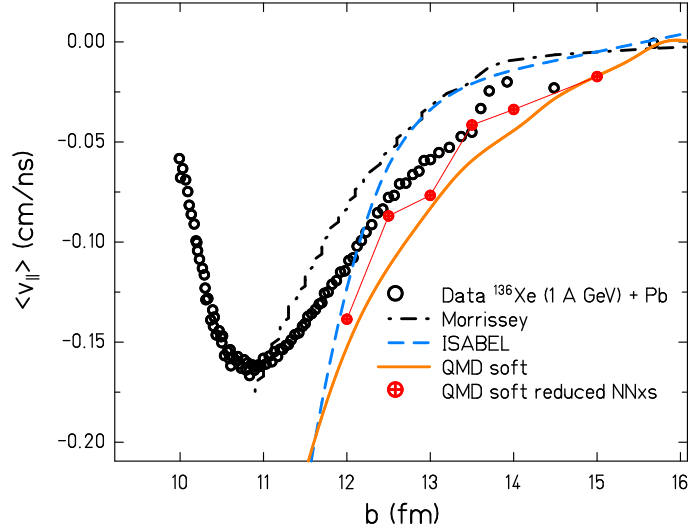
Figure 6.6: Mean longitudinal velocity as a function of the impact paramer from experimental data compared to QMD predictions (using a soft EoS, with and without reduction of the nucleon-nucleon cross-section), ISABEL and the Morrissey systematics.

The intranuclear cascade code ISABEL predicts a very strong dependence of the mean longitudinal velocity on the impact parameter, so that products of a collision with an impact parameter of 11 fm should have a mean longitudinal velocity already in the order of 0.3 cm/ns less than the beam velocity. The same order of mean longitudinal velocity is predicted by QMD. QMD predictions follow the same tendency than our data down to 11 fm, although there is a systematic discrepancy. The calculations are closer to the data points in the most peripheral collisions (above 13 fm). A few points could be calculated for a nucleon-nucleon cross-section reduced by a factor 2. Unfortunately, the low statistics on these values do not allow to draw firm conclusions, but the model seems to show a small sensitivity to the cross-section.

Actual deductions on the new constraints given by these data on the theoretical models are beyond the scope of this thesis. It would require a solid interplay with authors and users of the models, to ensure for example a numerical stability comparable to the precision of the data. QMD has not been extensively developed for our usage, and it would need some investigations to adapt the code and its parameters to reproduce observables as are available in our type of experiment, and to examine the sensitivity to the in-medium nucleon-nucleon cross-section.

6.2.4 Lesson from the spectra of light fragments

The considerations in this section are meant to present some general ideas on the information provided by the FRS experiment about the physics behind the production of

the intermediate-mass fragments in the mass range where complex velocity distributions appear.

It has been mentioned that the strong correlation between the mass of the final fragment and the impact parameter is expected to be weakened or lost for lighter masses. Indeed, the emission of an intermediate-mass fragment in a decay with a heavy remnant (binary decay in most cases) produces a residue with a mass close to the projectile spectator and a light nucleus. Thus, these two products with strongly differing masses originate from the same impact-parameter range. The situation is even more complex, since intermediate-mass fragments can also be produced by multifragmentation, which is supposed to be attributed to much more central collisions, i.e. to smaller impact parameters. Thus, intermediate-mass fragments originate from two very much different impact-parameter ranges. Just measuring the mass of the final fragment in this mass range does not give any distinct information on the impact parameter of the reaction.

However, a closer inspection of the velocity spectra of the light fragments provides us with a very powerful additional information. The two components of the longitudinal velocity distributions of the light fragments, namely the double-humped and the Gaussian-like component, are unequivocally attributed to binary decay and multifragmentation, respectively. Thus, these two processes can be disentangled by considering the two components of the velocity spectrum of each nuclide separately.

First, we would like to consider intermediate-mass fragments produced by very asymmetric binary decay. The recoil of the heavy, not directly observed remnant is reflected by the difference of the forward and backward components in the velocity spectrum of the light fragment, and thus the mass and/or the nuclear charge of this heavy remnant can be determined rather precisely. The neutron excess in terms of N/Z ratio of the heavy remnant, which links the radius of the Coulomb barrier and its height, should not differ much from the N/Z ratio of the projectile. The mass of the emitting source, which is the sum of the masses of the heavy remnant and the light fragment, is close to the mass of the projectile spectator, since particle evaporation before IMF emission is rather improbable due to the strong energy dependence of the IMF decay width. Applying the geometrical abrasion picture, the impact parameter is determined, too. This way, a link is established between the mass of the IMF and the mean impact parameter of the reactions responsible for the production of a certain nuclide by binary asymmetric splits. It is consistent with these ideas that the mean velocities of the two-humped velocity component in the IMF range are slightly negative, just like the velocities of the residues slightly smaller than the projectile.

Secondly, let us consider the products of a multifragmentation process. In this case, several intermediate-mass fragments of similar size are produced simultaneously. It is known from ALADIN experiments, that there is a considerable spread in the sizes of the fragments in one reaction. However, there is also a correlation between the mean mass of the fragments and the impact parameter. These findings, which are connected with the universal rise and fall of multifragmentation [SKW+96], suggest that the mean mass of the fragments decreases if the reaction becomes more central. This knowledge provides the key for understanding the steep increase of the mean velocity of the Gaussian-like

velocity component in the IMF range with decreasing mass, see figure 6.1. By combining the ALADIN results on the sizes and the multiplicities of the multifragmentation products with the mean values of the Gaussian component of the longitudinal velocity distribution measured at the FRS, we can extend our knowledge on the post-acceleration phenomena induced in the abrasion stage to smaller impact parameters.

It becomes evident that the complex velocity distributions in the intermediate-mass range from the FRS experiments contain rich information on the physics of the reaction. Furthermore, the combination of complementary information from full-acceptance and high-resolution experiments seems to be a very promising approach for obtaining new insight into the properties of nuclear matter in extreme conditions.

Chapter 7

Kinematical dispersion

The kinematics of fragment residues is determined by the description or the prediction of their velocity or momentum distributions. The mean value of these distributions is only one aspect of their determination. The width of the spectra -or more exactly the standard deviation- characterizes the kinematical dispersion of the fragments produced in heavy-ion reactions. We have seen that the populated distributions show a progressive evolution of their shape with the diminution of the observed mass. The width of the distributions reflects somehow the influences of the nuclear collision and de-excitation mechanisms.

To be able to predict the kinematical dispersion of the residues would have several profits. First, the process of understanding the reasons for the dispersion forces us to modelize and picture the reaction mechanisms. The comparison between a theoretical prediction and the observations validates or invalidates the chosen hypothesis. In this sense, the research for a description of the kinematical dispersion of fragmentation residues is of fundamental interest. But on the other hand, it has at least two concrete applications.

Some designs for future generations of nuclear reactors are based on hybrid reactors, or ADS (Accelerator-Driven System). The sub-critical core would be brought up to criticality by a neutron supply. These neutrons would come from a spallation target (possibly made of lead), hit by a proton-beam at an energy close to 1 GeV. The kinematical properties and especially the momentum dispersion of the fragments produced in the spallation target are for a great part responsible for aging phenomena. The same holds for the vacuum window (probably made of iron) placed at the entrance of the reactor. Dedicated experiments use spallation reactions (fragmentation of a heavy nucleus by a very light nucleus like proton or deuteron) to measure the reaction cross-sections. The kinematics of the products seem less dependent on the type of target nucleus, and even if the reaction studied in detail is a heavy-ion collision, the features and conclusions of our investigation should give profit to that matter as well. This study is then interesting for the estimation of the life-time of the spallation target under a certain flow of damages.

We have seen that the fragmentation of a beam of heavy ions produces many residues, populating a large range of nuclei across the nuclear chart. It comprises exotic nuclei, far from the valley of stability. In-flight separation of nuclei produced by fragmentation constitutes a technique to provide exotic-ion beams to experimental areas. The quality
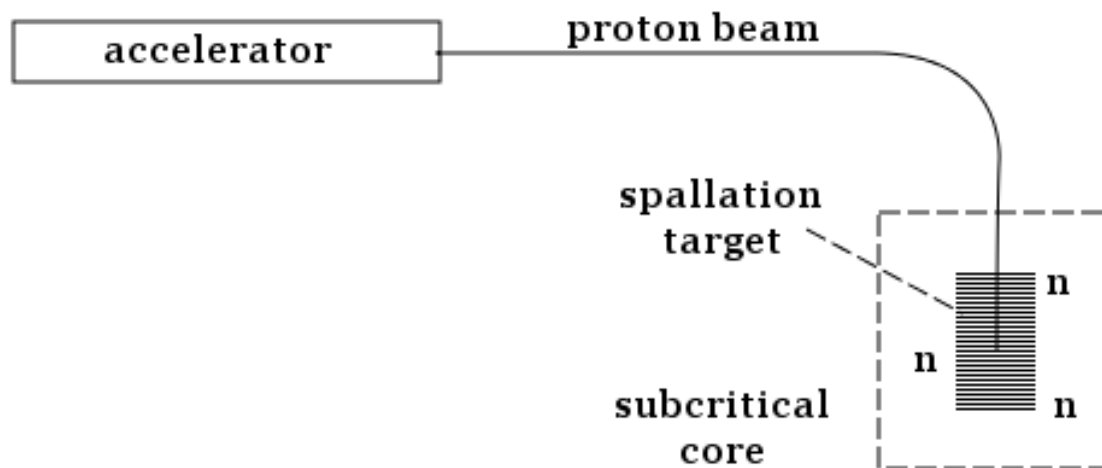
Figure 7.1: Schematic view of an ADS nuclear reactor, concentrated on the neutron supply by spallation reaction using a proton beam.

of such a secondary-beam is defined by different parameters. The intensity of the beam is depending on the fragmentation cross-sections for the isotope of interest. But the emittance is directly related to the momentum dispersion of the chosen species of residues. This defines the acceptance of recoil fragments in the following apparatus; the design of beam lines and recoil separators has to be optimized to avoid intensity losses.

7.1   First models

Dedicated experiments have long shown that the longitudinal momentum of the heavy fragmentation residues follows a Gaussian distribution in the projectile frame. Its standard deviation (the "width" of the spectra) is the subject of a few models.

7.1.1   Goldhaber model

The most often used theoretical model is Goldhaber's prediction for $\sigma_{p_\parallel}$ and σ_{p_T} induced in the abrasion process due to the Fermi motion of the nucleons (see [Gol74]). A proposition of Goldhaber is to consider simply the reaction as a sudden cut-off of the projectile, without taking into account any further evolution of the remaining part of the projectile. Some nucleons are removed instantaneously, without inducing transfer-momentum. This reaction mechanism is referred as the abrasion, and it suggests already a removal of material by friction phenomena, so that its description is probably too simple, but we shall discuss that after considering the strong implications of the assumption made by Goldhaber.

An instantaneous removal of random nucleons from the projectile does indeed affect the dynamical features of this projectile. The abrasion step is contributing to the broadening of the distribution through a simple combinatorial effect. Considering the ensemble of nucleons as a Fermi gas, we know that these constituents of the nucleus have an intrinsic movement, even with a temperature equal to zero. How this internal dynamics should affect observable features of the projectile-like fragments? Of course, since this motion is random, one cannot obtain any constraint on the average momentum of the whole system of nucleons.

But from the idea that the motion inside the projectile is isotropic and the boundary condition that the nucleons hold together, one finds a condition on the average square momenta of the surviving bound matter (the fragment). The σ_p of the fragment is directly related to its average square momentum, and provided the assumption that this broadening is equally distributed in all directions, the contribution to the variance of the longitudinal momentum distribution along the beam axis is one third of σ_p^2. The standard deviation is linked with the Fermi momentum p_F of the projectile of mass A_{proj} and the mass of the fragment after the abrasion process A:

$$\sigma_{p_{\parallel}}{}^2 = \frac{1}{3} \cdot \frac{3p_F^2}{5} \cdot \frac{A(A_{proj} - A)}{(A_{proj} - 1)} \tag{7.1}$$

We can comment that this equation is symmetric regarding to the mass, so that an abrasion process that removes half of the nucleons in the projectile produces the largest width in the distribution. On the other hand, in this hypothesis, light fragments and fragments of mass close to that of the projectile should have a similar broadening of their longitudinal momentum distributions.

This model provides some good predictions, regarding observations. At the time of release of Goldhaber's article, most data available were limited to small mass losses, corresponding to the heaviest fragments, if one measures projectile-like fragments. Among others, ALADiN collaboration also studied the other side of the mass range populated by products of heavy-ion collisions (and spallation). As enlightened in the paper of T. Odeh et al. [OBBB+00], this Goldhaber picture holds not only for masses close to the projectile but also for very light fragments, in the sense that the Fermi motion inside the projectile gives probably the main contribution to the broadening of the momentum distributions. This conclusion comes after a comparison with a different assumption in the description of the reaction between the projectile and the target: if multifragmentation is not sudden, but comes as a mass loss of a thermally equilibrated system, the fragments move according to the Boltzmann statistics with a certain temperature parameter. Observed spectra are not compatible with that option.

However, this model relies on simple considerations that can not predict the overall behavior of dynamical quantities that should reflect more complex properties of the interaction. But still, from the global tendency of the formula, one can conclude that even if the picture is not complete, it represents the abrasion phase in a coherent way. That's why we will take this model as a work-basis. We want to stress out that this model cannot be applicable "as is" to predict dynamical properties of observed fragments. Indeed,

the collision forcefully leads to excited fragments that will loose this energy by further means before being detected. As already said, De Jong et al. [dJIS97] explored this idea by an analytical parameterization of the de-excitation to predict the angular-momentum distributions of spectator fragments, including all reaction stages. But, to our knowledge, nothing similar has ever been done for the linear momentum. The mass A used in the formula (7.1) corresponds to a prefragment. The comprehension of the de-excitation processes of that latter is the key to address a model for the final fragment.

7.1.2 Morrissey's systematics

Another prediction for $\sigma_{p_\parallel}$ often used to compare with the data is the Morrissey systematics for the width [Mor89]. In addition to a prediction for the mean momentum shift, he established a formula for the dispersion around this mean value:

$$\sigma_{p_\parallel}{}^2 = \frac{150^2}{3} \cdot (A_p - A_f) \tag{7.2}$$

The trend of this empirical formula perfectly fitting most data near the projectile becomes unrealistic for lighter fragments. Indeed, the curve does not decrease towards low masses, as seen on figure 7.2. Finally, the prediction gives a non-zero value for very light fragments. One has to realize that being the width for the momentum, it has to go down to zero with mass approaching zero! This simple fit cannot cover the whole range of fragments produced and observed in typical experiments done in our group with the FRS. The need to built up a model based on physical considerations is then obvious.
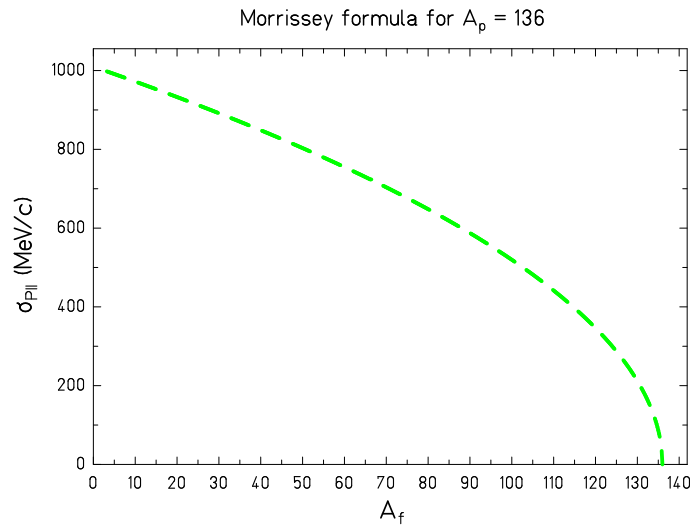
Figure 7.2: Morrissey formula for the longitudinal momentum width, given a projectile mass 136.

7.2   Numerical models

The Statistical Multifragmentation Model (SMM) was developed by Bondorf et al. [BBI$^+$95] to offer a treatment of the multifragmentation process in the de-excitation phase of the prefragments obtained after abrasion in a heavy-ion collision. The statistical model is assumed to govern all properties of the de-excitation channels of the prefragment, and to examine their respective probabilities according to the volume they occupy in the available phase space. In this way, the partition and the kinematics of the products are treated in a consistent way. The main assumption in SMM is that the prefragment, when it enters the de-excitation phase, is in thermal equilibrium, so that thermodynamical quantities can be defined. SMM does not treat the abrasion itself, so one has to couple this model with an abrasion model like ABRA (used in ABRABLA) or an intranuclear cascade code (INC). The code chosen for the abrasion step is providing as an output a prefragment, of mass and charge well-defined, as well as a residual excitation energy.

These features are used as input by SMM, for the starting point of the decaying system. The volume of the system, or in other words the nucleonic density, is an internal parameter of the de-excitation code. With the knowledge acquired by experiments, mainly from ALADiN collaboration, and the determination to reproduce the data, typical values have been deduced for the density.

Using all these parameters, SMM is calculating the volume occupied by each possible partition configuration in the phase space. The volume in this space determines the probability of the corresponding configuration.

If the excitation energy is too low, a surface increase is consuming rapidly the available energy and only few fragments can be produced. The most probable situation is a decay into a single large fragment and few individual nucleons. With increasing excitation energy, the decaying system can form more fragments, of smaller size.

Different channels of de-excitation are in this way included in SMM, multifragmentation but also evaporation, depending on the available phase space.

According to the statistical nature of the SMM model, the kinematics of the fragments is assumed to be governed by Boltzmann statistics. The velocity distribution of the fragments in the frame of the source, which undergoes the multifragmentation process, is the one of an ideal gas with the temperature at freeze-out. An additional contribution to the kinematics of the fragments comes from the Coulomb repulsion between them.

In some other simulation codes, the treatment of the partition into several pieces can be technically achieved using a power-law between the production yield and the charge of the fragments. This was a result of several models, but this law has also been observed experimentally.

The percolation model [FL83, Cam86, NBD$^+$87], which is quite simple to explain, is one of the models that are sufficient to obtain a power-law. It consists of the following. Let an ensemble of A nucleons be. The normal density is by definition 1. All volume unit cells are occupied by a nucleon. The excitation energy induced by the abrasion process results in a volume increase of the system. We divide the volume in unit cells and seed it with the A nucleon in a random way. The produced fragments are composed by adjacent

nucleons after this random distribution over the available space. Repeating the process for a large number of iterations allows to build a statistical tendency: a strong dependence between the yield of each nucleus produced and its mass is observed. The logarithm of the production yield is directly proportional with the logarithm of the mass.

An example of experimental observation of the power law reported by Karnaukhov in [Kar06] is shown in figure 7.3.
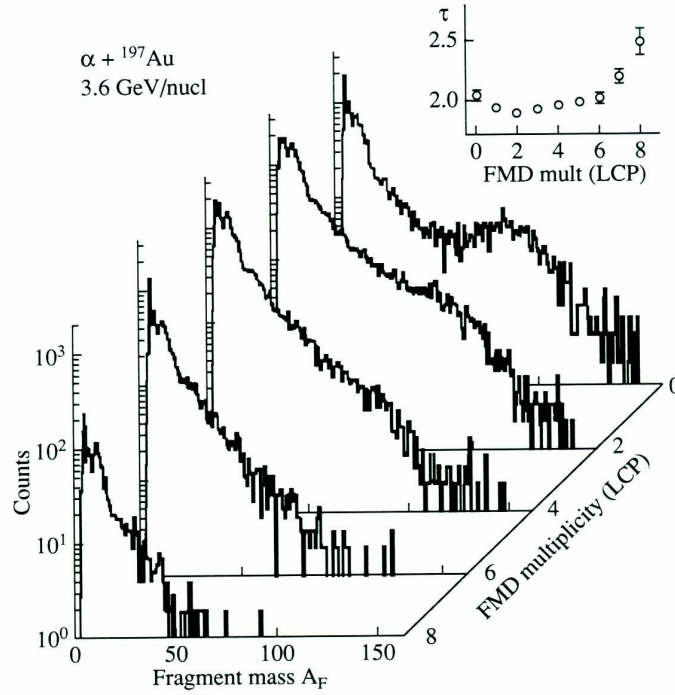
Figure 7.3: Experimental observation of the power-law of fragments multiplicity. This picture is taken from reference [Kar06].

In low-multiplicity events, binary decay products enter the mass distribution. This is clearly seen from the bump in the region of half the mass of the projectile corresponding to symmetric fission, but asymmetric decays also populate the lower mass range. The slope parameter is difficult to extract and does not account for multifragmentation. Above multiplicity 2, i.e. for the three downmost mass spectra, the slope parameter has a value around 2. It increases with the multiplicity, and the slope in the distribution becomes steeper.

7.3 A new complete description

We have seen that the Goldhaber model represents only the abrasion stage of the fragmentation reaction and does not include the evaporation stage, or any other de-excitation process. Therefore, it is incomplete and cannot be expected to account for the properties of the final fragmentation residues.

The following section is dedicated to a new model to try to explain observations in the light of modern knowledge on reaction mechanisms. Let us present these ideas step by step, first in a general context. We will then have the tools to discuss the application of such a model in a simulation code, and achieve the build of a simple formula to predict $\sigma_{p_\parallel}$.

7.3.1   Basic ideas on the different reaction mechanisms

Abrasion

We consider, as Hanelt et al. [HGS$^+$93] and Odeh et al. [OBBB$^+$00] confirmed it for peripheral and mid-central collisions, respectively, that the Fermi motion of the nucleons in the projectile nucleus (or target nucleus) gives rise to a dominant contribution to the spread of the velocity and momentum distribution.

Giacomelli et al.[GSS$^+$04] found an expression of the mass dependence of the Fermi momentum that relies on data from [MSW$^+$71]:

$$p_F(A) = 281 \cdot (1 - A^{-0.568}) MeV/c \qquad (7.3)$$

The Fermi momentum is subject to variations with respect to the nuclear density. In the description of abrasion, it should be the same Fermi momentum as the projectile nucleus in normal conditions, since the nucleons are at normal density.

This density can vary if the volume of the ensemble of nucleons is subject to variations (e.g. due to thermal expansion). Part of the excitation energy induced by the abrasion process can be consumed by the system into volumic expansion. This would lead to a decrease of the Fermi momentum.

Evaporation

De Jong et al. [dJIS97] proposed to include the evaporation process in a formula similar to (7.1) for the angular momentum. The idea was to assume a certain proportionality between abraded mass and evaporated mass, without choosing explicitly a value for the excitation energy. They obtained satisfactory predictions with this only parameter. The typical average value was of two nucleons evaporated per abraded nucleon.

The basic principle that we will reuse is that evaporation has to be treated in addition to previous reaction mechanisms (abrasion), as their consequence.

Regarding to the prefragment, the release of nucleons (mostly individually but also bound) decreases its excitation energy. That is what we will rely on for building the analytical formula, but the evaporation will be fully treated in the statistical model.

Our new ideas are not mostly concerning the evaporation step, even if it is treated with great consideration, being a complex and major process for both mass and excitation energy loss. The major improvement has been to consider the mass shift due to evaporation, between the mass A_{GH} used in Goldhaber formula and the mass A_f of the final fragment (after evaporation).

The importance of the evaporation process has been discussed by Hanelt et al. [HGS$^+$93]. The authors state that the recoil momentum induced by sequentially evaporated nucleons should also influence the width of momentum distributions.

Up to this point, we only considered the consequences of the mass losses, but they are not sole responsible for the broadening of the $p_\parallel$ distribution. We will see that these considerations already describe the global behavior of $\sigma_{p_\parallel}$ but give a rough qualitative model. The further refinement in the description of the processes undergone by the observed fragment is related to the dynamics acting in the evaporation step.

The sequential aspect of the evaporation gives rise to recoil momentum, broadening the momentum distributions. That recoil is strongly dependent on the evaporated particle as well as the mother nucleus. Structure effects and Coulomb barriers have to enter these considerations to estimate the recoil momentum. The simulation code is more suited for that purpose, but we will also try to incorporate that effect in the analytical formula.

Multifragmentation

As was already said in the first chapter, different approaches exist to describe the mechanisms at break-up. The kinematics of multifragmentation products are characterized by a temperature if the cracking system has time to thermalize, or is characterized by the Fermi motion of the nucleons inside the system, if the break-up process is so fast that no thermal equilibrium is reached. The observation of a universal behavior of the mean IMF multiplicity in ALADiN experiments pleads in favor of the thermalization: the multiplicity of IMF always follows the same rise and fall along the mass range, whatever the entrance channels (beam energy, nature of the target nucleus...). Multifragmentation events seem to loose memory of these entrance channels, which is an indication for thermal equilibration before the escape of the various products.

There are several methods to determine the nuclear temperature at break-up. Slope-parameter analysis of the kinetic-energy spectra of observed fragments have yielded corresponding temperatures of the order of 15 MeV [WSP$^+$78, OBBB$^+$00]. This value is much larger than deduced temperatures from population-ratio methods (for example [PMR$^+$95] ; see also the review of several caloric curves by Natowitz et al. [NWH$^+$02]) or thermal-energy approaches [SRBE02]; these methods agree on the order of 6 MeV in temperature. The discrepancy with the kinetic method comes from the supposition in the slope-parameter method that the kinetic energy is determined by a thermal motion. As underlined Odeh et al. in [OBBB$^+$00], the Fermi motion of the nucleons at break-up is leading to a similar energy spectra as the Boltzmann distribution; its corresponding "temperature" parameter is of the order of 15 MeV.

Purely Fermi-motion or purely temperature origin of the kinetic energy is not a realistic choice, and one can expect that even if the breaking system is thermalized, the fermionic nature of the internal constituents of the fragments must play a role.

W. Bauer discussed in an article [Bau95] the treatment of the kinetics of multifragmentation products, depending on the assumptions on the compound nucleus. Whether the origin of the fluctuations of the momentum of the fragments is coming from the Fermi

motion or from a thermal motion, the corresponding probability distribution of the kinetic energy has the same mathematical structure. The standard deviation of such a distribution in energy is directly linked with the temperature or an *apparent* temperature in case of Fermi motion. The finding of Bauer is that one can use this similarity to consider both effects in the formulation of an apparent temperature.

The kinetic energy probability distribution would then be described by a single formulation, using a temperature parameter that has two terms: one that accounts for the fermionic nature of nucleons in the fragment, and one that corresponds to the thermal motion with a real temperature T_{in}. Of course, in case $T_{in} = 0$, the only contribution comes from the Fermi motion and one finds a formula similar to Goldhaber's.

The apparent temperature T_f is given as a function of the real temperature T_{in} through a Taylor expansion by:

$$T_f(T_{in}) \approx \frac{A - A_f}{A - 1} \frac{2}{5} E_F \left(1 + \frac{5\pi^2}{12} \left(\frac{T_{in}}{E_F} \right)^2 + \mathcal{O} \left(\frac{T_{in}}{E_F} \right)^4 \right) \tag{7.4}$$

The author cites typical values for T_f, of the order of 15 MeV, if one considers a reduction of the Fermi energy subsequent to the volumic expansion at break-up. But the additional contribution of the Fermi motion from the abrasion process was not considered, neither is the Coulomb repulsion between products. We will treat these other processes in addition, and use for T_{in} realistic temperatures (about 5 MeV), deduced from thermometer methods not based on kinetics.

The domain of reactions where the multifragmentation will be treated is dictated by experimental measurements of the threshold temperature for this process. In other words, there is a limit in excitation energy under which there are only abrasion and evaporation processes. But beyond this limit, one goes through break-up, followed by a final evaporation stage.

Coulomb expansion

In the previous chapter, we referred to the Coulomb repulsion between charged fragments to explain the shapes of very light fragments. Here we want to consider that the electrical force is constantly at play between protons, present in all nuclear fragments. The IMF emission through a process similar to very asymmetric fission is not the only case where Coulomb repulsion needs to be treated.

In case of multifragmentation, the excited system of nucleons dilates. We shall consider the fact that the expanding particles we are talking about are charged particles. So that the Coulomb forces between charged pieces formed at break-up have to be taken into account.

K. C. Chung et al. developed ideas regarding the effects of this Coulomb expansion in nuclear fragmentation [CDS87]. Their study is made in terms of energy, but we can summarize here the main ideas and results of their article.

Assuming that the expansion is uniform (the radial swelling of the expanding system conditions the evolution of the distance between fragments), but that the size of the pieces

formed is not subject to any variations, it is possible to express the Coulomb contribution to the final kinetic energy. For a fragment of charge Z and mass A, formed at a distance r from the center of a prefragment of mass A_p, charge Z_p and radius R_p:

$$E_{Coul} = \frac{ZZ_pe^2}{R_p^3}r^2(1 - A/A_p)^2 \tag{7.5}$$

Equation 7.5 is remarkably simple, especially due to the fact that the only initial condition considered to be relevant is the relative position of the piece inside the system at break-up. We have seen that other features of the multifragmentation could come into play, coupling with this simple process.

While that kind of contribution can be easily included in a statistical simulation, its inclusion in an analytical model may be more complex, or will require some assumptions. We will come to that matter in the next sections. Let us first summarize in a condensed way the different regimes taken into account.

Repartition of the different regimes over the mass range

To picture clearly the different stages experienced by the spectator matter depending on the degree of excitation reached in the reaction, we can think in terms of excitation energy as a function of the mass of the fragment, and draw the evolution scheme below.
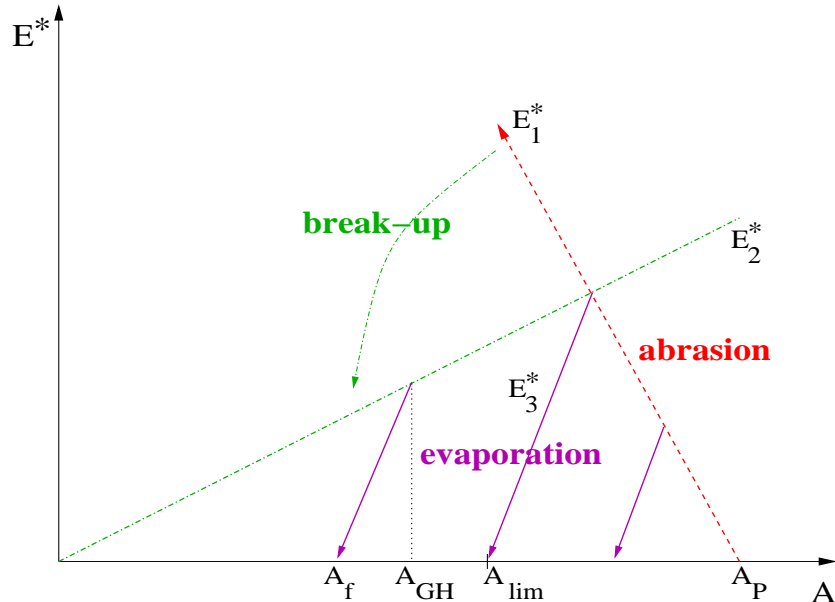
Figure 7.4: Excitation energy of the fragment through its evolution by different reaction mechanisms. A_P and A_f are the masses of the projectile and the final fragment, respectively. A_{GH} and A_{lim} are defined for the use of the analytical formula: A_{GH} is the mass of the fragment at entrance of the evaporation chain; A_{lim} is the mass of the heaviest multifragmentation product possible, as would be finally observed after evaporation.

To follow the evolution of a prefragment, one has to read figure (7.4) form right to left. The first fragmenting process, abrasion, reduces the mass of the prefragment that we are following, inducing substantial excitation energy, according to the line E_1^*. As soon as the system is excited, it has a tendency to emit neutrons, protons and light nuclei through evaporation. It is represented by the arrows E_3^*. But if abrasion has gone far enough, the prefragment severs into many parts. Any of these pieces should enter the evaporation process after equilibrating around the freeze-out line E_2^*.

On the other hand, for a given observed fragment, this picture suggests that if its mass is below a certain limit A_{lim}, it is a product of multifragmentation; if the mass is close to the projectile, above the limit, it should be considered as a simple fragmentation-evaporation residue.

This simple model induces two regions in mass, corresponding to the two regimes preceding evaporation. The mass limit A_{lim} for the final fragment between these processes is determined through the image by evaporation of the break-up limit.

While the transitions between different regimes of reaction mechanisms will be sharp in an analytical formula, as on figure 7.4, they will operate more smoothly in the simulation code.

7.3.2   Predictions using a simulation code: ABRABLA

ABRABLA is an abrasion-ablation model relying on the basic work published in [GS91]. Let us give the keys of the model chosen for each reaction step mentioned before, abrasion, evaporation and multifragmentation. Fission is also included, and is even one great success of this code, but its complex treatment is beyond the frame of this thesis, and anyway not required for the comparison with xenon fragmentation data. The kinematics of the fragments are treated with the same concepts as exposed in the previous section.

Abrasion

The number of removed nucleons by the first stage of the reaction is determined in the frame of the abrasion picture. The centrality of the collision is the main criterion. The ratio N/Z of the abrasion residue can be taken as the same as the projectile.

The original treatment of the excitation energy induced by abrasion was done in the frame of the statistical hole-energy model. The excitation energy is the sum of the energy levels freed by abraded nucleons. In a Woods-Saxon potential, assuming that all energy levels could be with equal probability "touched" by abrasion, the average excitation energy was estimated around 13 MeV per created hole. The initial excitation energy rise due to the abrasion process has been doubled following observations and deductions using the isospin thermometer method [SBC+93]. It amounts finally around 27 MeV per abraded nucleon, in good accordance to the value proposed by Harvey in [Har92], and as confirmed by later observations. The physical reason for such a high excitation energy is not fully understood at present.

Evaporation

The evaporation process is implemented in ABRABLA according to the Weisskopf-Ewing statistical model [WE40]. The basic hypothesis is that due to the large density of levels at high excitation energy (reached by abrasion) and large number of decay channels, the initial conditions of the collision are lost and the evaporation stage is independent from previous stages. The probabilities of emissions are characterized by the level densities and the transmission coefficient. The probability W_p of a certain decay channel p at excitation energy E_i is given as:

$$W_p(E_i) = \frac{\Gamma_p(E_i)}{\sum_i \Gamma_i(E_i)} \tag{7.6}$$

where, Γ_p is a decay width for a given channel p. The decay width, Γ_p, is calculated in ABLA according to the Weisskopf-Ewing formalism [WE40]. In this formalism, the decay width of a given mother nucleus, characterized by its excitation energy E_i into a daughter nucleus by emission of particle p with kinetic energy ϵ_p is given as:

$$\Gamma_p(E_i) = \frac{2s+1}{2\pi\rho(E_i)} \cdot \frac{2m_p}{\pi\hbar^2} \int_0^{E_i-S_p} \sigma_c(\epsilon_p)\rho(E_f)(\epsilon_p - B_p)dE_f \tag{7.7}$$

In the above equation, s is the spin of the emitted particle, S_p its separation energy, $\rho(E_i)$ and $\rho(E_f)$ are the level densities in a mother and a daughter nucleus, respectively, σ_c is the cross section for the inverse process (capture), B_p is the Coulomb barrier for charged-particle emission and m_p the particle mass. In the ABLA code, level densities are calculated according to ref. [JdJC+98]. These properties are deduced from capture cross-sections.

The emission barrier is taken to be equal to the fusion barrier; it is calculated on the basis of the fusion nuclear potential of Bass [Bas, dJ98] and the Coulomb potential [SSB+00].

At the excitations energies well above the Coulomb barrier, the capture cross section σ_c is calculated using the ingoing-wave boundary condition model [KLRM+95], where only a real potential is used to describe the transmission probability of particles:

$$\sigma_c(\epsilon_p) = \pi R^2 \left(1 - \frac{B_p}{\epsilon_p}\right) \tag{7.8}$$

$$R = 1.16\,(A_f^{1/3} + A_p^{1/3}) + \sqrt{\frac{\hbar^2}{2\mu E_{cm}}} \tag{7.9}$$

where μ is the reduced mass and $E_{cm} = \epsilon_p(A_f - A_p)/A1$. Indexes p and f refer to the emitted particle and corresponding daughter nucleus. For low particle kinetic energy the wavelength associated to the particle becomes comparable to the nuclear dimensions, which results in the dependence of the cross section on particle energy; this effect is

incorporated into ABLA via the second term of equation 7.9, which is calculated for the square-well potential.

Considering the fact that first excited states of hydrogen and helium isotopes are high, these nuclei are supposed to be created in their ground state. The total decay width for any IMF is compared to emission width of lighter clusters. Apart from that, the treatment of IMF emission is the same as "simple" evaporation, with the exception that level densities of the daughter IMF are taken into account. The IMF can then enter evaporation.

Multifragmentation

Above an excitation energy per nucleon of about 2.5 MeV, acquired after the abrasion step, a break-up process is assumed to set in. If the prefragment enters break-up, the produced pieces have excitation energies corresponding to the thermal conditions at freeze-out. From mass distributions of ^{238}U+Ti reaction, it was deduced that the average energy loss per lost nucleon in the break-up stage is of the order of 10 MeV. The mass of the followed fragment is determined by the energy loss (i.e. mass loss) needed to reach the energy at freeze-out.

SMM predicts that the ratio N/Z is more or less conserved during the break-up stage. This is the option chosen in ABRABLA to determine the "isospin" of the fragments. This is not in accordance with the two-phases aspect of the multifragmenting matter according to some models. Neutrons may flow to lower density regions, hence leaving the heaviest fragment slightly less neutronic.

Figure 7.5 shows the contributions of the different production mechanisms to the total cross-section. This figure is meant as an illustration of the regions of the nuclear chart populated by the different mechanisms, compared to the observed products. Fragmentation is meant as the large fragment produced in fragmentation-evaporation process. IMF denotes the lighter product of binary decay with $A > 5$. Break-up events count all multifragmentation products, even if they suffered a further mass-loss by evaporation, IMF emission or even fission. These second-step mechanisms are made possible through very energetic events: abrasion produced an excited prefragment that broke into several parts, still excited enough to have significant decay probabilities in these channels.

It is interesting to gauge the importance of each production mechanism, depending on the mass range. In figure 7.6, we plotted the cross-section as a function of A for fragmentation-evaporation, multifragmentation, and IMF-emission events. IMFs are inexistent beyond $A = 50$; this contribution is five times lower than multifragmentation below $A = 20$.

The total production cross-sections can be reproduced with different combinations of the various processes. The light fragments can be produced either by binary decays (IMF emission) or by multifragmentation. In order to quantify the relative weight of the production mechanisms, one needs other variables that carry signatures of the processes. Therefore, the kinematics of the fragments has been included in ABRABLA; this inclusion profits from the ideas chosen for our new description of the reaction mechanisms.
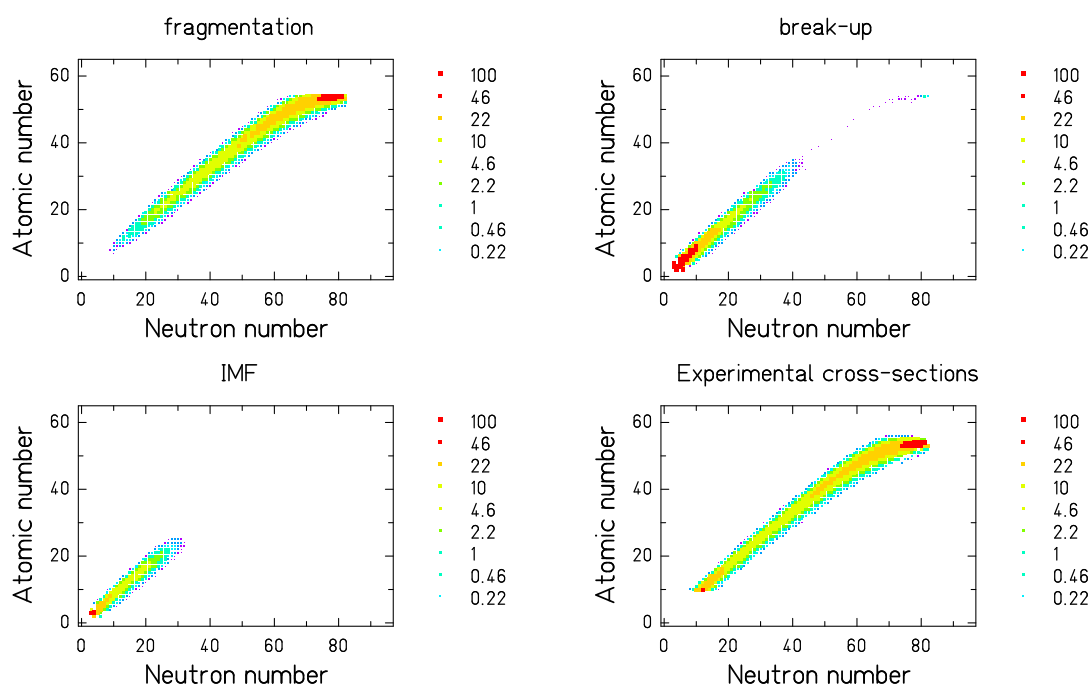
Figure 7.5: Isotopic cross-sections for each production mechanism predicted by ABRABLA, compared to the experimental data (lower-right panel). The panel "fragmentation" refers to heavy residues in fragmentation-evaporation events; multifragmentation products are displayed in the panel "break-up", while Intermediate Mass Fragments enter the panel "IMF".
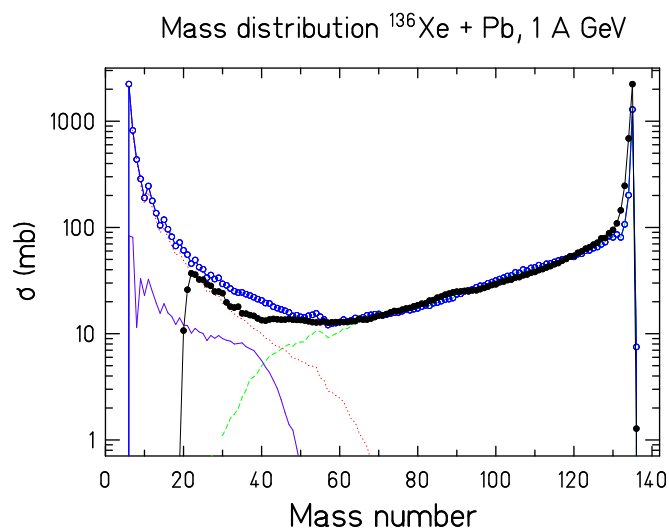
Figure 7.6: Comparison of simulated contributions from fragmentation-evaporation (green dashed line), multifragmentation (red dotted line) and IMFs (deep purple line) as a function of A. The sum of these cross-sections simulated by ABRABLA is shown as the blue points. The experimental cross-sections are represented by the black points.

Inclusion of the new ideas into the kinematics of the fragments

The description has already been made on general terms in the beginning of this section. Let us now stress the specificities and advantages of the inclusion inside the simulation code ABRABLA.

The Fermi momentum of the various nuclei constituted by the fragment through its evolution can be calculated. Among variables, it contains a dependence on the volume or the density of the systems of nucleons. It means that the volumic expansion, as a possible answer of the prefragment to the excitation energy due to abrasion stage, can be taken into account for the estimation of the Fermi momentum. In this way, the contribution of the Fermi motion to the kinematical dispersion comes in two separate steps, the abrasion and the break-up.

Of course, the whole evaporation cascade enters in the code. Recoil-momentum and Coulomb repulsion are individually calculated, for each couple of entrance and decay channel, without the intervention of a global parameter, as we will need for the analytical formula. Not only the biggest residue of each event is followed, but all reaction products.

The simulated longitudinal velocity distribution of the different contributions are plotted in figure 7.7. The limited acceptance of the FRS has been applied to the generated distributions in velocity-space.

Concerning the main topic of the present chapter, the kinematical dispersion, we see on figure 7.7 that the products of multifragmentation populate a broad longitudinal velocity range. The IMFs populate two regions in longitudinal velocity, corresponding to the forward and backward peaks seen due to the limited acceptance of the FRS.

Figure 7.8 represents the standard deviation of the longitudinal momentum distributions $\sigma_{p_\parallel}$ as a function of the mass of the final fragment observed, for the data and for the ABRABLA simulation. The parameters specific of the multifragmentation were a volume expansion of 6 times the normal volume, and a freeze-out temperature around 6.5 MeV. We will see that these values are different than what we will use in the formula; ABRABLA has indeed another constraint, to reproduce the production cross-sections at the same time. The reproduction of the data is of good quality, except maybe an underestimation of the kinematical dispersion of the lightest products. We will return to the discussion about the mechanisms while developing the analytical formula, but we can already state here that the ingredients of our model are compatible with a satisfactory reproduction of the data.

7.3.3   Analytical formula

The inclusion of the reaction mechanisms in an analytical formula is of great interest, for it is due to be more handy than a statistical code for practical applications. Let us repeat that the dispersion of the velocity spectra of produced fragments is important to predict damages in the spallation target for an Accelerator-Driven System (ADS). Furthermore, it will determine the emittance of the produced secondary beam (for example in exotic-beam facilities).
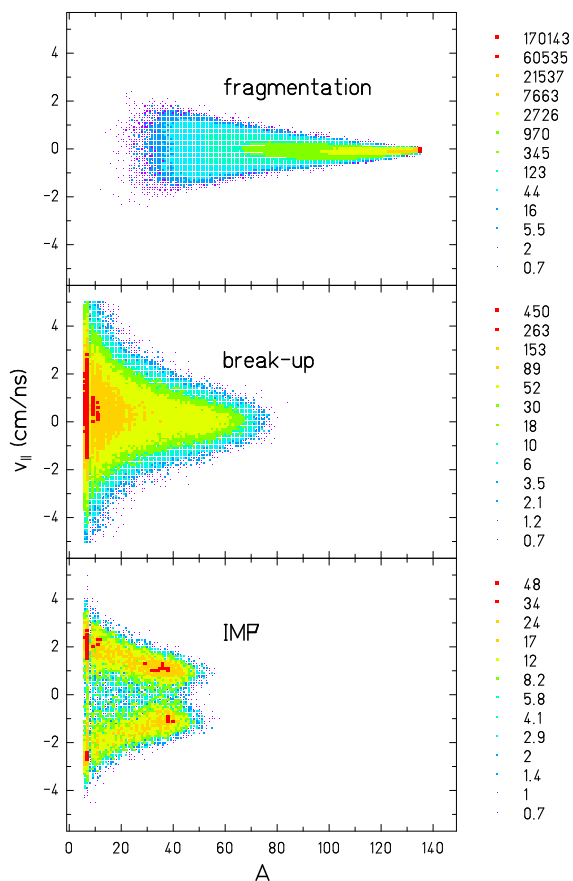
Figure 7.7: Longitudinal velocity distributions of the various reaction products according to ABRABLA simulation, as a function of mass number. The acceptance of the FRS was applied.
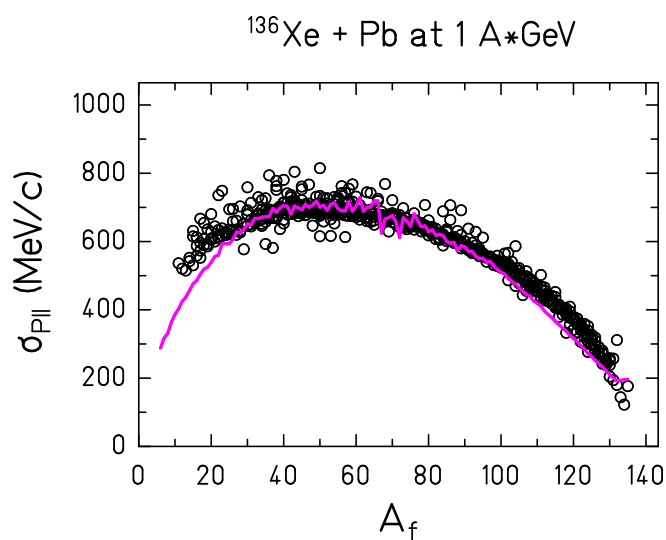
Figure 7.8: Comparison of the simulation of the width of the longitudinal momentum with ABRABLA (pink line) including our new description of the kinematics compared to the data.

To obtain an analytical formula based on a description of the reaction mechanisms, one requires some compromises and approximations. We will enlighten the technical tools used to address a formula more predictive than what is available for now. The specific assumptions dedicated to the establishment of a compact formula predicting the longitudinal (or transversal) momentum dispersion are discussed in the following, one reaction mechanism after the other.

Abrasion

The inclusion of this effect, as it was done by Goldhaber with the formula 7.1, will serve as a basis for further developments.

The main parameter for this contribution, the Fermi momentum of the projectile (respectively target) nucleus, is used as a fixed parameter, only depending on the mass of the projectile (an approximate formula can be found in 7.3).

Let us repeat that this supposes that the projectile is a Fermi gas; the abraded nucleons in the first step of the collision are nucleons well defined in space but with randomly chosen individual momentum, sampled over their Fermi distribution. The contribution of the Fermi motion to the momentum dispersion from the abrasion step is always included, in addition to other effects. This contribution is not considered in SMM.

The gain of energy due to abrasion has been determined experimentally by the isospin-thermometer method [SBC$^+$93] and is taken to be 27 MeV per abraded nucleon.

Evaporation

Taking into account the mean separation energy of one nucleon and the average nuclear temperature inside the prefragment, this "cooling" of the system allowed by evaporation is taken to be 15 MeV per emitted nucleon. This is a rather crude estimation, but this is needed in some way to be able to build an analytical formula.

One has to make a choice for the description of the average behavior and its consequences on the excitation energy of the evaporating system. The value of 15 MeV per evaporated nucleon is close to experimental observations of most light evaporated particles.

On the evolution scheme 7.4, it means that we chose the evaporation lines to be $E_3^* = -k(A_{GH} - A_f)$ with $k = 15$ MeV over the whole mass range. A_f is the mass of the final observed fragment, while A_{GH} is the mass of the prefragment after abrasion or the mass of the heaviest residue of break-up if it occurred. In other words, A_{GH} is the mass of the nucleus entering evaporation, whatever has been its fate before.

Up to this point, we considered simply the mass loss to be responsible for the broadening of the $p_\parallel$ distribution. These considerations already describe the global behavior of $\sigma_{p_\parallel}$ but give a rough qualitative model.

The further refinement in the description of the processes undergone by the observed fragment is related to the dynamics acting in the evaporation step. The sequential aspect of the evaporation gives rise to recoil momentum, broadening the momentum distributions.

Neutrons don't have to overcome any Coulomb barrier, the energy cost for the evaporation of one neutron is its binding energy plus the thermal energy. Protons are more costly to be evaporated, because of the Coulomb force. The difficulty of inclusion of this feature into an analytical model (in contrast to a simulation code) comes from the mass and charge dependence of the Coulomb force. The probability for the emission of light nuclei like alpha particles and lithium cores is not negligible. Their corresponding Coulomb barriers of course differ from those of a single-proton evaporation.

For this approach, we look first at the variance of the longitudinal velocity distributions. If we start from the variance of the prefragment, we may assume that the variance after evaporation of one nucleon is modified by the induced recoil momentum; the additional contribution to the variance is:

$$\sigma_{v_1}^2 = \frac{p_{evap}^2}{(A_{GH} - 1)^2} \tag{7.10}$$

where we suppose that a single particle is evaporated with a mean momentum p_{evap}. A_{GH} is, let us repeat, the mass of the fragment at the beginning of the evaporation cascade, just after abrasion or multifragmentation if it occurred. Evaporation is by definition a sequential process, so that we can treat the evaporation step-by-step, and add up the contribution or influence of each step. To be able to estimate the recoil induced by evaporation, we have limited ourselves to the description of single-nucleon emission. If a prefragment looses n nucleons, these could be bound in a cluster in reality, but we treat it as n times the emission of one particle, with always the same momentum. Then for a number n of emitted particles, we can write:

$$\sigma_{v_n}^2 = p_{evap}^2 \cdot \sum_{i=0}^{n} \frac{1}{(A_{GH} - i)^2} \tag{7.11}$$

For a large number A_{GH} (compared to the number of evaporated particles n), the difference between two steps of the sum is rather small. The sum can then be approximated by an integral. With the upper bound of the integral being $n = A_{GH} - A_f$, we obtain this integrated relation for the final fragment:

$$\sigma_{v_{recoil}}^2 = p_{evap}^2 \cdot \left(\frac{1}{A_f} - \frac{1}{A_{GH}} \right) \tag{7.12}$$

The momentum variance is linked with the velocity variance by:

$$\sigma_{p_{recoil}}^2 = A_f{}^2 \sigma_{v_{recoil}}^2 \tag{7.13}$$

In order to compare explicitly this momentum recoil with the Fermi momentum, we expressed p_{evap} as a function of the mean individual longitudinal momentum taken by Goldhaber: $p_{evap} = \eta \cdot p_F / \sqrt{5}$. η is not easily estimated, because it depends on the charge of the mother nucleus (the prefragment of mass $A_G H$), and of course is different for each type of particle is evaporated in reality (neutron, proton, alpha, IMF...). We have estimated

the Coulomb repulsion felt by a proton and considered the thermal contribution to the kinetic energy for protons and neutrons. We obtained an average recoil per evaporated nucleon, assuming that neutrons and protons are evaporated in same quantities. η is this mean recoil, scaled to the mean energy of the fermions.

$$\eta^2 = \left(\frac{1}{2} \cdot 8 + \frac{1}{2} \left(8 + \frac{1 Z_p e^2}{r_0 (A_p^{1/3} + 1)} \right) \right) / 20 \tag{7.14}$$

Using this new expression, we write:

$$\sigma_{p_{\parallel recoil}}^2 = A_f^2 \cdot \frac{p_F^2 \eta^2}{5} \cdot \left(\frac{1}{A_f} - \frac{1}{A_{GH}} \right) \tag{7.15}$$

$\sigma_{p_{\parallel recoil}}^2$ represents the contribution from the recoil of evaporated particles to the variance of the longitudinal momentum. This term will be added to other contributions in a final formula, but let us treat other processes before writing the complete formula.

Multifragmentation

The limit for break-up processes is symbolized by the line E_2^* in figure 7.4. Its slope is characterized by the temperature at freeze-out. The temperature T_f at freeze-out for the formation of multiple fragments is estimated around 5 MeV [SRBE02]. The relation between temperature and excitation energy is described by the following formula:

$$E^* = aT^2 \tag{7.16}$$

In this equation, a is the level density parameter ; its value is around $A/11$. If one assumes a critical temperature of 5 MeV for the limit, $E_2^* = \frac{25}{11} A$.

Our model induces two regions in mass, corresponding to the two regimes preceding evaporation. The mass limit for the final fragment between these processes is determined through the image by evaporation of the break-up limit. We obtain, showing the parameters explicitly (instead of their value):

$$A_{lim} = \frac{11k - T_f^2}{11k} \cdot \frac{11 \cdot 27}{(11 \cdot 27 + T_f^2)} \cdot A_p \tag{7.17}$$

We use it as a sharp limit, without transition, between abrasion-evaporation regime and abrasion-multifragmentation-evaporation regime.

Let us calculate the contribution of the Fermi motion to the momentum dispersion. It is convenient to express A_{GH} (GH stands for Goldhaber) the mass of the prefragment just before evaporation as we will use as a variable in a formula similar to Goldhaber's.

For masses close to the projectile $(A_f \geq A_{lim})$, A_{GH} is the mass of the prefragment just after the abrasion step:

$$A_{GH} = \frac{kA_f + 27A_p}{(27 + k)} \tag{7.18}$$

The contribution to the momentum width from the Fermi motion in these events of abrasion-evaporation is simply given by:

$$\sigma^2_{p_\parallel Fermi} = \left(\frac{A_f}{A_{GH}}\right)^2 \cdot \frac{p_F^2}{5} \cdot \frac{A_{GH}(A_p - A_{GH})}{(A_p - 1)} \tag{7.19}$$

This has to be added quadratically with the contribution from recoil, in which one also takes A_{GH} as in equation 7.18.

If the observed final mass is below the limit, i.e. $A_f \leq A_{lim}$, the observed fragment was produced in an abrasion-multifragmentation-evaporation event; we will refer to "multi-fragmentation events", since abrasion and evaporation are always occuring. Let us define some relevant quantities to examine the effect of this combination of processes on the momentum dispersion. A_{GH}, the mass entering evaporation is this time the mass of the prefragment after abrasion and multifragmentation:

$$A_{GH} = \frac{11k}{11k - T_f^2} \cdot A_f \tag{7.20}$$

In order to make specific treatments for the multifragmentation process, for example to take into account the volume expansion between the prefragment after abrasion and the cracking system leading to multiple fragments, we need to assume the nature of the prefragment before multifragmentation. For an upper estimate, we will use the heaviest fragment that can enter multifragmentation. It corresponds to a precise number of nucleons abraded, resulting in an excitation energy sufficient to enter the break-up process. This maximum mass entering break-up is found on the figure 7.4 at the intersection of the lines E_1^* and E_2^*.

$$A_{bu} = \frac{27 \cdot 11}{27 \cdot 11 + T_f^2} A_p \tag{7.21}$$

The influence of the Fermi nature of the nucleons comes in two contributions in multifragmentation events: one contribution from the abrasion process (formation of a prefragment of mass A_{bu} out of a projectile A_p), and another contribution from the multifragmentation itself (formation of a product of mass A_{GH} out of an ensemble of A_{bu} nucleons). Furthermore, the volume expansion V_e subsequent to the excitation energy induced by abrasion is reducing the Fermi momentum and Fermi energy of the cracking system. It is defined as the ratio of the volume of the system at break-up over the volume in normal conditions: $V_e = V_{bu}/V_0$.

Thus, the total contribution of the Fermi motion in the kinematics of multifragmentation products, including the abrasion, is written:

$$\sigma^2_{p_\parallel Fermi} = \left(\frac{A_f}{A_{bu}}\right)^2 \cdot \frac{p_F^2}{5} \cdot \frac{A_{bu}(A_p - A_{bu})}{(A_p - 1)} + \left(\frac{A_f}{A_{GH}}\right)^2 \cdot \frac{p_{Fbu}^2}{5} \cdot \frac{A_{GH}(A_{bu} - A_{GH})}{(A_{bu} - 1)} \tag{7.22}$$

with p_{Fbu} the effective Fermi momentum at break-up, given by:

$$p_{Fbu} = p_F \cdot \left(\frac{V_0}{V_{bu}}\right)^{1/3} \tag{7.23}$$

Formula 7.22 is thus used exclusively to describe multifragmentation events, i.e. for a final fragment mass below A_{lim}. Let us repeat that formula 7.19 is used for larger observed masses.

The thermal motion inside the system at multifragmentation is also participating to the kinematics of the products, as was already said. Nuclear thermometry methods not based on the kinetics almost all agree on a thermalization of the cracking system near 5-6 MeV. We will use $T_f = 5$ MeV in the formula 7.4 proposed by Bauer to introduce a temperature in the Fermi gas.

Formula 7.22 can be kept in the same form, if we adapt the expression of p_{Fbu}, into an apparent Fermi momentum:

$$p_{Fbu} = p_F \cdot \left(\frac{V_0}{V_{bu}} \right)^{1/3} \cdot \frac{5\pi^2}{12} \left(\frac{T_{bu}}{E_{Fbu}^2} \right) \tag{7.24}$$

where

$$E_{Fbu} = E_F \cdot \left(\frac{V_0}{V_{bu}} \right)^{2/3} \tag{7.25}$$

Coulomb expansion

We evoked the expansion due to Coulomb forces, among the processes that should be implemented in a complete model. Let us reconsider equation 7.5. Many variables are subject to fluctuations from a reaction to another, but through simple assumptions, one can simplify this equation. Isospin thermometer experiments [SBC+93, SRBE02] have shown that the nuclear composition of prefragments just before the sequential evaporation steps is compatible with a scenario in which the prefragment keeps "in memory" the ratio Z_p/A_p of the projectile. Both processes, abrasion and multifragmentation, preserve this value. It means that both the mother nucleus and its considered daughter have the same proportion of neutrons and protons. We express then the atomic number of these two nuclei in the following form :

$$Z = A \cdot \frac{Z_p}{A_p} \tag{7.26}$$

where A, Z design the features of each considered part of the nuclear ensemble.

What's more, we do not know *a priori* the mass and charge of the source. As an upper estimate, still with Z/A fixed, one can take the heaviest fragment that can enter multifragmentation, of previously determined mass A_{bu} (see equation 7.21). This heaviest and most charged mother nucleus will generate the biggest electric field. This assumption should give us an upper estimate, but also allow us to check whether the magnitude of such an effect is compatible with observed spectra.

The distance r between the fragments at their formation is also crucial. We assume that the production of a fragment has a uniform probability inside the volume of the system. The variance of such a distribution of probability in one direction (in our case,

along the longitudinal axis) and within a small angular range[1] is then the one of a uniform distribution between an interval $[-r_{max};+r_{max}]$. The bounds of this interval correspond also to the maxima that the Coulomb contribution to the longitudinal momentum can take (which we name P_{Coul}). The Coulomb contribution to the variance of the spectra is then written:

$$\sigma^2_{p_{\parallel Coul}} = \frac{4}{12} \cdot \left(\frac{A_f}{A_{GH}}\right)^2 P^2_{Coul} \tag{7.27}$$

with the maximum estimate for the contribution taken as:

$$P^2_{Coul} = 2A_{GH} \cdot u \cdot \frac{A_{GH}A_{bu}Z_p^2 e^2}{A_p^2 R_{bu}^3} \cdot r_{max}^2 \cdot \left(1 - \frac{A_{GH}}{A_{bu}}\right)^2 \tag{7.28}$$

with $u = 931.5$ MeV$/c^2$ and $e^2 = 1.44$ MeV·fm. r_{max} is the maximum distance between the center of mass of the fragment and the one of the whole system, so it is the radius of the mother nucleus, reduced by the radius of the produced piece: $r_{max} = R_{bu} - R_{GH}$.

Our final analytical formula is the quadratic sum of the different contributions, the Fermi motion (from equation 7.19 for masses beyond A_{lim} or equation 7.22 for masses below A_{lim}), recoil induced by evaporation (formula 7.15), and Coulomb repulsion between multifragmentation products (equation 7.27, applied below A_{lim}). The momentum dispersion of final fragments is expressed as a function of their mass by:

$$\sigma^2_{p_{\parallel}} = \sigma^2_{p_{\parallel Fermi}} + \sigma^2_{p_{\parallel recoil}} + \sigma^2_{p_{\parallel Coul}} \tag{7.29}$$

The predictions given by our analytical model are compared in figure 7.9 with three different systems for which the data were available over the whole mass range: ^{197}Au+Au and ^{136}Xe+Pb at 1 A GeV, and ^{86}Kr+Be at 500 A MeV. The volume expansion at break-up was set to $V_{bu}/V_0 = 1.5$ and the freeze-out temperature $T_f = 5$ MeV. Although fission events in the reaction Au + Au were identified by their large recoil velocities and excluded from the analysis, there is a bump visible in the fission-fragment range. This might be a hint that the suppression of fission fragments is not complete.

The shape of the global prediction for $\sigma_{p_{\parallel}}$ of spectator fragments is in good accordance with the overall trend of the data available for this observable. For instance, the asymmetry of the formula, also present in the data, points out that specific assumptions made for intermediate and light fragments (multifragmentation, Coulomb repulsion between fragments) are pertinent. This mass region can not be treated the same way as heavier residues; the fact that more central and hence, more violent collisions, do not lead to the same evolution of the colliding system than peripheral collisions (producing heavy residues) is then sustained.

In figure 7.10, we compare the agreement with the xenon data of Morrissey's, Goldhaber's and our description (both analytical and from the simulation code). The asymmetry of the data would not have been predicted by Goldhaber's formula. Although

---

[1]The following formula is thus suited for the comparison with FRS data, measured with a strong kinematical cut on the emission angle. The corresponding formula for residues of all emission angles differs from this.
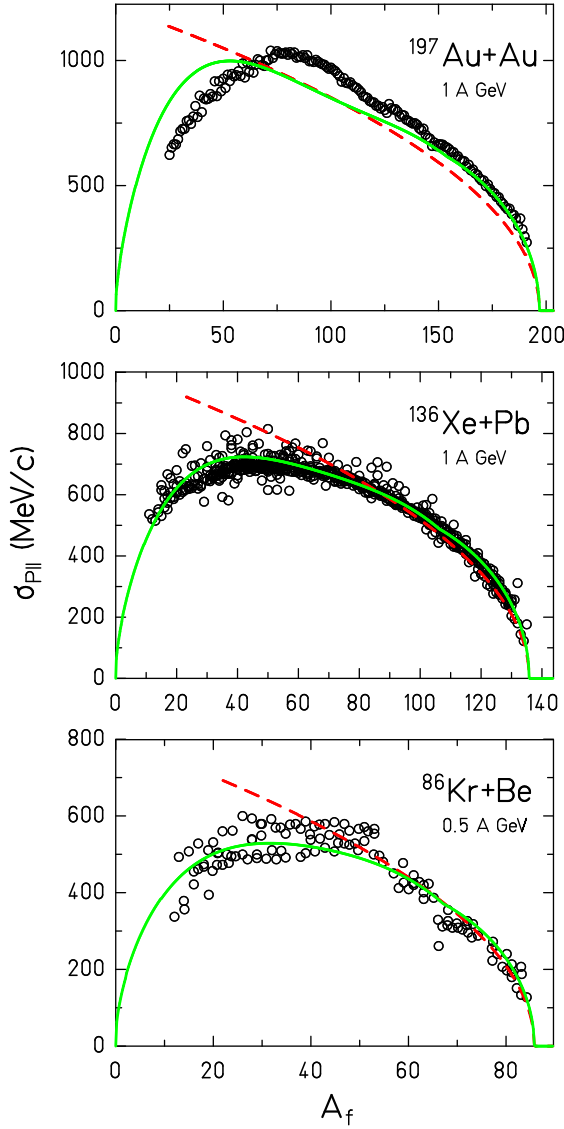
Figure 7.9: Analytical model in its full form as the square-root of equation 7.29 (plain line) and Morrissey's systematics (dashed line) compared to different data sets. The volume at break-up was taken to be $V_{bu} = 1.5V_0$, and the freeze-out temperature at 5 MeV.

its use for the final fragments is not appropriate, as was explained in the beginning of this chapter, it is not far from the data points; yet, our description leads to a better description.

The analytical formula and the simulation code offer a rather close prediction of this kinematical dispersion, which gives a relative validity to the specific assumptions that we made for the realization of the formula. The formula, which has less constraints than the code, who tries also to reproduce the cross-sections, gives a slightly better result, especially for light residues.

The degree of sophistication seems sufficient to reproduce the data. Some discrepancies
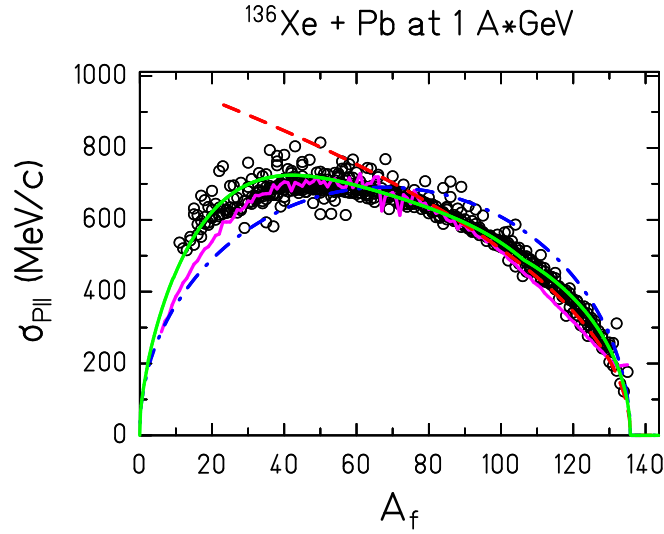
Figure 7.10: Comparison of the reproduction of xenon data with the analytical model (green line), ABRABLA (pink line) including the same principles on the kinematics, Morrissey's (red dashed line) and Goldhaber's (blue mixed line) formula.

subsist, and we can discuss these problems.

Several simplifications made in the formulation of the analytical expression tend to overestimate the width. In particular, we have incorporated multifragmentation effects with the largest widths, namely the one based on the Fermi momentum of the largest prefragment entering the break-up process.

Furthermore, to take into account the Coulomb repulsion between the fragments at break-up, we have taken the overestimating "option", supposing that the observed residue was always produced in the most extreme conditions: formation of the heaviest and most charged system entering multifragmentation. But small fragments coming from multi-fragmentation events are probably formed in more violent (i.e. more central) collisions, where abrasion produced a mother nucleus much lighter than what we would call a quasi-projectile. Our treatment of the Coulomb force at break-up is, again, giving an upper estimate of these effects.

Yet, the model is in general accordance with the data for very light fragments and no systematic over-prediction is observed. As said just above, in this region, our prediction could have been too large; this is not the case, neither for krypton nor for xenon data. In the case of gold data, the predicted dispersion is too high for the lightest fragments, and too low for fragments of mass about 90.

The combination of parameters that we took is sufficient to give satisfactory predictions. Let us remind these parameters. The excitation energy induced by the first step of the collision was taken from [SBC$^+$93], 27 MeV per removed nucleon. The mean energy reduction by evaporation of one nucleon is estimated to 15 MeV. The mean individual momentum of evaporated nucleons was estimated with considerations on the Coulomb barrier and the thermal motion in the source. The temperature of freeze-out in multifrag-

mentation (break-up) events is of the order of 5 MeV (see e.g. [NWH$^+$02]); the volume expansion at break-up is our last parameter, and adjusted to the data. Our aim is to learn about the mechanisms, especially at play in the multifragmentation process. We will therefore concentrate on the specific parameters of multifragmentation, and explore the sensitivity of the model to these parameters.

The kinematics of the multifragmentation products is not determined by the sole influence of a thermal motion and the Coulomb forces between the products. To confirm this conclusion, we tried to express the momentum dispersion using only these two ingredients. The thermal motion leads to a Boltzmann distribution of the velocities, with a temperature parameter. The result with a temperature of 5 MeV is shown in figure 7.11.
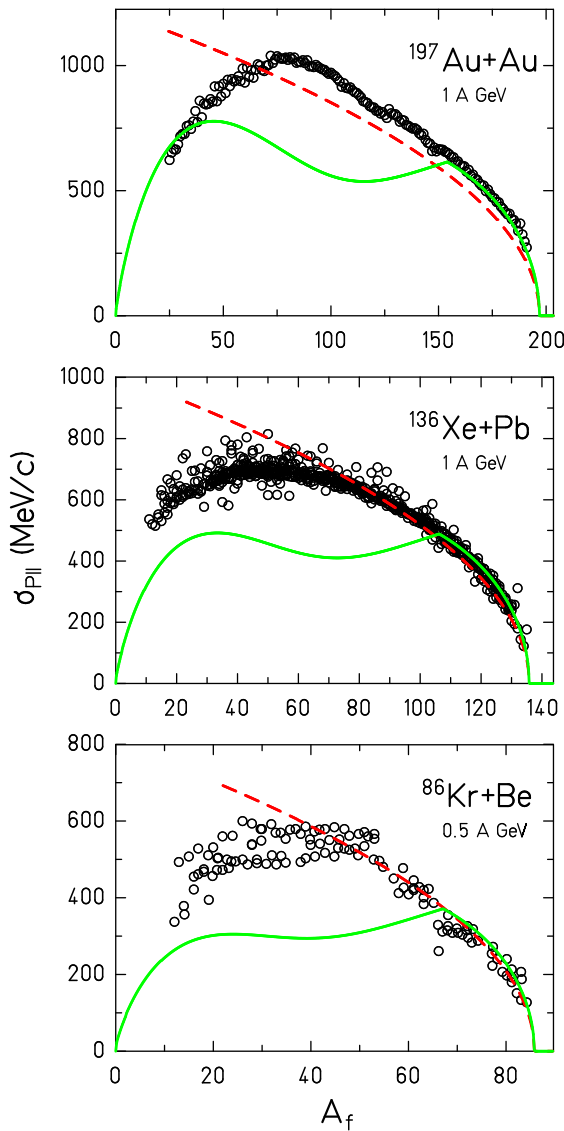
Figure 7.11: Model with kinematics of break-up products determined by Boltzmann statistics (temperature of 5 MeV) and the Coulomb interaction (plain line), compared to Morrissey systematics (dashed line) and to different data sets.

These predictions are not realistic and underestimate largely the momentum dispersion, confirming the importance of the Fermi motion to explain the width of the longitudinal momentum distributions.

The other extreme would be to neglect any thermal motion in the description of the momentum dispersion in multifragmentation, i.e. disregard the expression of p_{Fbu} given in equation 7.24. With picture 7.12, we understand that the contribution of the thermal
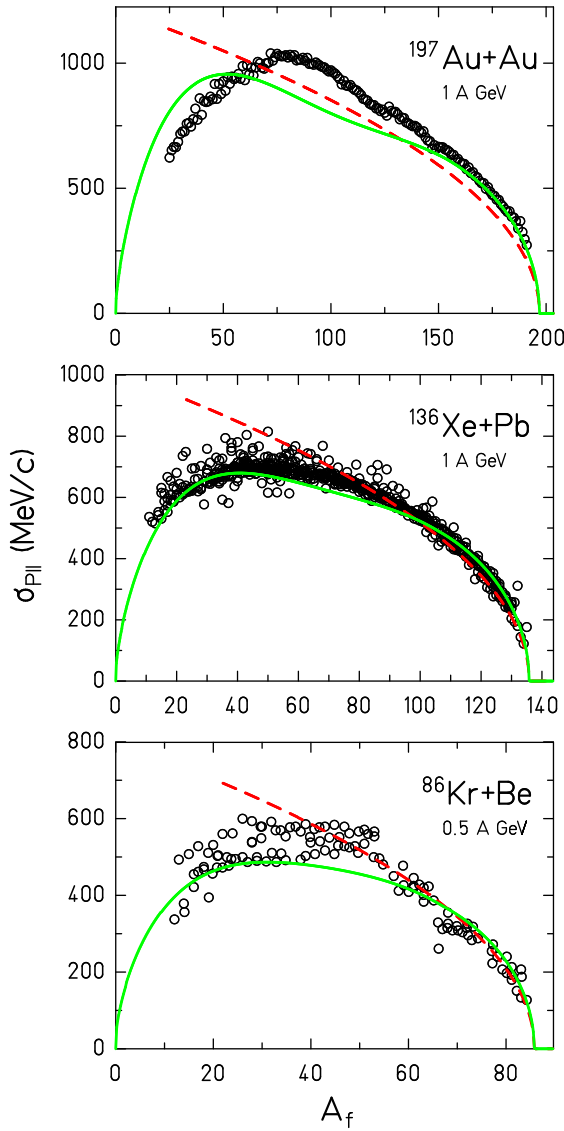
Figure 7.12: Model without any thermal motion entering the kinematics of break-up products (plain line), compared to Morrissey systematics (dashed line), and to different data sets.

motion to the kinematics of break-up products is not a great part of the total dispersion. Yet, without this contribution, the model systematically underestimates $\sigma_{p_\parallel}$. This is an indication that the system entering multifragmentation has indeed time to thermalize.

These were very fundamental options on the description of the multifragmentation process, and our model in these different configurations helps us to spot the essential features of multifragmentation. Fermi motion plays a major role, both in the abrasion and in the multifragmentation. Furthermore, the data are compatible with a quick thermalization of the cracking system, that reflects on the kinematics of the multifragmentation products.

Beyond these very important determinations of the reaction mechanisms at play in multifragmentation, we can try to estimate the dependence of our model on the parameters of these processes. One can make a variation on the freeze-out temperature at break-up, or one can modify the assumed volume expansion of the system. In figure 7.13, predictions of the full model with temperatures of 4 and 7 MeV are drawn. 7 MeV of freeze-out temperature leads to a clear underestimation of $\sigma_{p_\parallel}$ in the case of xenon and gold; the discrepancy is less pronounced for krypton. A freeze-out temperature of 4 MeV seems to reproduce better the gold case. This is in accordance with the dependence of the freeze-out temperature on the mass of the system, as is generally accepted (see for example [NWH$^+$02]).

In figure 7.14, attempts with break-up volumes of 1 and 3 times the normal volume V_0 are represented. The predictions without volume expansion are surprisingly well in accordance with the data. One can say that $\sigma_{p_\parallel}$ is slightly overestimated for multifragmentation products in the xenon case, but this is acceptable for the krypton data. For the gold data, the prediction fits even better than our very first presentation of the model with $V_{bu} = 3V_0$ in figure 7.9. This was not expected and is not well understood: one may expect that if the freeze-out temperature is lower, the volume expansion should be larger. This does not seem to be the case.

The right side of the figure 7.14 shows the model predictions with more dilution of the system: $V_{bu} = 3V_0$. For krypton and xenon, the accordance is acceptable, but the gold data are not reproduced in the region of multifragmentation. Near half the mass of the projectile, the model underestimates $\sigma_{p_\parallel}$, while it is largely overestimated for the lightest fragments represented.

It is important to note that our model does not consider the nature of the target nucleus. Even if the processes assumed to play a major role and the ideas used to develop the analytical description are not fully justified for all kinds of target, the agreement with the data is quite satisfactory. This demonstrates that the approximations made when developing the analytical approach were not crucial. Our formula obviously gives a good estimate of the kinematics of projectile-like fragments in the 1 GeV domain, which is the range of energy concerning the mentioned applications.
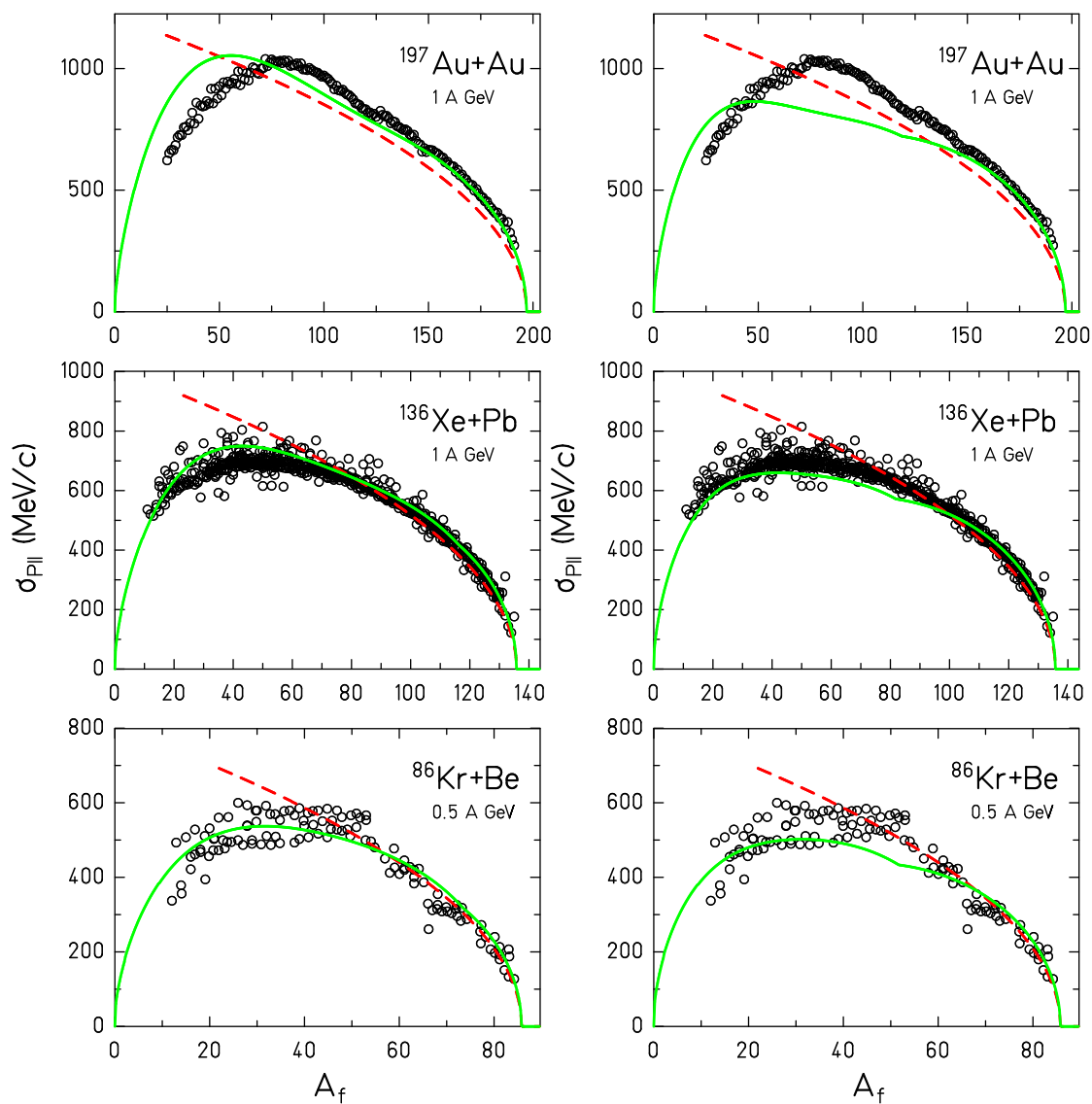
Figure 7.13: Full model with different freeze-out temperatures at break-up (plain line), compared to Morrissey systematics (dashed line), and to different data sets. On the left side, we took $T_f = 4$ MeV; on the right side, $T_f = 7$ MeV.
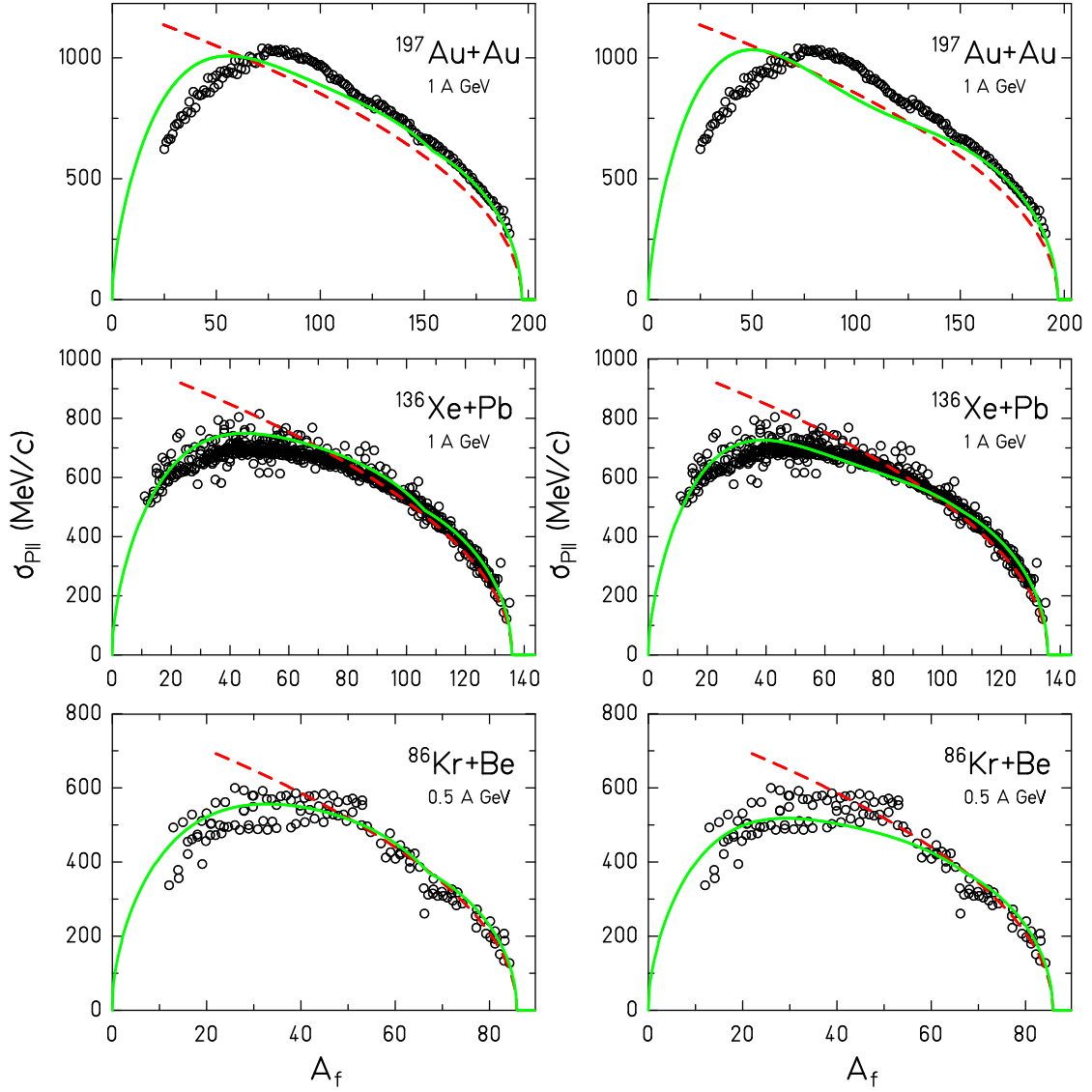
Figure 7.14: Full model with different volumes at break-up (plain line), compared to Morrissey systematics (dashed line), and to different data sets. The left side corresponds to the break-up without volume expansion, i.e. $V_{bu} = V_0$. On the right side, $V_{bu} = 3V_0$.

Summary

The Fragment Separator has proven to be a very powerful tool to study the reaction mechanisms at play in heavy-ion collisions at energies of the order of 1 GeV per nucleon. The small acceptance, limited to 15 mrad around the beam trajectory, acts as a kinematical cut on the velocity spectra. This inevitable angular selection strongly limits the transmission of light produced fragments, but it allows us to see deviations from a simple Gaussian shape in the longitudinal velocity spectra that would not be seen in a large-acceptance set-up without angular information.

The shapes of the longitudinal velocity spectra were the starting point of a discussion on the possible reaction mechanisms at play to produce the observed spectra. Heavy fragments populate Gaussian velocity spectra in space, and they do not reveal much information on the reaction mechanisms. Light fragments seem to have two main origins. Events where abrasion is followed by an asymmetric binary decay can populate a shell in velocity space, that translates through the acceptance of the FRS into broad asymmetric shapes in longitudinal velocity. Events where abrasion led to higher excitation energy, i.e. with a lower impact parameter, enter subsequently the multifragmentation process. Products of this break-up populate a Gaussian distribution in longitudinal velocity, similarly to heavier fragments.

This knowledge is of great importance. It is indeed crucial to understand that the light fragments observed in heavy-ion collisions come from various sources.

Experiments done at the FRS allow to reconstruct production cross-sections and velocity distributions of spectator fragments over a wide mass range, without any low-energy threshold. The cross-sections allowed us to establish the correlation for heavy fragments between the observed mass and the impact parameter of the collision, using the Glauber theory to describe the interaction. This information on the impact parameter for heavy fragments, i.e. peripheral collisions, is precious. The combination of this correlation with the other observable available in FRS experiments, the longitudinal velocity, made possible the presentation of the data on longitudinal velocities in a new aspect. Indeed, we could finally present the mean longitudinal velocity of observed fragments as a function of the impact parameter. This is interesting, because it allows for comparisons with models (ISABEL, QMD), independently from the treatment of the de-excitation of the prefragment produced in abrasion. The knowledge on the nucleon-nucleon cross-section could not be extracted, and would need further investigations with theoretical models. The complexity of the correlation of this cross-section with our observables and the long computation times of dynamical codes makes the achievement of this promising study

beyond the scope of the thesis. Nevertheless, it opened a new experimental approach to the in-medium nucleon-nucleon cross-section that should be exploited in the future.

We developed a new model to explain the variations of the standard deviation of longitudinal momentum spectra over the whole mass range of observed fragments. This model relies on general ideas on the reaction mechanisms and helps, by confrontation with the data, drawing a general picture of the production mechanisms and the kinematics of fragmentation residues. The ingredients of this new model were included in the simulation code ABRABLA, but were also compiled into an analytical formula, convenient for technical applications. The fundamental profit from this investigation is a greater knowledge on the influence of the reaction mechanisms on the kinematics of fragments observed in heavy-ion collisions at relativistic energies. The major role of the Fermi nature of the nucleons and the related motion inside the projectile, but also inside the mother nucleus of multifragmentation events, was demonstrated. The description of the system at break-up is a delicate matter that is subject to several models, with their specific assumptions on the dynamics of the process, and on the kinematics of the products. Our work indicates the following. After abrasion, when the induced excitation energy is beyond a critical temperature, the prefragment enters into multifragmentation. The excitation energy results in a volume expansion of the system. In addition to influence of the Fermi motion, the kinematics of the products originating from this expanded source are compatible with a thermal motion. This means that the fragment formation is a process slow enough to let the mother nucleus (or source) reach thermal equilibrium. The temperature parameter, corresponding to the freeze-out temperature at break-up, has been independently deduced by thermometry methods; its value of about 5 MeV is in accordance with the data, if we use the description of this contribution on the kinematics by Bauer [Bau95]. The volume expansion of the source plays a role, but the quantification of this expansion is delicate; the strong interplay between the parameters and the relatively low dependence of the prediction on the expansion makes its precise determination difficult. Yet, it seems that the value of $V_{bu} = 3V_0$ often suggested from the comparison of ALADiN data with SMM calculations is slightly too large in the case of xenon.

Our investigation excluded two extreme scenarii: an instantaneous break-up with no thermalization would not be sufficient to explain the kinematical dispersion, neither would a purely thermalized system with a realistic temperature of the order of 5 MeV.

Within this thesis, a comprehensive overview on the physics content of high-precision velocity measurements for fully identified residues has been given over the whole impact-parameter range where bound matter of the projectile spectator survives. Progress has been achieved to enlighten the experimental aspects for extracting the relevant nuclear properties behind the observed phenomena. Special emphasis was put on the in-medium nucleon-nucleon cross section and on the dynamics of the simultaneous break-up of nuclear matter. The complementary character of this information to results from full-acceptance experiments has been stressed.

As a practical result for applications, the theoretical understanding of the emittance of secondary beams produced by projectile fragmentation has been condensed in an analytical closed expression.

Outlook

The perspectives of this field in the light of the developments made in this thesis require a short review on the knowledge from experiments with the FRS but also with large-acceptance set-ups, to be fully exposed. The fragment separator at GSI, which is part of the SIS18 complex, was the first instrument world-wide, designed to provide secondary beams of radioactive nuclei in the 1 A GeV regime up to the region of ^{238}U. When the fragment separator became operational, about 20 years ago, it was one of the first goals to explore the new possibilities for providing secondary beams of exotic nuclei. A series of experiments aimed to identify the projectile fragments in nuclear charge Z and mass number A, to separate them [MGV$^+$94] and to measure their production cross sections [dJSB$^+$98, JdJC$^+$98, WDD$^+$94, ABB$^+$04, SBA$^+$98, DCA$^+$98, BAB$^+$98, EBF$^+$99, RFK$^+$98, SFF$^+$02]. The information on the production cross sections was crucial for estimating the prospects to provide a great variety of secondary beams of exotic nuclei, reaching as near as possible to the drip lines in order to explore their properties and thus to improve our knowledge on the general characteristics of nuclear structure. Some experiments provided specific information on the kinematical properties of the fragmentation residues and thus gave a glance on the high resolution achievable and on the improved insight into the reaction dynamics.

During the last years, fragmentation reactions of heavy nuclei with hydrogen in the 1 A GeV regime gained great interest due to their importance for technical applications. These were the incineration of radioactive waste in accelerator-driven systems (HINDAS, EUROTRANS) and the production of exotic nuclei in a new-generation ISOL-based secondary-beam facility (EURISOL, EURISOL-DS).

In an experimental campaign of an international collaboration, the fragmentation of a series of projectiles over the whole mass range with hydrogen, and in some cases also with deuterium, has been studied systematically [RMA$^+$01, BAB$^+$02, EAB$^+$02, EWA$^+$01, TSC$^+$03, BAB$^+$06, RAB$^+$06, BAB$^+$03, PBC$^+$07, CBP$^+$06, VCBD$^+$07, FDAA$^+$05, ATGA$^+$06, NSB$^+$04, NSTG$^+$07].

In addition to the production cross sections, the kinematical properties of the reaction residues were determined, too, in all these experiments. In most cases, they only played the key role for distinguishing the production by fragmentation-evaporation and fragmentation-fission reactions. Even some indications for contributions by multifragmentation reactions have been deduced from the residue kinematics [NSB$^+$04], although the energy introduced in the system is rather at the limit, where the simultaneous break-up is expected to set in. Detailed information on the reaction process has been extracted

for heavy residues very close to the projectile [HGS$^+$93, RFK$^+$98]. Only very recently, the kinematics of the residues has become the central subject of dedicated experimental studies. A completely new phenomenon has been discovered in the kinematics of light residues produced in heavy-ion fragmentation reactions: the re-acceleration of projectile-spectator matter [REP$^+$03], which was interpreted as the response of the spectators to the participants blast [SDL01] and related to the momentum-dependent contribution to the nuclear mean field.

This thesis provides the first systematic view on the experimental information, which can be obtained with a high-resolution magnetic spectrometer, like the fragment separator, on the kinematical properties of the fragmentation residues over the whole mass range from a variety of projectiles between ^{86}Kr and ^{197}Au. With this material, it is possible to provide an outlook on the prospects on future studies of the properties of nuclear matter with high-resolution spectrometers. In particular, it is tempting to compare the kind of information, which is accessible by this new approach, with the one gathered with traditional methods and to explore the benefit of eventually combining the two approaches in a future experimental installation, e.g. in the FAIR facility at GSI.

The instrument, which has traditionally been used for studying the decay of projectile-spectator matter at SIS energies is the large dipole magnet ALADiN. The magnetic deflection serves mostly for preventing the charged particles from hitting the large-area neutron detector LAND. The identification of the reaction products is mostly achieved by measuring the energy loss in a multiply sampling ionization chamber. The set-up is characterized by a full acceptance for the projectile-like fragments, except the very heavy residues, which are emitted with angles very close to the primary beam. The main experimental information consists of the multiplicity distribution and the atomic numbers of the residues. Only protons cannot be detected. Mass resolution can only be obtained for the lightest residues. Velocities of the fragments are determined by a time-of-flight measurement on a distance of about 10 m. The time-of-flight resolution is limited, and the absolute calibration imposes some difficulties due to the walk of the constant-fraction discriminators. This information is complemented with the measured multiplicity of light charged particles from a target hodoscope, which serves to characterize the impact parameter.

The most prominent results from these experiments consist in deducing the caloric curve of nuclear matter [PMR$^+$95] and discovering the rise and fall of multifragmentation [SKW$^+$96].

At the first sight, the information obtained with the high-resolution magnetic spectrometer FRS appears to be very different.

- all reaction products are fully identified in Z and A

- the momentum of each reaction product is determined with high precision on an absolute scale.

- there is an important kinematical cut to the invariant cross section in 3 dimensions; only products with velocity vectors almost parallel to the beam direction are

registered.

- only one fragment per reaction can be measured

Let us present a review of the experimental results on the kinematics of projectile fragments obtained at the fragment separator. The pattern of the velocity distributions, either one-humped or double-humped, served to distinguish fragmentation-evaporation from fragmentation-fission reactions in the analysis of many previous experiments. Due to the complete identification of the residues in Z and A and the full acceptance for heavy residues, the impact parameter could be deduced with the help of Glauber calculations of the nuclear transparency for very peripheral collisions. In this way, the friction phenomenon in peripheral nucleus-nucleus collisions could be determined as a function of the impact parameter for the first time in the present work. With decreasing impact parameter, the violence of the collision grows, and the friction phenomenon is more and more compensated and finally exceeded by a re-acceleration phenomenon, which had been interpreted as the participant blast to the spectators [REP+03]. For the lightest residues, the longitudinal velocity distributions of nucleus-nucleus collision residues develop a double-humped structure. In this thesis it was proposed to interpret this distribution as the superposition of a double-humped distribution, governed by the strong Coulomb repulsion of a heavy remnant and a single-humped distribution, which reflects the superposition of many recoils of similar size. In contrast to the triple-humped structure appearing in proton-induced reactions [NSB+04, NSTG+07], the re-acceleration phenomenon, which appears in nucleus-nucleus collisions, leads to an almost perfect superposition of the forward peak of the double-humped structure and the single hump in this case. Thus the true structure is not directly distinguishable from analyzing the shape of the spectrum. However, the high intensity of the forward peak compared to the backward one reveals the contributions of the two components in this peak. The single-humped distribution of the lightest fragment is attributed to the multifragmentation process, and thus it provides valuable information on the kinematics of this reaction type. The data have a very high quality: First, the velocities are measured with high resolution. Secondly, the measurement does not have any low-energy threshold, from which measurements in normal kinematics generally suffer. The interpretation of these data in terms of the kinematics of the multifragmentation process is another important subject of this thesis.

At this stage, we would like to mention some features of using high-resolution spectrometers for studies on nuclear fragmentation, which turn out to provide some unexpected benefits. The first feature we mention in this context is the kinematical cut induced by the limited angular acceptance of the fragment separator. While, on the one hand, it prevents to register those reaction products that are emitted with large transversal momentum, which is certainly an undesired restriction, it provides, on the other hand, a rather precise information on the emission angle of the measured residues. This way, the experimental information on longitudinal velocity distributions is rather close to the invariant cross section in one dimension along the beam axis, which is a very interesting experimental information. It has been shown that the kinematical information from full-acceptance experiments without a good velocity resolution and a precise measurement of

the emission angle is not able to resolve the fine structures, which are clearly observed in the high-resolution data from the magnetic spectrometer and which contain such a rich experimental information. The next feature to stress is the distance between the forward and the backward component of the double-humped structure in the velocity distribution. This distance is directly related to the size of the heavy remnant that is the source of the strong Coulomb repulsion, which is responsible for the double-humped structure in the velocity distribution of the light fragment. In this way, indirect information on a second heavy but unobserved fragment is accessible from the measurement of only one light fragment. Finally, the mean velocities of the two components, the double-humped and the single-humped distributions, carry the information on the violence of the two reaction types responsible for their production. It seems that the quantitative calibration of this information in terms of impact parameter can only be deduced for the more peripheral collisions from this experiment alone, but the sensitivity is certainly given, also for the lightest residues produced in rather central collisions. Thus, the measurement of the mean velocity of a certain group of reaction products with a high-resolution magnetic spectrometer is, in principle, another suitable tool to provide the information on the mean impact parameter of this reaction group in addition to the well established signatures like Z_{bound} or the multiplicity of light charged particles.

One may imagine that the combination of a full-acceptance set-up with a high-resolution spectrometer in a unique experimental set-up would provide an important progress. Essential experimental information from both sources with different characteristics could be combined on an event-by-event basis and provide a substantial progress in the experimental study of the properties of nuclear matter. It is hoped that a set-up of such kind will be available at the future FAIR facility of GSI.

Appendix

Moments of the velocity distributions

Let us remind that these quantities are obtained through their mathematical expression for the raw longitudinal velocity distributions, obtained within the acceptance of 15 mrad of the Fragment Separator. These data are from the experiment ^{136}Xe+Pb at 1 AGeV. Due to the slight enhancement of fragments emitted in forward direction compared to backward-emitted fragments by the kinematical cut of the FRS, the mean velocity values of the full distribution are slightly larger than the directly measured values given here in the cases of the lighter masses, where the angular transmission is well below 100%. However, this effect is very small and is comparable with the uncertainty of the data points [Ric04]. The effect of the limited angular acceptance on the higher moments is expected to be more important in the lower mass range in those cases, where the shape of the distribution appreciably differs from a Gaussian and where the angular transmission is low.

Z	N	A	mean (cm/ns)	σ (cm/ns)	skewness
light residues					
3	3	6	-3.29E-02	1.82E+00	-2.85E-01
3	4	7	-2.61E-01	1.81E+00	-1.08E-01
3	5	8	-9.92E-02	1.68E+00	-4.26E-01
4	3	7	9.75E-02	1.79E+00	-1.02E-01
4	5	9	-1.47E-01	1.56E+00	-2.08E-01
4	6	10	-7.04E-02	1.56E+00	-2.74E-01
4	7	11	-2.11E-01	1.41E+00	-5.11E-01
5	5	10	8.92E-02	1.61E+00	-3.56E-01
5	6	11	-6.50E-02	1.41E+00	-3.33E-01
5	7	12	-1.38E-01	1.39E+00	-2.47E-01
5	8	13	-4.55E-02	1.35E+00	-4.08E-01
5	9	14	-3.68E-01	1.33E+00	-6.72E-01
6	5	11	9.47E-02	1.62E+00	-1.40E-01
6	6	12	2.38E-02	1.36E+00	-3.78E-01
6	7	13	-6.80E-03	1.26E+00	-3.96E-01
6	8	14	-8.43E-02	1.20E+00	-3.66E-01
6	9	15	-1.00E-01	1.27E+00	-3.68E-01

Z	N	A	mean (cm/ns)	σ (cm/ns)	skewness
6	10	16	-8.09E-02	1.22E+00	-4.80E-01
6	11	17	-3.07E-01	1.21E+00	-9.61E-01
7	7	14	4.54E-02	1.29E+00	-3.61E-01
7	8	15	3.52E-02	1.15E+00	-4.54E-01
7	9	16	-2.39E-02	1.14E+00	-3.91E-01
7	10	17	-8.47E-02	1.13E+00	-3.67E-01
7	11	18	-5.76E-02	1.16E+00	-4.87E-01
7	12	19	-1.11E-01	1.15E+00	-7.32E-01
7	13	20	-4.67E-01	1.24E+00	-1.15E+00
8	8	16	4.11E-02	1.16E+00	-3.71E-01
8	9	17	5.83E-02	1.08E+00	-4.82E-01
8	10	18	-1.23E-02	1.05E+00	-4.19E-01
8	11	19	-4.48E-02	1.01E+00	-4.73E-01
8	12	20	-8.53E-02	1.07E+00	-4.51E-01
8	13	21	-2.28E-01	1.12E+00	-3.27E-01
8	14	22	-1.94E-01	1.17E+00	-9.43E-01
9	9	18	1.65E-01	1.17E+00	-2.63E-01
9	10	19	7.13E-02	1.04E+00	-5.11E-01
9	11	20	2.30E-02	9.92E-01	-4.95E-01
9	12	21	-1.71E-02	9.73E-01	-5.13E-01
9	13	22	-6.40E-02	9.67E-01	-5.34E-01
9	14	23	-9.23E-02	1.03E+00	-5.83E-01
9	15	24	-2.29E-01	1.19E+00	-9.76E-01
9	16	25	-4.39E-01	1.25E+00	-7.96E-01
9	17	26	-2.50E-01	6.60E-01	5.82E-02
10	10	20	7.93E-02	1.05E+00	-2.80E-01
10	11	21	7.07E-02	9.68E-01	-5.31E-01
10	12	22	2.68E-02	9.20E-01	-5.31E-01
10	13	23	-6.65E-03	9.16E-01	-5.12E-01
10	14	24	-4.33E-02	8.81E-01	-6.49E-01
10	15	25	-1.91E-01	1.02E+00	-9.10E-01
10	16	26	-1.80E-01	1.07E+00	-7.58E-01
10	17	27	1.34E-01	7.50E-01	-1.41E-01
10	19	29	-6.32E-02	4.86E-01	-8.01E-01
11	11	22	1.25E-01	1.07E+00	7.08E-02
11	12	23	5.72E-02	9.12E-01	-5.32E-01
11	13	24	3.71E-02	8.75E-01	-5.73E-01
11	14	25	1.09E-03	8.51E-01	-5.34E-01
11	15	26	-1.29E-02	8.50E-01	-6.55E-01
11	16	27	-8.82E-02	8.46E-01	-7.56E-01
11	17	28	-1.98E-01	1.05E+00	-9.52E-01
11	18	29	-1.96E-01	1.03E+00	-6.84E-01

Z	N	A	mean (cm/ns)	σ (cm/ns)	skewness
11	19	30	6.28E-02	7.33E-01	-2.28E-01
11	20	31	-1.53E-01	7.25E-01	-2.44E-01
12	12	24	7.28E-02	9.43E-01	-1.79E-01
12	13	25	5.24E-02	8.53E-01	-5.18E-01
12	14	26	2.84E-02	8.16E-01	-5.48E-01
12	15	27	-1.22E-02	8.08E-01	-5.63E-01
12	16	28	-1.84E-02	8.19E-01	-5.83E-01
12	17	29	-6.66E-02	8.17E-01	-1.20E+00
12	18	30	-1.74E-01	8.78E-01	-7.84E-01
12	20	32	-2.63E-01	1.04E+00	-9.94E-01
12	21	33	2.82E-02	5.45E-01	2.20E-01
12	22	34	5.57E-05	3.55E-01	-3.64E-01
13	13	26	1.43E-01	9.62E-01	-3.14E-02
13	14	27	5.02E-02	7.99E-01	-5.07E-01
13	15	28	3.40E-02	7.64E-01	-5.66E-01
13	16	29	3.47E-03	7.52E-01	-5.53E-01
13	17	30	-1.68E-02	7.55E-01	-5.18E-01
13	18	31	-2.81E-02	7.46E-01	-6.88E-01
13	19	32	-1.49E-01	8.10E-01	-8.67E-01
13	20	33	-2.27E-01	9.29E-01	-1.14E+00
13	21	34	-7.68E-01	1.52E+00	-8.75E-01
13	22	35	-5.15E-01	1.43E+00	-1.24E+00
13	23	36	-5.20E-02	7.77E-01	-5.46E-02
14	14	28	7.15E-02	8.25E-01	-2.01E-01
14	15	29	4.68E-02	7.67E-01	-5.81E-01
14	16	30	3.86E-02	7.26E-01	-5.97E-01
14	17	31	2.00E-03	7.10E-01	-5.72E-01
14	18	32	-1.24E-02	7.05E-01	-5.74E-01
14	19	33	-1.88E-02	7.47E-01	-7.55E-01
14	20	34	-5.62E-02	6.87E-01	-7.90E-01
14	21	35	-2.55E-01	7.89E-01	-1.36E+00
14	22	36	-7.22E-01	1.47E+00	-1.41E+00
14	23	37	2.90E-02	5.41E-01	-2.74E-01
14	25	39	-1.84E-01	7.48E-01	1.57E-01
15	16	31	3.97E-02	7.30E-01	-4.95E-01
15	17	32	2.84E-02	6.99E-01	-6.10E-01
15	18	33	8.20E-03	6.85E-01	-5.63E-01
15	19	34	-3.93E-02	6.80E-01	-6.96E-01
15	20	35	-4.70E-02	7.00E-01	-7.02E-01
15	21	36	-7.30E-02	7.33E-01	-1.07E+00
15	22	37	-1.95E-01	7.17E-01	-1.10E+00
15	23	38	-4.72E-02	7.82E-01	-1.52E+00

Z	N	A	mean (cm/ns)	σ (cm/ns)	skewness
15	24	39	-3.21E-01	1.19E+00	-1.47E+00
15	25	40	-3.45E-01	1.14E+00	-9.15E-01
15	26	41	2.55E-01	4.33E-01	8.80E-01
15	27	42	1.75E-01	0.00E+00	0.00E+00
16	16	32	1.37E-01	8.88E-01	7.41E-01
16	17	33	4.65E-02	6.92E-01	-4.63E-01
16	18	34	3.33E-02	6.58E-01	-6.28E-01
16	19	35	2.36E-02	6.43E-01	-6.43E-01
16	20	36	-1.24E-02	6.45E-01	-6.45E-01
16	21	37	-4.01E-02	6.62E-01	-8.40E-01
16	22	38	-5.27E-02	7.01E-01	-9.65E-01
16	23	39	-1.47E-01	7.41E-01	-1.48E+00
16	24	40	-2.61E-01	9.23E-01	-2.04E+00
17	18	35	3.93E-02	6.72E-01	-1.79E-01
17	19	36	2.33E-02	6.29E-01	-6.00E-01
17	20	37	8.09E-04	6.15E-01	-6.35E-01
17	21	38	-2.36E-02	6.20E-01	-7.48E-01
17	22	39	-4.80E-02	6.28E-01	-7.83E-01
17	23	40	-5.34E-02	6.60E-01	-8.17E-01
17	24	41	-5.71E-02	6.54E-01	-1.34E+00
17	25	42	-2.82E-01	9.03E-01	-1.98E+00
18	18	36	1.87E-01	8.56E-01	1.34E+00
18	19	37	4.61E-02	6.24E-01	-1.44E-01
18	20	38	2.02E-02	6.00E-01	-4.72E-01
18	21	39	1.03E-02	5.91E-01	-5.81E-01
18	22	40	-3.15E-02	5.86E-01	-7.16E-01
18	23	41	-5.66E-02	5.92E-01	-7.58E-01
18	24	42	-6.64E-02	6.32E-01	-1.04E+00
18	25	43	-1.05E-01	6.98E-01	-1.39E+00
18	26	44	-3.11E-01	8.75E-01	-1.77E+00
19	20	39	3.86E-02	6.02E-01	1.12E-01
19	21	40	1.59E-02	5.57E-01	-4.27E-01
19	22	41	2.64E-03	5.60E-01	-5.05E-01
19	23	42	-2.69E-02	5.58E-01	-5.95E-01
19	24	43	-3.71E-02	5.68E-01	-7.84E-01
19	25	44	-8.93E-02	6.10E-01	-1.01E+00
19	26	45	-7.49E-02	6.59E-01	-1.27E+00
19	27	46	-1.52E-01	8.17E-01	-1.85E+00
19	28	47	-2.08E-01	7.17E-01	-2.30E+00
20	21	41	4.41E-02	5.76E-01	2.84E-01
20	22	42	1.20E-02	5.40E-01	-1.25E-01
20	23	43	-8.49E-03	5.20E-01	-3.13E-01

Z	N	A	mean (cm/ns)	σ (cm/ns)	skewness
20	24	44	-2.87E-02	5.23E-01	-4.40E-01
20	25	45	-4.50E-02	5.38E-01	-6.12E-01
20	26	46	-9.30E-02	5.73E-01	-1.09E+00
20	27	47	-1.82E-01	7.19E-01	-1.39E+00
21	22	43	6.60E-02	6.01E-01	9.57E-01
21	23	44	1.09E-02	5.13E-01	-1.02E-01
21	24	45	-4.81E-03	4.98E-01	-2.07E-01
21	25	46	-1.02E-02	4.92E-01	-3.12E-01
21	26	47	-5.39E-02	4.95E-01	-5.27E-01
21	27	48	-8.81E-02	5.47E-01	-9.87E-01
21	28	49	-1.59E-01	6.58E-01	-1.40E+00
22	23	45	4.72E-02	5.49E-01	6.90E-01
22	24	46	4.88E-03	4.98E-01	1.40E-01
22	25	47	-8.91E-04	4.77E-01	-6.34E-02
22	26	48	-2.60E-02	4.68E-01	-2.19E-01
22	27	49	-5.03E-02	4.66E-01	-3.32E-01
22	28	50	-8.13E-02	5.09E-01	-9.27E-01
22	29	51	-1.90E-01	6.52E-01	-1.52E+00
23	24	47	1.09E-01	6.07E-01	2.11E+00
23	25	48	2.72E-02	4.67E-01	4.29E-01
23	26	49	-1.76E-03	4.55E-01	-1.32E-01
23	27	50	-1.74E-02	4.50E-01	-2.28E-01
23	28	51	-4.88E-02	4.50E-01	-3.39E-01
23	29	52	-8.87E-02	4.80E-01	-6.72E-01
23	30	53	-1.36E-01	5.51E-01	-1.45E+00
23	31	54	-2.87E-01	7.57E-01	-1.49E+00
24	25	49	1.93E-01	6.16E-01	2.51E+00
24	26	50	5.57E-02	4.16E-01	3.67E-01
24	27	51	1.85E-02	4.17E-01	4.11E-02
24	28	52	-2.62E-02	4.25E-01	-1.46E-01
24	29	53	-4.96E-02	4.29E-01	-3.53E-01
24	30	54	-6.87E-02	4.58E-01	-6.02E-01
24	31	55	-1.02E-01	5.22E-01	-1.03E+00
24	32	56	-1.99E-01	6.42E-01	-1.84E+00
25	28	53	9.55E-02	3.80E-01	2.55E-01
25	29	54	2.41E-02	3.93E-01	1.17E-02
25	30	55	-3.80E-02	4.04E-01	-2.18E-01
25	31	56	-6.52E-02	4.19E-01	-3.99E-01
25	32	57	-9.68E-02	4.60E-01	-9.96E-01
25	33	58	-1.79E-01	5.45E-01	-1.39E+00
25	34	59	-3.04E-01	7.89E-01	-1.69E+00

Z	N	A	mean (cm/ns)	σ (cm/ns)	skewness
heavy residues					
15	14	29	9.36E-02	1.06E+00	-5.54E-02
15	15	30	1.00E-02	8.27E-01	-4.88E-01
15	16	31	2.11E-03	6.99E-01	-3.67E-01
15	17	32	-8.55E-03	6.86E-01	-3.78E-01
15	18	33	-1.39E-04	6.70E-01	-3.48E-01
15	19	34	-4.47E-03	6.67E-01	-3.21E-01
15	20	35	5.48E-05	6.42E-01	-3.89E-01
15	21	36	1.86E-02	6.36E-01	-4.73E-01
15	22	37	-2.20E-01	6.34E-01	-3.14E-01
15	23	38	-1.44E-01	7.35E-01	-2.03E-01
16	15	31	1.17E-01	1.09E+00	-1.05E-01
16	16	32	2.18E-02	7.27E-01	-5.00E-01
16	17	33	-2.92E-03	6.77E-01	-4.60E-01
16	18	34	-1.59E-04	6.48E-01	-3.98E-01
16	19	35	-6.58E-03	6.41E-01	-3.51E-01
16	20	36	-7.14E-04	6.23E-01	-3.54E-01
16	21	37	1.10E-03	6.24E-01	-4.04E-01
16	22	38	1.97E-02	6.38E-01	-4.71E-01
16	23	39	-7.21E-02	5.69E-01	-4.96E-01
16	24	40	-1.98E-01	6.12E-01	1.88E-01
16	25	41	-1.31E-01	8.17E-01	-8.26E-01
16	26	42	8.63E-02	3.14E-01	-2.10E-02
17	17	34	-1.33E-02	7.89E-01	-5.83E-01
17	18	35	5.38E-04	6.49E-01	-4.37E-01
17	19	36	-1.45E-02	6.28E-01	-4.28E-01
17	20	37	-1.93E-02	6.14E-01	-3.54E-01
17	21	38	-1.84E-02	5.99E-01	-4.01E-01
17	22	39	-2.31E-02	5.89E-01	-3.62E-01
17	23	40	-1.06E-02	5.90E-01	-5.57E-01
17	24	41	-2.45E-02	5.59E-01	-3.13E-01
17	25	42	-1.53E-01	5.26E-01	-2.09E-01
17	26	43	-1.19E-02	6.10E-01	-3.46E-01
17	27	44	-1.54E-01	7.78E-01	-8.48E-01
18	18	36	1.60E-02	7.27E-01	-3.21E-01
18	19	37	-3.56E-02	6.28E-01	-4.95E-01
18	20	38	-2.46E-02	5.98E-01	-4.20E-01
18	21	39	-3.43E-02	5.86E-01	-3.58E-01
18	22	40	-3.66E-02	5.69E-01	-3.72E-01
18	23	41	-3.19E-02	5.58E-01	-3.41E-01
18	24	42	-3.47E-02	5.58E-01	-3.55E-01
18	25	43	-3.35E-02	5.42E-01	-5.83E-01

Z	N	A	mean (cm/ns)	σ (cm/ns)	skewness
18	26	44	-1.89E-01	5.85E-01	-1.26E+00
18	27	45	-1.66E-01	4.65E-01	1.37E-01
18	28	46	-2.79E-01	8.48E-01	-6.20E-01
18	29	47	5.98E-02	2.83E-01	-1.50E-01
19	19	38	3.75E-02	8.08E-01	-3.20E-02
19	20	39	-2.89E-02	5.98E-01	-4.64E-01
19	21	40	-3.13E-02	5.75E-01	-4.23E-01
19	22	41	-3.55E-02	5.58E-01	-3.51E-01
19	23	42	-2.96E-02	5.47E-01	-3.32E-01
19	24	43	-4.14E-02	5.32E-01	-3.58E-01
19	25	44	-4.73E-02	5.22E-01	-3.77E-01
19	26	45	-5.12E-02	5.40E-01	-4.64E-01
19	27	46	-7.39E-02	5.30E-01	-7.46E-01
19	28	47	-2.26E-01	5.23E-01	-8.11E-01
19	30	49	1.56E-01	3.73E-01	-1.16E-01
20	20	40	5.02E-02	7.01E-01	-7.69E-02
20	21	41	-3.14E-02	5.84E-01	-5.07E-01
20	22	42	-2.91E-02	5.53E-01	-4.04E-01
20	23	43	-3.27E-02	5.34E-01	-3.60E-01
20	24	44	-3.39E-02	5.23E-01	-3.11E-01
20	25	45	-4.13E-02	5.10E-01	-3.83E-01
20	26	46	-4.20E-02	5.16E-01	-3.92E-01
20	27	47	-2.53E-02	5.06E-01	-3.88E-01
20	28	48	-9.46E-02	4.79E-01	-7.31E-01
20	29	49	-2.01E-01	4.06E-01	-3.82E-01
20	30	50	-5.09E-01	8.61E-01	-3.02E-01
20	31	51	-2.81E-01	1.03E+00	-9.62E-01
20	32	52	1.89E-01	1.79E-01	1.15E+00
20	50	70	1.89E-01	1.79E-01	1.15E+00
21	21	42	1.38E-01	8.36E-01	2.30E-01
21	22	43	-2.93E-02	5.63E-01	-3.34E-01
21	23	44	-4.05E-02	5.27E-01	-4.13E-01
21	24	45	-4.47E-02	5.08E-01	-3.44E-01
21	25	46	-4.41E-02	4.99E-01	-2.85E-01
21	26	47	-4.01E-02	4.79E-01	-2.86E-01
21	27	48	-6.32E-02	4.82E-01	-4.04E-01
21	28	49	-5.89E-02	4.74E-01	-4.01E-01
21	29	50	-4.67E-02	4.69E-01	-2.52E-01
21	30	51	-7.81E-02	4.90E-01	-7.39E-01
21	31	52	-2.70E-01	3.78E-01	1.95E-01
21	33	54	1.92E-01	2.33E-01	7.12E-01
21	34	55	3.70E-02	2.31E-01	-3.43E-01

Z	N	A	mean (cm/ns)	σ (cm/ns)	skewness
22	22	44	1.25E-01	7.59E-01	5.75E-01
22	23	45	-4.72E-02	5.40E-01	-5.05E-01
22	24	46	-4.52E-02	5.03E-01	-4.15E-01
22	25	47	-5.42E-02	4.86E-01	-3.27E-01
22	26	48	-4.82E-02	4.70E-01	-2.67E-01
22	27	49	-4.77E-02	4.65E-01	-2.71E-01
22	28	50	-5.72E-02	4.57E-01	-2.94E-01
22	29	51	-6.29E-02	4.70E-01	-6.00E-01
22	30	52	-5.44E-02	4.62E-01	-5.14E-01
22	31	53	-8.76E-02	5.20E-01	-1.41E+00
22	32	54	-2.80E-01	4.07E-01	-4.48E-01
22	33	55	-1.74E-01	3.86E-01	-3.75E+00
22	34	56	1.10E-01	2.76E-01	6.34E-01
23	24	47	-3.90E-02	5.23E-01	-3.38E-01
23	25	48	-5.64E-02	4.84E-01	-4.52E-01
23	26	49	-5.65E-02	4.62E-01	-3.08E-01
23	27	50	-5.16E-02	4.52E-01	-2.47E-01
23	28	51	-5.47E-02	4.47E-01	-2.43E-01
23	29	52	-5.08E-02	4.40E-01	-3.69E-01
23	30	53	-5.64E-02	4.34E-01	-2.95E-01
23	31	54	-5.70E-02	4.46E-01	-3.62E-01
23	32	55	-5.52E-02	4.09E-01	-4.02E-01
23	33	56	-1.76E-01	3.71E-01	-3.89E-01
23	34	57	-2.08E-01	4.84E-01	-1.38E+00
23	35	58	-3.05E-01	6.25E-01	1.65E-01
23	37	60	1.76E-01	3.35E-01	-7.17E-01
24	25	49	-5.06E-02	5.29E-01	-1.77E-01
24	26	50	-6.94E-02	4.62E-01	-3.73E-01
24	27	51	-6.25E-02	4.50E-01	-3.20E-01
24	28	52	-6.37E-02	4.31E-01	-2.49E-01
24	29	53	-6.31E-02	4.29E-01	-2.60E-01
24	30	54	-6.23E-02	4.23E-01	-2.39E-01
24	31	55	-6.36E-02	4.20E-01	-3.58E-01
24	32	56	-6.14E-02	4.06E-01	-2.44E-01
24	33	57	-5.21E-02	4.21E-01	-5.03E-01
24	34	58	-6.73E-02	4.77E-01	-1.18E+00
24	35	59	-2.56E-01	3.31E-01	-1.03E+00
24	36	60	-2.68E-01	3.20E-01	9.66E-01
24	37	61	6.08E-02	2.40E-01	5.64E-01
25	26	51	-4.52E-02	5.42E-01	2.36E-01
25	27	52	-7.78E-02	4.47E-01	-3.65E-01
25	28	53	-7.50E-02	4.26E-01	-3.58E-01

Z	N	A	mean (cm/ns)	σ (cm/ns)	skewness
25	29	54	-7.30E-02	4.18E-01	-2.70E-01
25	30	55	-7.03E-02	4.14E-01	-2.26E-01
25	31	56	-6.76E-02	4.08E-01	-2.54E-01
25	32	57	-7.04E-02	4.05E-01	-2.88E-01
25	33	58	-8.27E-02	4.06E-01	-3.74E-01
25	34	59	-7.17E-02	3.99E-01	-3.82E-01
25	35	60	-6.35E-02	4.35E-01	-9.65E-01
25	36	61	-8.20E-02	3.56E-01	-5.79E-01
25	37	62	-2.50E-01	5.18E-01	-1.64E+00
25	39	64	-1.16E-01	2.76E-01	7.12E-01
26	27	53	-5.61E-02	4.92E-01	5.23E-02
26	28	54	-7.91E-02	4.35E-01	-2.81E-01
26	29	55	-8.74E-02	4.11E-01	-3.44E-01
26	30	56	-8.32E-02	3.97E-01	-3.05E-01
26	31	57	-8.35E-02	3.99E-01	-2.23E-01
26	32	58	-7.82E-02	3.94E-01	-2.97E-01
26	33	59	-8.32E-02	3.87E-01	-2.75E-01
26	34	60	-8.13E-02	3.84E-01	-3.21E-01
26	35	61	-7.75E-02	4.01E-01	-4.85E-01
26	36	62	-9.59E-02	3.76E-01	-2.26E-01
26	37	63	-6.93E-02	4.48E-01	-2.03E-01
26	38	64	1.49E-02	3.25E-01	-9.97E-01
26	39	65	-8.86E-02	2.14E-01	1.06E+00
26	40	66	1.19E-01	1.62E-01	1.28E+00
26	41	67	-2.57E-01	2.76E-01	1.14E+00
27	28	55	-4.34E-02	5.29E-01	2.37E-01
27	29	56	-8.33E-02	4.23E-01	-3.24E-01
27	30	57	-9.22E-02	3.98E-01	-3.80E-01
27	31	58	-8.69E-02	3.87E-01	-2.91E-01
27	32	59	-8.47E-02	3.77E-01	-2.20E-01
27	33	60	-8.27E-02	3.79E-01	-2.56E-01
27	34	61	-8.41E-02	3.70E-01	-2.70E-01
27	35	62	-8.40E-02	3.75E-01	-3.37E-01
27	36	63	-9.77E-02	3.80E-01	-6.95E-01
27	37	64	-6.99E-02	4.00E-01	-5.71E-01
27	38	65	-6.99E-02	4.10E-01	-6.24E-01
27	39	66	-1.23E-01	3.33E-01	-8.45E-01
27	40	67	-4.58E-03	2.94E-01	-1.58E+00
27	41	68	-1.84E-01	6.22E-01	-5.69E-01
27	42	69	-2.54E-01	2.02E-01	2.51E+00
28	29	57	-5.75E-03	5.58E-01	6.34E-01
28	30	58	-8.31E-02	4.06E-01	-7.01E-01

Z	N	A	mean (cm/ns)	σ (cm/ns)	skewness
28	31	59	-8.68E-02	3.83E-01	-4.51E-01
28	32	60	-8.47E-02	3.72E-01	-3.32E-01
28	33	61	-8.94E-02	3.66E-01	-2.42E-01
28	34	62	-8.30E-02	3.61E-01	-2.04E-01
28	35	63	-7.80E-02	3.57E-01	-2.58E-01
28	36	64	-8.44E-02	3.54E-01	-2.38E-01
28	37	65	-9.43E-02	3.64E-01	-6.28E-01
28	38	66	-8.51E-02	3.87E-01	-7.29E-01
28	39	67	-7.54E-02	3.43E-01	-4.37E-01
28	40	68	-1.04E-01	3.02E-01	-6.55E-01
28	41	69	-5.01E-03	3.66E-01	-8.29E-01
28	42	70	-1.92E-01	3.62E-01	1.48E+00
28	44	72	1.05E-01	4.00E-02	8.44E-01
29	30	59	1.37E-01	7.65E-01	1.25E+00
29	31	60	-7.44E-02	4.46E-01	2.29E-01
29	32	61	-9.92E-02	3.76E-01	-4.77E-01
29	33	62	-9.28E-02	3.62E-01	-3.22E-01
29	34	63	-9.24E-02	3.48E-01	-2.59E-01
29	35	64	-9.12E-02	3.48E-01	-2.35E-01
29	36	65	-8.45E-02	3.48E-01	-3.16E-01
29	37	66	-8.85E-02	3.43E-01	-2.91E-01
29	38	67	-9.15E-02	3.43E-01	-4.27E-01
29	39	68	-8.65E-02	3.52E-01	-5.57E-01
29	40	69	-1.15E-01	3.35E-01	-5.64E-01
29	41	70	-7.64E-02	3.67E-01	-9.86E-01
29	42	71	-1.33E-01	3.00E-01	-1.02E+00
29	43	72	-2.96E-01	2.70E-01	-1.29E+00
30	31	61	3.77E-02	6.60E-01	1.43E+00
30	32	62	-8.89E-02	4.17E-01	-2.03E-01
30	33	63	-1.00E-01	3.62E-01	-5.44E-01
30	34	64	-9.68E-02	3.50E-01	-3.41E-01
30	35	65	-9.38E-02	3.36E-01	-2.81E-01
30	36	66	-9.55E-02	3.33E-01	-2.07E-01
30	37	67	-8.65E-02	3.31E-01	-2.75E-01
30	38	68	-9.08E-02	3.30E-01	-3.69E-01
30	39	69	-9.35E-02	3.30E-01	-4.92E-01
30	40	70	-9.67E-02	3.41E-01	-5.17E-01
30	41	71	-9.18E-02	3.66E-01	-9.20E-01
30	42	72	-8.27E-02	3.84E-01	-8.69E-01
30	43	73	-1.23E-01	3.25E-01	-4.99E-01
30	44	74	-9.72E-02	2.88E-01	-1.43E+00
30	45	75	-2.83E-01	3.72E-01	1.18E+00

Z	N	A	mean (cm/ns)	σ (cm/ns)	skewness
31	33	64	-5.13E-02	4.48E-01	6.75E-01
31	34	65	-1.03E-01	3.57E-01	-5.43E-01
31	35	66	-1.04E-01	3.41E-01	-4.27E-01
31	36	67	-1.02E-01	3.28E-01	-3.19E-01
31	37	68	-9.71E-02	3.22E-01	-2.28E-01
31	38	69	-9.10E-02	3.23E-01	-2.93E-01
31	39	70	-9.47E-02	3.21E-01	-3.51E-01
31	40	71	-9.23E-02	3.21E-01	-3.66E-01
31	41	72	-9.51E-02	3.26E-01	-5.36E-01
31	42	73	-8.64E-02	3.34E-01	-5.59E-01
31	43	74	-9.02E-02	3.52E-01	-1.05E+00
31	44	75	-8.68E-02	3.49E-01	-7.46E-01
31	45	76	-1.71E-01	3.78E-01	-1.70E+00
31	46	77	-2.32E-01	2.82E-01	-1.55E+00
32	34	66	-5.72E-02	4.37E-01	7.97E-01
32	35	67	-1.12E-01	3.61E-01	-1.14E-01
32	36	68	-1.10E-01	3.24E-01	-4.71E-01
32	37	69	-1.05E-01	3.19E-01	-3.56E-01
32	38	70	-1.00E-01	3.08E-01	-2.03E-01
32	39	71	-9.40E-02	3.06E-01	-2.10E-01
32	40	72	-9.12E-02	3.04E-01	-2.69E-01
32	41	73	-9.01E-02	3.04E-01	-4.14E-01
32	42	74	-1.06E-01	3.12E-01	-6.15E-01
32	43	75	-1.04E-01	3.27E-01	-9.70E-01
32	44	76	-9.84E-02	3.43E-01	-1.33E+00
32	45	77	-8.98E-02	3.91E-01	-1.93E+00
32	46	78	-1.12E-01	3.54E-01	-5.99E-01
32	47	79	-1.45E-01	4.37E-01	-7.44E-01
33	35	68	-7.48E-02	4.68E-01	1.34E+00
33	36	69	-9.57E-02	3.48E-01	-2.15E-01
33	37	70	-1.11E-01	3.21E-01	-4.60E-01
33	38	71	-1.00E-01	3.05E-01	-3.10E-01
33	39	72	-1.00E-01	2.97E-01	-3.25E-01
33	40	73	-9.39E-02	2.94E-01	-1.97E-01
33	41	74	-8.84E-02	2.87E-01	-2.20E-01
33	42	75	-9.04E-02	2.90E-01	-3.87E-01
33	43	76	-9.44E-02	3.01E-01	-6.60E-01
33	44	77	-9.62E-02	3.20E-01	-1.03E+00
33	45	78	-1.02E-01	3.14E-01	-1.11E+00
33	46	79	-8.89E-02	3.27E-01	-8.63E-01
33	47	80	-8.22E-02	3.23E-01	-8.93E-01
33	48	81	-6.71E-02	2.82E-01	-1.51E+00

Z	N	A	mean (cm/ns)	σ (cm/ns)	skewness
33	49	82	-4.95E-02	1.72E-01	1.53E+00
33	50	83	-2.95E-01	2.57E-01	-3.30E+00
34	36	70	-1.05E-01	4.25E-01	7.79E-01
34	37	71	-1.12E-01	3.46E-01	1.74E-02
34	38	72	-1.17E-01	3.02E-01	-5.05E-01
34	39	73	-1.04E-01	2.97E-01	-4.16E-01
34	40	74	-1.05E-01	2.83E-01	-2.80E-01
34	41	75	-1.01E-01	2.85E-01	-2.51E-01
34	42	76	-9.25E-02	2.76E-01	-2.52E-01
34	43	77	-9.45E-02	2.80E-01	-4.17E-01
34	44	78	-9.66E-02	2.85E-01	-6.85E-01
34	45	79	-9.15E-02	2.80E-01	-6.16E-01
34	46	80	-9.56E-02	3.12E-01	-1.13E+00
34	47	81	-9.79E-02	3.08E-01	-1.07E+00
34	48	82	-1.60E-01	3.66E-01	-1.27E+00
34	49	83	-2.33E-01	3.69E-01	-1.90E+00
34	50	84	-2.90E-01	3.87E-01	-1.65E+00
35	37	72	-1.49E-01	4.01E-01	1.55E+00
35	38	73	-1.03E-01	3.78E-01	3.36E-03
35	39	74	-1.09E-01	3.01E-01	-4.48E-01
35	40	75	-1.15E-01	2.82E-01	-3.88E-01
35	41	76	-1.08E-01	2.77E-01	-3.67E-01
35	42	77	-1.04E-01	2.72E-01	-2.03E-01
35	43	78	-9.50E-02	2.69E-01	-2.47E-01
35	44	79	-9.64E-02	2.66E-01	-3.38E-01
35	45	80	-9.61E-02	2.71E-01	-6.32E-01
35	46	81	-9.54E-02	2.77E-01	-9.01E-01
35	47	82	-9.95E-02	2.94E-01	-1.08E+00
35	48	83	-1.04E-01	3.05E-01	-1.35E+00
35	49	84	-1.01E-01	3.49E-01	-1.18E+00
35	50	85	-1.42E-01	3.08E-01	-2.13E+00
35	51	86	-2.89E-01	4.61E-01	-2.44E+00
35	52	87	-2.71E-01	4.61E-01	-2.16E-01
36	37	73	-1.75E-01	2.05E-01	-6.37E-01
36	38	74	-6.88E-02	3.20E-01	4.83E-01
36	39	75	-1.05E-01	3.00E-01	5.02E-02
36	40	76	-1.12E-01	2.83E-01	-1.82E-02
36	41	77	-1.12E-01	2.72E-01	-6.00E-02
36	42	78	-1.07E-01	2.62E-01	-7.45E-02
36	43	79	-1.06E-01	2.59E-01	-6.55E-02
36	44	80	-9.48E-02	2.56E-01	-8.71E-02
36	45	81	-9.26E-02	2.53E-01	-1.22E-01

Z	N	A	mean (cm/ns)	σ (cm/ns)	skewness
36	46	82	-9.27E-02	2.54E-01	-2.66E-01
36	47	83	-8.71E-02	2.48E-01	-3.89E-01
36	48	84	-9.37E-02	2.71E-01	-8.55E-01
36	49	85	-8.93E-02	2.72E-01	-7.97E-01
36	50	86	-9.59E-02	3.15E-01	-1.11E+00
36	51	87	-1.27E-01	3.35E-01	-1.48E+00
36	52	88	-8.80E-02	3.01E-01	-1.54E+00
36	53	89	1.51E-03	4.67E-01	-1.80E+00
36	54	90	-2.87E-01	4.91E-01	-1.54E+00
37	39	76	9.03E-02	4.73E-01	1.22E+00
37	40	77	-8.99E-02	2.95E-01	1.01E+00
37	41	78	-1.21E-01	2.75E-01	6.76E-02
37	42	79	-1.05E-01	2.65E-01	-1.11E-02
37	43	80	-1.07E-01	2.55E-01	-9.41E-02
37	44	81	-1.05E-01	2.49E-01	-8.13E-02
37	45	82	-9.77E-02	2.50E-01	-8.25E-02
37	46	83	-9.02E-02	2.41E-01	-1.51E-01
37	47	84	-9.03E-02	2.42E-01	-2.20E-01
37	48	85	-8.29E-02	2.45E-01	-3.42E-01
37	49	86	-9.26E-02	2.59E-01	-8.40E-01
37	50	87	-8.46E-02	2.65E-01	-9.68E-01
37	51	88	-8.06E-02	2.85E-01	-1.22E+00
37	52	89	-1.06E-01	2.95E-01	-1.48E+00
37	53	90	-1.01E-01	3.47E-01	-1.49E+00
37	54	91	-2.23E-02	3.70E-01	-5.09E-01
37	55	92	-4.64E-02	2.69E-01	-2.07E+00
37	56	93	1.55E-01	3.00E-02	0.00E+00
37	57	94	2.31E-02	1.09E-01	2.51E+00
37	58	95	-3.00E-01	1.73E-01	1.53E+00
38	39	77	-9.95E-02	2.55E-01	-3.49E-01
38	40	78	-1.16E-01	3.62E-01	1.84E-01
38	41	79	-1.01E-01	2.86E-01	9.73E-02
38	42	80	-1.16E-01	2.64E-01	-1.08E-01
38	43	81	-1.14E-01	2.53E-01	-2.83E-02
38	44	82	-1.08E-01	2.46E-01	-5.52E-02
38	45	83	-1.07E-01	2.39E-01	-7.05E-02
38	46	84	-1.01E-01	2.37E-01	-8.46E-02
38	47	85	-9.08E-02	2.32E-01	-1.12E-01
38	48	86	-8.62E-02	2.31E-01	-1.45E-01
38	49	87	-8.37E-02	2.32E-01	-3.40E-01
38	50	88	-8.47E-02	2.34E-01	-5.68E-01
38	51	89	-9.23E-02	2.54E-01	-1.09E+00

Z	N	A	mean (cm/ns)	σ (cm/ns)	skewness
38	52	90	-9.14E-02	2.73E-01	-1.53E+00
38	53	91	-1.06E-01	3.00E-01	-1.65E+00
38	54	92	-8.31E-02	2.66E-01	-1.33E+00
38	55	93	-1.76E-01	3.38E-01	-1.99E+00
38	56	94	-2.08E-01	2.14E-01	-1.61E+00
38	58	96	6.50E-02	3.00E-02	0.00E+00
38	59	97	1.34E-02	1.76E-01	1.57E+00
39	41	80	6.94E-02	2.88E-01	2.02E-02
39	42	81	-4.51E-02	3.50E-01	1.60E+00
39	43	82	-1.11E-01	2.52E-01	2.35E-01
39	44	83	-1.17E-01	2.44E-01	-9.44E-02
39	45	84	-1.08E-01	2.38E-01	-6.75E-02
39	46	85	-1.04E-01	2.30E-01	-8.05E-02
39	47	86	-1.01E-01	2.28E-01	-8.53E-02
39	48	87	-9.26E-02	2.24E-01	-1.37E-01
39	49	88	-8.78E-02	2.20E-01	-1.35E-01
39	50	89	-8.19E-02	2.17E-01	-1.86E-01
39	51	90	-8.61E-02	2.31E-01	-7.77E-01
39	52	91	-8.94E-02	2.41E-01	-1.11E+00
39	53	92	-8.90E-02	2.57E-01	-1.43E+00
39	54	93	-9.18E-02	2.68E-01	-1.66E+00
39	55	94	-1.11E-01	3.13E-01	-1.86E+00
39	56	95	-1.22E-01	3.26E-01	-1.60E+00
39	57	96	-9.55E-02	3.10E-01	-2.90E+00
40	41	81	-2.15E-01	4.00E-02	0.00E+00
40	42	82	-2.82E-02	3.12E-01	7.37E-01
40	43	83	-1.26E-01	2.42E-01	-2.70E-01
40	44	84	-1.17E-01	2.40E-01	4.08E-02
40	45	85	-1.06E-01	2.45E-01	1.46E-01
40	46	86	-1.07E-01	2.30E-01	-3.80E-02
40	47	87	-9.94E-02	2.22E-01	-8.06E-02
40	48	88	-9.91E-02	2.19E-01	-6.34E-02
40	49	89	-8.92E-02	2.15E-01	-9.15E-02
40	50	90	-8.33E-02	2.11E-01	-1.22E-01
40	51	91	-7.83E-02	2.08E-01	-1.93E-01
40	52	92	-7.53E-02	2.12E-01	-5.52E-01
40	53	93	-7.50E-02	2.19E-01	-8.88E-01
40	54	94	-7.92E-02	2.32E-01	-1.23E+00
40	55	95	-7.63E-02	2.47E-01	-1.49E+00
40	56	96	-7.84E-02	2.59E-01	-1.88E+00
40	57	97	-7.75E-02	2.49E-01	-1.75E+00
40	58	98	-1.01E-01	2.61E-01	-2.22E+00

Z	N	A	mean (cm/ns)	σ (cm/ns)	skewness
40	59	99	-9.73E-02	2.73E-01	-2.10E+00
40	60	100	-1.67E-01	2.48E-01	-4.13E+00
40	61	101	1.72E-01	1.89E-02	-7.07E-01
40	63	103	7.00E-02	5.50E-02	3.91E-17
41	44	85	-1.19E-01	2.54E-01	7.55E-02
41	45	86	-1.01E-01	2.66E-01	1.21E+00
41	46	87	-1.08E-01	2.32E-01	1.05E-01
41	47	88	-1.05E-01	2.26E-01	3.07E-02
41	48	89	-1.01E-01	2.14E-01	-1.12E-01
41	49	90	-9.78E-02	2.09E-01	-5.47E-02
41	50	91	-8.73E-02	2.06E-01	-6.85E-02
41	51	92	-8.37E-02	2.03E-01	-1.28E-01
41	52	93	-7.79E-02	2.02E-01	-1.88E-01
41	53	94	-7.60E-02	2.02E-01	-3.50E-01
41	54	95	-6.99E-02	2.01E-01	-6.05E-01
41	55	96	-6.66E-02	2.09E-01	-1.12E+00
41	56	97	-6.92E-02	2.32E-01	-1.78E+00
41	57	98	-6.18E-02	2.31E-01	-1.75E+00
41	58	99	-5.42E-02	2.38E-01	-1.85E+00
41	59	100	-6.54E-02	2.55E-01	-2.34E+00
41	60	101	-3.46E-02	1.64E-01	-2.14E+00
41	61	102	-6.68E-02	2.45E-01	-2.16E+00
41	62	103	-1.15E-01	3.14E-01	-3.01E+00
41	63	104	-2.01E-01	4.84E-01	-1.45E+00
41	64	105	1.98E-01	4.26E-02	-1.02E+00
41	65	106	1.87E-01	1.68E-01	-2.19E-01
41	66	107	7.22E-02	1.14E-01	-2.13E-01
42	45	87	-4.68E-02	2.86E-01	6.92E-01
42	46	88	-9.36E-02	2.98E-01	1.70E+00
42	47	89	-1.09E-01	2.30E-01	5.59E-01
42	48	90	-1.06E-01	2.15E-01	-1.01E-02
42	49	91	-9.87E-02	2.07E-01	-8.16E-02
42	50	92	-9.70E-02	2.01E-01	-4.77E-02
42	51	93	-8.90E-02	2.00E-01	-8.64E-02
42	52	94	-8.05E-02	1.95E-01	-1.24E-01
42	53	95	-7.81E-02	1.93E-01	-1.65E-01
42	54	96	-7.23E-02	1.92E-01	-2.59E-01
42	55	97	-6.50E-02	1.89E-01	-3.46E-01
42	56	98	-6.22E-02	1.91E-01	-6.84E-01
42	57	99	-6.42E-02	1.97E-01	-1.10E+00
42	58	100	-5.67E-02	1.99E-01	-1.20E+00
42	59	101	-5.18E-02	2.15E-01	-1.65E+00

Z	N	A	mean (cm/ns)	σ (cm/ns)	skewness
42	60	102	-4.34E-02	2.16E-01	-1.98E+00
42	61	103	-5.75E-02	2.06E-01	-2.17E+00
42	62	104	-1.32E-01	2.95E-01	-3.34E+00
42	63	105	-1.85E-01	2.95E-01	-3.08E+00
42	64	106	1.26E-01	6.81E-02	8.35E-01
42	65	107	-2.69E-01	5.49E-01	-1.63E+00
42	66	108	1.73E-01	8.53E-02	1.75E-01
43	46	89	-9.12E-02	1.80E-01	2.85E-02
43	47	90	-1.26E-01	2.01E-01	-3.18E-01
43	48	91	-1.12E-01	2.24E-01	9.38E-02
43	49	92	-1.03E-01	2.05E-01	-5.86E-02
43	50	93	-9.90E-02	1.99E-01	-4.20E-02
43	51	94	-9.74E-02	1.93E-01	-3.92E-02
43	52	95	-8.82E-02	1.92E-01	-6.11E-02
43	53	96	-7.95E-02	1.88E-01	-1.14E-01
43	54	97	-7.61E-02	1.85E-01	-1.04E-01
43	55	98	-6.95E-02	1.81E-01	-1.89E-01
43	56	99	-6.32E-02	1.81E-01	-3.87E-01
43	57	100	-6.02E-02	1.81E-01	-4.50E-01
43	58	101	-5.29E-02	1.75E-01	-5.00E-01
43	59	102	-5.04E-02	1.89E-01	-1.10E+00
43	60	103	-4.97E-02	1.82E-01	-1.30E+00
43	61	104	-4.20E-02	1.80E-01	-7.21E-01
43	62	105	-3.61E-02	1.98E-01	-2.73E+00
43	63	106	-8.21E-02	1.88E-01	-2.03E+00
43	64	107	-5.73E-02	2.36E-01	-3.98E+00
43	65	108	-1.04E-01	3.76E-01	-2.59E+00
43	66	109	-2.85E-01	6.11E-01	-8.70E-01
43	68	111	6.77E-02	1.45E-01	2.57E-01
44	47	91	-7.58E-02	6.95E-02	8.06E-01
44	48	92	-1.23E-01	2.01E-01	1.71E-01
44	49	93	-9.23E-02	2.19E-01	1.11E-01
44	50	94	-1.00E-01	1.99E-01	5.33E-02
44	51	95	-9.80E-02	1.91E-01	-2.70E-02
44	52	96	-9.23E-02	1.85E-01	-6.04E-02
44	53	97	-8.63E-02	1.84E-01	-9.53E-02
44	54	98	-7.83E-02	1.81E-01	-1.13E-01
44	55	99	-7.39E-02	1.75E-01	-9.93E-02
44	56	100	-6.68E-02	1.73E-01	-2.03E-01
44	57	101	-6.09E-02	1.71E-01	-2.69E-01
44	58	102	-5.76E-02	1.69E-01	-2.83E-01
44	59	103	-5.37E-02	1.72E-01	-7.18E-01

Z	N	A	mean (cm/ns)	σ (cm/ns)	skewness
44	60	104	-4.71E-02	1.75E-01	-1.02E+00
44	61	105	-4.56E-02	1.75E-01	-1.28E+00
44	62	106	-3.89E-02	1.86E-01	-1.71E+00
44	63	107	-3.41E-02	1.99E-01	-2.11E+00
44	64	108	-5.08E-02	1.99E-01	-2.20E+00
44	65	109	-3.59E-02	2.24E-01	-3.30E+00
44	66	110	-1.31E-01	2.07E-01	-4.63E+00
44	67	111	3.97E-02	3.59E-01	-3.02E+00
44	68	112	4.40E-02	4.70E-02	-1.45E-01
44	69	113	7.38E-02	4.54E-02	3.54E-01
44	70	114	4.46E-02	1.53E-01	7.05E-02
45	48	93	5.61E-02	2.46E-01	1.25E+00
45	49	94	-9.40E-02	1.75E-01	-2.00E-01
45	50	95	-9.27E-02	1.92E-01	-1.02E-01
45	51	96	-9.80E-02	1.91E-01	8.09E-02
45	52	97	-9.43E-02	1.82E-01	-2.41E-02
45	53	98	-8.75E-02	1.76E-01	-4.41E-02
45	54	99	-8.32E-02	1.76E-01	-9.21E-02
45	55	100	-7.47E-02	1.74E-01	-1.23E-01
45	56	101	-6.92E-02	1.67E-01	-1.19E-01
45	57	102	-6.23E-02	1.66E-01	-1.99E-01
45	58	103	-5.68E-02	1.63E-01	-1.45E-01
45	59	104	-5.29E-02	1.60E-01	-3.64E-01
45	60	105	-4.75E-02	1.60E-01	-5.02E-01
45	61	106	-4.31E-02	1.62E-01	-8.53E-01
45	62	107	-4.00E-02	1.63E-01	-1.18E+00
45	63	108	-3.57E-02	1.63E-01	-1.44E+00
45	64	109	-2.65E-02	1.67E-01	-1.57E+00
45	65	110	-3.27E-02	1.65E-01	-1.83E+00
45	66	111	-3.46E-02	1.74E-01	-3.35E+00
45	67	112	-8.41E-02	1.96E-01	-3.51E+00
45	68	113	-6.99E-02	2.48E-01	-1.70E+00
45	69	114	-8.74E-02	3.93E-01	-3.10E+00
45	70	115	7.42E-03	8.98E-02	1.77E+00
45	71	116	6.11E-02	8.48E-02	1.21E+00
45	72	117	6.90E-02	8.40E-02	7.07E-01
46	50	96	-1.50E-01	2.17E-01	-5.33E-01
46	51	97	-1.12E-01	1.71E-01	3.68E-02
46	52	98	-1.01E-01	1.90E-01	3.42E-01
46	53	99	-8.98E-02	1.79E-01	9.09E-02
46	54	100	-8.76E-02	1.71E-01	-2.95E-02
46	55	101	-8.43E-02	1.69E-01	-8.56E-02

Z	N	A	mean (cm/ns)	σ (cm/ns)	skewness
46	56	102	-7.55E-02	1.65E-01	-7.30E-02
46	57	103	-6.81E-02	1.59E-01	-1.09E-01
46	58	104	-6.36E-02	1.58E-01	-1.31E-01
46	59	105	-5.72E-02	1.56E-01	-3.08E-01
46	60	106	-5.01E-02	1.52E-01	-2.41E-01
46	61	107	-4.58E-02	1.51E-01	-3.75E-01
46	62	108	-4.05E-02	1.49E-01	-4.98E-01
46	63	109	-3.66E-02	1.52E-01	-1.01E+00
46	64	110	-3.17E-02	1.50E-01	-9.41E-01
46	65	111	-3.25E-02	1.65E-01	-1.84E+00
46	66	112	-2.35E-02	1.46E-01	-1.29E+00
46	67	113	-2.89E-02	1.66E-01	-1.65E+00
46	68	114	-4.41E-02	1.78E-01	-3.96E+00
46	69	115	-7.56E-02	1.54E-01	-2.94E+00
46	70	116	-1.90E-02	2.60E-01	-3.82E+00
46	71	117	7.85E-03	7.33E-02	-2.06E-01
46	72	118	3.61E-02	1.47E-01	9.31E-02
46	73	119	-2.83E-02	1.54E-01	-2.42E-01
46	74	120	3.70E-02	1.23E-01	-2.16E-01
47	51	98	2.23E-02	3.96E-01	8.90E-01
47	52	99	-1.08E-01	1.78E-01	-1.96E-01
47	53	100	-1.01E-01	1.72E-01	-1.27E-01
47	54	101	-8.78E-02	1.72E-01	-8.14E-02
47	55	102	-8.37E-02	1.62E-01	-7.86E-02
47	56	103	-7.99E-02	1.60E-01	-8.81E-02
47	57	104	-7.28E-02	1.57E-01	-1.03E-01
47	58	105	-6.21E-02	1.51E-01	-1.00E-01
47	59	106	-5.84E-02	1.51E-01	-1.34E-01
47	60	107	-5.26E-02	1.47E-01	-1.47E-01
47	61	108	-4.40E-02	1.45E-01	-2.50E-01
47	62	109	-3.99E-02	1.42E-01	-2.93E-01
47	63	110	-3.59E-02	1.40E-01	-4.85E-01
47	64	111	-2.94E-02	1.39E-01	-8.51E-01
47	65	112	-2.65E-02	1.40E-01	-8.22E-01
47	66	113	-2.09E-02	1.39E-01	-1.10E+00
47	67	114	-1.10E-02	1.34E-01	-8.86E-01
47	68	115	-1.44E-02	1.45E-01	-2.02E+00
47	69	116	-1.22E-02	1.26E-01	-2.18E+00
47	70	117	-4.56E-03	1.25E-01	-1.89E+00
47	71	118	-7.53E-02	1.77E-01	-3.53E+00
47	72	119	5.88E-02	1.27E-01	-2.50E+00
47	73	120	-1.78E-02	8.02E-02	9.85E-01

Z	N	A	mean (cm/ns)	σ (cm/ns)	skewness
47	74	121	2.90E-02	1.04E-01	-7.51E-01
47	75	122	5.01E-02	9.43E-02	-2.33E-01
48	52	100	-1.41E-01	4.01E-02	-2.69E-01
48	53	101	-1.00E-01	1.86E-01	-2.24E-01
48	54	102	-8.57E-02	1.67E-01	-2.08E-01
48	55	103	-8.65E-02	1.70E-01	2.78E-01
48	56	104	-8.65E-02	1.57E-01	5.19E-02
48	57	105	-7.93E-02	1.55E-01	-9.24E-02
48	58	106	-7.22E-02	1.50E-01	-6.48E-02
48	59	107	-6.13E-02	1.45E-01	-1.17E-01
48	60	108	-5.82E-02	1.44E-01	-1.04E-01
48	61	109	-4.96E-02	1.39E-01	-7.10E-02
48	62	110	-4.36E-02	1.37E-01	-2.54E-01
48	63	111	-3.84E-02	1.35E-01	-2.76E-01
48	64	112	-3.23E-02	1.32E-01	-4.77E-01
48	65	113	-2.85E-02	1.31E-01	-6.27E-01
48	66	114	-2.36E-02	1.31E-01	-9.09E-01
48	67	115	-1.71E-02	1.30E-01	-1.01E+00
48	68	116	-1.21E-02	1.32E-01	-1.52E+00
48	69	117	-7.85E-03	1.30E-01	-1.92E+00
48	70	118	-7.73E-04	1.27E-01	-1.49E+00
48	71	119	-5.98E-04	1.30E-01	-2.56E+00
48	72	120	-2.28E-02	1.13E-01	-2.67E+00
48	73	121	-2.03E-02	2.49E-01	-1.52E+00
48	74	122	1.49E-02	1.06E-01	-2.42E+00
48	75	123	-6.77E-02	2.37E-01	-1.82E+00
48	76	124	2.33E-02	1.10E-01	-1.15E+00
48	77	125	4.23E-02	8.80E-02	-5.33E-01
49	53	102	3.66E-02	1.51E-01	-4.28E-01
49	54	103	-3.54E-02	1.98E-01	2.42E-01
49	55	104	-1.00E-01	1.55E-01	-2.49E-01
49	56	105	-8.68E-02	1.67E-01	7.27E-01
49	57	106	-8.33E-02	1.50E-01	2.22E-01
49	58	107	-7.80E-02	1.50E-01	-2.34E-02
49	59	108	-7.07E-02	1.42E-01	-4.79E-02
49	60	109	-5.93E-02	1.39E-01	-1.87E-01
49	61	110	-5.61E-02	1.36E-01	-7.01E-02
49	62	111	-4.60E-02	1.31E-01	-1.46E-01
49	63	112	-4.06E-02	1.31E-01	-1.78E-01
49	64	113	-3.34E-02	1.27E-01	-3.13E-01
49	65	114	-2.71E-02	1.24E-01	-4.54E-01
49	66	115	-2.32E-02	1.23E-01	-4.10E-01

Z	N	A	mean (cm/ns)	σ (cm/ns)	skewness
49	67	116	-1.71E-02	1.19E-01	-6.08E-01
49	68	117	-1.23E-02	1.17E-01	-8.14E-01
49	69	118	-7.67E-03	1.18E-01	-9.30E-01
49	70	119	2.65E-03	1.17E-01	-1.55E+00
49	71	120	6.35E-03	1.20E-01	-1.43E+00
49	72	121	1.50E-02	1.14E-01	-1.76E+00
49	73	122	2.03E-02	1.19E-01	-3.02E+00
49	74	123	-6.95E-02	1.40E-01	-3.86E+00
49	75	124	3.09E-02	1.74E-01	-2.79E+00
49	76	125	-1.93E-03	8.66E-02	-6.37E+00
49	77	126	4.57E-02	1.08E-01	-2.13E+00
49	78	127	-5.64E-02	3.24E-01	-3.24E+00
50	55	105	-1.40E-01	9.26E-02	8.41E-01
50	56	106	-1.02E-01	1.56E-01	-5.68E-01
50	57	107	-8.77E-02	1.42E-01	3.44E-03
50	58	108	-7.48E-02	1.43E-01	9.48E-02
50	59	109	-7.59E-02	1.42E-01	-1.57E-01
50	60	110	-6.64E-02	1.34E-01	-6.02E-02
50	61	111	-5.80E-02	1.34E-01	-1.30E-01
50	62	112	-5.27E-02	1.28E-01	-6.90E-02
50	63	113	-4.22E-02	1.25E-01	-1.90E-01
50	64	114	-3.55E-02	1.23E-01	-1.75E-01
50	65	115	-2.88E-02	1.18E-01	-2.43E-01
50	66	116	-2.08E-02	1.16E-01	-3.22E-01
50	67	117	-1.78E-02	1.14E-01	-3.78E-01
50	68	118	-1.09E-02	1.11E-01	-6.89E-01
50	69	119	-7.06E-03	1.10E-01	-6.68E-01
50	70	120	-1.70E-03	1.06E-01	-7.84E-01
50	71	121	6.34E-03	1.06E-01	-1.01E+00
50	72	122	8.83E-03	1.05E-01	-1.38E+00
50	73	123	1.91E-02	1.05E-01	-1.68E+00
50	74	124	4.21E-02	1.13E-01	-1.07E+00
50	75	125	2.08E-02	8.52E-02	-5.00E+00
50	76	126	-7.13E-02	1.63E-01	-5.56E-01
50	77	127	-1.44E-02	1.80E-01	-2.20E+00
50	78	128	-1.34E-01	2.68E-01	-1.41E+00
50	79	129	-1.14E-01	3.47E-01	-1.87E+00
50	80	130	2.18E-02	1.30E-01	-3.09E+00
51	57	108	-1.11E-01	1.74E-01	1.06E+00
51	58	109	-7.26E-02	1.06E-01	-1.26E-01
51	59	110	-8.39E-02	1.36E-01	-1.98E-01
51	60	111	-7.19E-02	1.40E-01	2.60E-01

Z	N	A	mean (cm/ns)	σ (cm/ns)	skewness
51	61	112	-6.32E-02	1.28E-01	-7.62E-02
51	62	113	-4.99E-02	1.26E-01	-9.61E-02
51	63	114	-4.44E-02	1.20E-01	-7.75E-02
51	64	115	-3.42E-02	1.18E-01	-1.26E-01
51	65	116	-2.82E-02	1.15E-01	-1.12E-01
51	66	117	-1.87E-02	1.09E-01	-1.65E-01
51	67	118	-1.28E-02	1.09E-01	-3.01E-01
51	68	119	-8.61E-03	1.04E-01	-3.78E-01
51	69	120	-1.50E-03	1.03E-01	-5.29E-01
51	70	121	2.05E-03	9.98E-02	-5.44E-01
51	71	122	8.89E-03	9.63E-02	-7.83E-01
51	72	123	1.29E-02	9.35E-02	-5.57E-01
51	73	124	1.89E-02	9.27E-02	-9.71E-01
51	74	125	2.71E-02	9.24E-02	-1.23E+00
51	75	126	3.30E-02	9.20E-02	-1.30E+00
51	76	127	6.03E-02	9.52E-02	-1.25E+00
51	77	128	-2.75E-02	6.90E-02	-4.30E+00
51	78	129	5.06E-02	1.24E-01	-3.95E+00
51	79	130	1.55E-02	1.08E-01	-4.27E+00
51	80	131	8.80E-03	2.39E-01	-2.74E+00
51	81	132	-8.62E-02	3.47E-01	-2.09E+00
52	58	110	6.71E-02	1.51E-01	-6.88E-01
52	59	111	-7.86E-02	1.16E-01	-6.98E-01
52	60	112	-8.40E-02	1.57E-01	1.27E+00
52	61	113	-7.16E-02	1.32E-01	5.27E-01
52	62	114	-6.06E-02	1.22E-01	-1.46E-01
52	63	115	-5.17E-02	1.24E-01	1.85E-01
52	64	116	-4.42E-02	1.12E-01	-1.13E-01
52	65	117	-3.14E-02	1.11E-01	-1.96E-01
52	66	118	-2.83E-02	1.07E-01	-7.95E-02
52	67	119	-1.52E-02	1.02E-01	-2.79E-01
52	68	120	-1.18E-02	1.01E-01	-1.02E-01
52	69	121	-3.28E-03	9.40E-02	-4.55E-01
52	70	122	9.76E-04	9.53E-02	-3.78E-01
52	71	123	4.43E-03	8.99E-02	-4.57E-01
52	72	124	1.28E-02	8.92E-02	-6.74E-01
52	73	125	1.48E-02	8.55E-02	-6.31E-01
52	74	126	2.45E-02	8.13E-02	-7.79E-01
52	75	127	2.67E-02	8.02E-02	-9.51E-01
52	76	128	3.72E-02	7.65E-02	-1.21E+00
52	77	129	4.21E-02	8.37E-02	-8.84E-01
52	78	130	4.30E-02	6.36E-02	-3.55E+00

Z	N	A	mean (cm/ns)	σ (cm/ns)	skewness
52	79	131	1.20E-02	1.46E-01	-1.22E+00
52	80	132	4.90E-02	7.88E-02	-3.63E+00
52	81	133	-4.22E-02	1.74E-01	-3.32E+00
52	82	134	2.31E-03	1.97E-01	-3.57E+00
53	60	113	-4.29E-02	1.74E-01	1.18E+00
53	61	114	-8.38E-02	1.24E-01	2.69E-01
53	62	115	-8.48E-02	1.31E-01	8.64E-02
53	63	116	-6.51E-02	1.19E-01	1.82E-01
53	64	117	-6.26E-02	1.14E-01	5.43E-03
53	65	118	-4.88E-02	1.02E-01	-2.98E-01
53	66	119	-4.01E-02	1.08E-01	-1.58E-01
53	67	120	-3.43E-02	9.64E-02	-6.54E-02
53	68	121	-1.99E-02	9.81E-02	-3.18E-01
53	69	122	-2.09E-02	9.19E-02	-1.16E-01
53	70	123	-4.35E-03	8.87E-02	-1.74E-01
53	71	124	-9.42E-03	8.86E-02	-1.70E-01
53	72	125	5.09E-03	7.94E-02	-5.69E-01
53	73	126	4.18E-03	8.23E-02	-4.49E-01
53	74	127	1.26E-02	7.17E-02	-5.67E-01
53	75	128	1.76E-02	7.57E-02	-8.33E-01
53	76	129	2.16E-02	6.64E-02	-7.55E-01
53	77	130	3.34E-02	7.01E-02	-1.03E+00
53	78	131	3.54E-02	6.55E-02	-6.02E-01
53	79	132	6.18E-02	7.26E-02	-8.42E-01
53	80	133	9.55E-03	4.99E-02	-3.25E+00
53	81	134	5.12E-02	5.49E-02	-5.26E+00
53	82	135	4.93E-02	5.14E-02	-6.36E+00
54	62	116	-2.72E-02	3.16E-01	2.47E+00
54	63	117	-1.02E-01	1.15E-01	-5.37E-01
54	64	118	-7.63E-02	1.12E-01	-2.63E-01
54	65	119	-6.59E-02	1.08E-01	2.01E-01
54	66	120	-4.94E-02	9.99E-02	-2.31E-01
54	67	121	-4.94E-02	9.82E-02	8.07E-02
54	68	122	-3.15E-02	8.81E-02	-2.70E-01
54	69	123	-2.76E-02	9.23E-02	-1.63E-01
54	70	124	-1.81E-02	8.05E-02	-5.86E-01
54	71	125	-1.06E-02	8.44E-02	-2.59E-01
54	72	126	-7.61E-03	7.54E-02	6.63E-01
54	73	127	4.39E-03	7.72E-02	4.65E-01
54	74	128	2.67E-03	7.25E-02	1.51E+00
54	75	129	1.85E-02	6.87E-02	9.91E-01
54	76	130	1.66E-02	6.58E-02	7.50E-01

Z	N	A	mean (cm/ns)	σ (cm/ns)	skewness
54	77	131	3.37E-02	5.74E-02	-1.39E-01
54	78	132	3.49E-02	5.35E-02	4.12E-01
54	79	133	4.99E-02	4.54E-02	3.75E-01
54	80	134	4.55E-02	3.65E-02	4.84E-01
54	81	135	5.70E-02	2.71E-02	-3.34E+00
54	82	136	-1.10E-01	8.12E-02	-2.10E+00
54	83	137	-2.97E-01	2.49E-01	4.24E-01
55	63	118	-9.03E-02	6.03E-02	-8.42E-02
55	64	119	-1.89E-01	1.38E-01	-9.75E-02
55	65	120	-8.05E-02	1.08E-01	7.73E-01
55	66	121	-7.49E-02	9.41E-02	6.29E-02
55	67	122	-7.36E-02	9.83E-02	-3.73E-01
55	68	123	-6.27E-02	9.20E-02	1.42E+00
55	69	124	-5.09E-02	8.62E-02	-3.24E-01
55	70	125	-4.70E-02	8.11E-02	7.69E-02
55	71	126	-3.27E-02	7.61E-02	-9.57E-01
55	72	127	-3.28E-02	7.35E-02	-3.01E-01
55	73	128	-1.81E-02	6.78E-02	2.80E-01
55	74	129	-1.96E-02	6.89E-02	6.26E-01
55	75	130	-7.65E-03	6.01E-02	-7.17E-01
55	76	131	-6.75E-03	7.05E-02	4.60E+00
55	77	132	6.59E-05	5.80E-02	9.54E-01
55	78	133	2.57E-03	5.44E-02	-2.97E+00
55	79	134	7.77E-03	5.01E-02	-3.03E+00
55	80	135	1.27E-02	6.30E-02	-3.99E+00
55	81	136	3.22E-02	7.99E-02	-2.82E+00
55	82	137	1.23E-01	7.86E-02	-4.18E+00
55	83	138	-5.70E-02	6.18E-02	-6.98E+00
56	66	122	-1.09E-01	1.48E-01	9.58E-01
56	67	123	-1.09E-01	8.39E-02	2.25E-01
56	68	124	-1.12E-01	8.96E-02	2.00E-01
56	69	125	-7.49E-02	7.14E-02	-1.53E-01
56	70	126	-7.63E-02	8.81E-02	-8.43E-01
56	71	127	-6.53E-02	7.47E-02	-3.70E-01
56	72	128	-6.11E-02	8.14E-02	-1.46E+00
56	73	129	-6.01E-02	9.47E-02	-3.63E+00
56	74	130	-4.91E-02	8.27E-02	-2.28E+00
56	75	131	-5.18E-02	9.82E-02	-6.01E+00
56	76	132	-3.96E-02	8.41E-02	-2.24E+00
56	77	133	-5.70E-02	1.72E-01	-4.52E+00
56	78	134	-3.33E-02	1.12E-01	-1.86E+00
56	79	135	-3.19E-02	6.66E-02	-1.87E-01

Z	N	A	mean (cm/ns)	σ (cm/ns)	skewness
56	80	136	1.43E-01	3.54E-01	6.89E-01
56	81	137	2.39E-02	1.54E-01	-6.35E+00
56	82	138	2.08E-02	1.60E-01	-5.05E+00
56	83	139	3.26E-02	8.13E-02	-6.69E+00
56	84	140	5.41E-02	5.93E-02	-6.16E+00
56	85	141	-1.40E-01	8.95E-02	-1.43E+00
56	86	142	-2.99E-01	2.77E-01	7.56E-01

Longitudinal velocity as a function of the impact parameter

The following table gives the reconstructed correlation between observed mean longitudinal velocity and the impact parameter, using the method described in chapter 6 and the data from the experiment ^{136}Xe+Pb at 1 AGeV.

b (fm)	$v_\parallel$ (cm/ns)
9.99074	-1.33E-01
10.0054	-2.28E-01
10.0308	-1.83E-01
10.0666	-2.39E-01
10.0916	-2.98E-01
10.109	-3.66E-01
10.134	-4.12E-01
10.1688	-4.60E-01
10.191	-5.44E-01
10.2001	-5.52E-01
10.2093	-5.93E-01
10.2324	-6.36E-01
10.2676	-6.81E-01
10.2906	-7.14E-01
10.3	-7.80E-01
10.3094	-8.38E-01
10.3324	-8.32E-01
10.3676	-9.39E-01
10.3906	-8.89E-01
10.4	-9.71E-01
10.4094	-9.25E-01
10.4324	-1.01E+00
10.4676	-9.93E-01
10.4906	-1.02E+00
10.5	-1.05E+00
10.5094	-1.02E+00
10.5324	-1.12E+00
10.5676	-1.10E+00
10.5907	-1.13E+00
10.5999	-1.09E+00
10.6089	-1.17E+00
10.6313	-1.12E+00
10.6661	-1.14E+00
10.6911	-1.12E+00
10.7083	-1.16E+00

b (fm)	$v_\parallel$ (cm/ns)
10.7328	-1.18E+00
10.7673	-1.14E+00
10.7916	-1.19E+00
10.8085	-1.15E+00
10.8328	-1.22E+00
10.8672	-1.16E+00
10.8912	-1.19E+00
10.9073	-1.17E+00
10.9312	-1.17E+00
10.9673	-1.17E+00
10.9989	-1.13E+00
11.0307	-1.16E+00
11.0689	-1.12E+00
11.1001	-1.15E+00
11.1312	-1.10E+00
11.169	-1.12E+00
11.2	-1.09E+00
11.2307	-1.09E+00
11.2678	-1.07E+00
11.2984	-1.06E+00
11.3313	-1.04E+00
11.3766	-1.01E+00
11.423	-1.00E+00
11.4677	-9.71E-01
11.5001	-9.57E-01
11.5325	-9.22E-01
11.5771	-9.08E-01
11.6231	-8.87E-01
11.6676	-8.60E-01
11.6996	-8.53E-01
11.7312	-8.06E-01
11.7751	-7.99E-01
11.8224	-7.61E-01
11.8745	-7.43E-01
11.924	-7.00E-01
11.9757	-6.94E-01
12.0241	-6.42E-01
12.0746	-6.29E-01
12.1224	-5.71E-01
12.1747	-5.43E-01
12.2301	-5.01E-01
12.2981	-4.63E-01

b (fm)	$v_\parallel$ (cm/ns)
12.3677	-4.04E-01
12.4304	-3.85E-01
12.499	-3.27E-01
12.5676	-3.17E-01
12.6315	-2.59E-01
12.7075	-2.56E-01
12.7904	-2.13E-01
12.864	-1.96E-01
12.9264	-1.43E-01
13.0029	-1.38E-01
13.1036	-1.03E-01
13.2292	-7.70E-02
13.3707	-2.30E-02
13.4995	-1.00E-03
13.6058	1.17E-01
13.7071	2.05E-01
13.9215	2.50E-01
14.4844	2.20E-01
15.6788	4.43E-01

Bibliography

[ABB+04]   P. Armbruster, J. Benlliure, M. Bernas, A. Boudard, E. Casarejos, S. Czajkowski, T. Enqvist, S. Leray, P. Napolitani, J. Pereira, F. Rejmund, M.-V. Ricciardi, K.-H. Schmidt, C. Stéphan, J. Taieb, L. Tassan-Got, and C. Volant, *Measurement of a complete set of nuclides, cross sections, and kinetic energies in spallation of ^{238}U 1A GeV with protons*, Phys. Rev. Lett. **93** (2004), 212701.

[AH84]   M. Asghar and R.W. Hasse, *Saddle-to-scission landscape in fission : experiments and theories*, J. Phys. Colloques **45** (1984), 455.

[ATGA+06]   L. Audouin, L. Tassan-Got, P. Armbruster, J. Benlliure, M. Bernas, A. Boudard, E. Casarejos, S. Czajkowski, T. Enqvist, B. Fernandez-Dominguez, B. Jurado, R. Legrain, S. Leray, B. Mustapha, J. Pereira, M. Pravikoff, F. Rejmund, M.-V. Ricciardi, K.-H. Schmidt, C. Stephan, J. Taieb, C. Volant, and W. Wlazlo, *Evaporation residues produced in spallation of ^{208}Pb by protons at 500 A MeV*, Nucl. Phys. A **768** (2006), 1.

[BAB+98]   J. Benlliure, P. Armbruster, M. Bernas, C. Böckstiegel, S. Czajkowski, C. Donzaud, H. Geissel, A. Heinz, C. Kozhuharov, Ph. Dessagne, G. Münzenberg, M. Pfützner, C. Stéphan, K.-H. Schmidt, K. Sümmerer, W. Schwab, L. Tassan-Got, and B. Voss, *Production of medium-weight isotopes by fragmentation in 750 A MeV ^{238}U on ^{208}Pb collisions*, Eur. Phys. J. A **2** (1998), 193.

[BAB+02]   J. Benlliure, P. Armbruster, M. Bernas, A. Boudard, T. Enqvist, R. Legrain, S. Leray, F. Rejmund, K.-H. Schmidt, C. Stephan, L. Tassan-Got, and C. Volant, *Signatures of fission dynamics in highly excited nuclei produced in ^{197}Au (800 A MeV) on proton collisions*, Nucl. Phys. A **700** (2002), 469.

[BAB+03]   M. Bernas, P. Armbruster, J. Benlliure, A. Boudard, E. Casarejos, S. Czajkowski, T. Enqvist, R. Legrain, S. Leray, B. Mustapha, P. Napolitani, J. Pereira, F. Rejmund, M. V. Ricciardi, K.-H. Schmidt, C. Stéphan, J. Taieb, L. Tassan-Got, and C. Volant, *Fission residues produced in the spallation reaction $^{238}U + p$ at 1 A GeV*, Nucl. Phys. A **725** (2003), 213.

[BAB⁺06]   M. Bernas, P. Armbruster, J. Benlliure, A. Boudard, E. Casarejos, T. Enqvist, A. Kelic, R. Legrain, S. Leray, J. Pereira, F. Rejmund, M.-V. Ricciardi, K.-H. Schmidt, C. Stephan, J. Taieb, L. Tassan-Got, and C. Volant, *Very heavy fission fragments produced in the spallation reaction $^{238}U + p$ at 1 A GeV*, Nucl. Phys. A **765** (2006), 197.

[Bas]   R. Bass, *Fusion reactions: successes and limitations of a one-dimensional description*, Lecture notes in Physics vol. 117: Deep-Inelastic and Fusion Reactions with Heavy Ions (W. Oertzen, ed.).

[Bau95]   W. Bauer, *Temperatures of fragment kinetic energy spectra*, Phys. Rev. C **51** (1995), 803.

[BBI⁺95]   J.P. Bondorf, A.S. Botvina, A.S. Iljinov, I.N. Mishustin, and K. Sneppen, *Statistical multifragmentation of nuclei*, Phys. Rep. **257** (1995), 133.

[BSB⁺97]   C. Böckstiegel, S. Steinhäuser, J. Benlliure, H.-G. Clerc, A. Grewe, A. Heinz, M. de Jong, A. R. Junghans, J. Müller, and K.-H. Schmidt, *Total kinetic energies and nuclear-charge yields in the fission of relativistic ^{233}U secondary projectiles*, Phys. Lett. B **398** (1997), 259.

[BST73]   J. D. Bowman, W. J. Swiatecki, and C. E. Tsang, *Abrasion and ablation of heavy ions*, Lawrence Berkeley Laboratory report **LBL-2908** (1973).

[Cam86]   X. Campi, *Multifragmentation: nuclei break-up like percolation clusters*, Journal of Physics A: Mathematical and General **19** (1986), L917.

[Car95]   B. V. Carlson, *Microscopic abrasion-ablation approximation to projectile fragmentation*, Phys. Rev. C **51** (1995), 252.

[CBP⁺06]   E. Casarejos, J. Benlliure, J. Pereira, P. Armbruster, M. Bernas, A. Boudard, S. Czajkowski, T. Enqvist, R. Legrain, S. Leray, B. Mustapha, M. Pravikoff, F. Rejmund, K.-H. Schmidt, C. Stephan, J. Taieb, L. Tassan-Got, C. Volant, and W. Wlazlo, *Isotopic production cross sections of spallation-evaporation residues from reactions of ^{238}U (1 A GeV) with deuterium*, Phys. Rev. C **74** (2006), 044609.

[CDS87]   K. C. Chung, R. Donangelo, and H. Schechter, *Dynamical effects in the Coulomb expansion following nuclear fragmentation*, Phys. Rev. C **36** (1987), 986.

[Dan02]   P. Danielewicz, *Bulk nuclear properties from reactions*, arXiv:0203002v1 (2002).

[DCA⁺98]   C. Donzaud, S. Czajkowski, P. Armbruster, M. Bernas, C. Böckstiegel, Ph. Dessagne, H. Geissel, E. Hanelt, A. Heinz, C. Kozhuharov, Ch. Miehé, G. Münzenberg, M. Pfützner, W. Schwab, C. Stéphan, K. Sümmerer,

L. Tassan-Got, and B. Voss, *Low-energy fission investigated in reactions of 750 A MeV ^{238}U-ions on ^{208}Pb. isotopic cross sections.*, Eur. Phys. J. A **1** (1998), 407.

[dJ98]   M. de Jong, *Experimentalle Untersuchungen und Modellrechnungen zur Projektilfragmentation schwerer Kerne am Beispiel von ^{208}Pb*, Ph.D. thesis, TU Darmstadt, 1998.

[dJIS97]   M. de Jong, A.V. Ignatyuk, and K.-H. Schmidt, *Angular momentum in peripheral fragmentation reactions*, Nucl. Phys. A **613** (1997), 435.

[dJSB$^+$98] M. de Jong, K. H. Schmidt, B. Blank, C. Bockstiegel, T. Brohm, H. G. Clerc, S. Czajkowski, M. Dornik, H. Geissel, A. Grewe, E. Hanelt, A. Heinz, H. Irnich, A. R. Junghans, A. Magel, G. Munzenberg, F. Nickel, M. Pfutzner, A. Piechaczek, C. Scheidenberger, W. Schwab, S. Steinhauser, K. Summerer, W. Trinder, B. Voss, and C. Ziegler, *Fragmentation cross sections of relativistic ^{208}Pb projectiles*, Nucl. Phys. A **628** (1998), 479.

[dSNPS06]   R. de Souza, N. Le Neindre, A. Pagano, and K.-H. Schmidt, *Dynamics and thermodynamics with nuclear degrees of freedom: Detection*, Eur. Phys. J. A **30** (2006), 275.

[DSVC06]   J.N. De, S.K. Samaddar, X. Vinas, and M. Centelles, *Nuclear expansion with excitation*, Phys. Lett. B **638** (2006), 160.

[EAB$^+$02]   T. Enqvist, P. Armbruster, J. Benlliure, M. Bernas, A. Boudard, S. Czajkowski, R. Legrain, S. Leray, B. Mustapha, M. Pravikoff, F. Rejmund, K.-H. Schmidt, C. Stéphan, J. Taieb, L. Tassan-Got, F. Vivès, C. Volant, and W. Wlazlo, *Primary-residue production cross sections and kinetic energies in 1 A GeV ^{208}Pb on deuteron reactions*, Nucl. Phys. A **703** (2002), 435.

[EBF$^+$99]   T. Enqvist, J. Benlliure, F. Farget, K.-H. Schmidt, P. Armbruster, M. Bernas, L. Tassan-Got, A. Boudard, R. Legrain, C. Volant, C. Böckstiegel, M. de Jong, and J. P. Dufour, *Systematic experimental survey on projectile fragmentation and fission induced in collisions of ^{238}U at 1 A GeV with lead*, Nucl. Phys. A **658** (1999), 47.

[EWA$^+$01]   T. Enqvist, W. Wlazlo, P. Armbruster, J. Benlliure, M. Bernas, A. Boudard, S. Czajkowski, R. Legrain, S. Leray, B. Mustapha, M. Pravikoff, F. Rejmund, K.-H. Schmidt, C. Stéphan, J. Taieb, L. Tassan-Got, and C. Volant, *Isotopic yields and kinetic energies of primary residues in 1 A GeV $^{208}Pb + p$ reactions*, Nucl. Phys. A **686** (2001), 481.

[FDAA$^+$05] B. Fernandez-Dominguez, P. Armbruster, L. Audouin, J. Benlliure, M. Bernas, A. Boudard, E. Casarejos, S. Czajkowski, J. E. Ducret, T. Enqvist, B. Jurado, R. Legrain, S. Leray, B. Mustapha, J. Pereira, M. Pravikoff,

F. Rejmund, M. V. Ricciardi, K.-H. Schmidt, C. Stephan, J. Taieb, L. Tassan-Got, and C. Volant, *Nuclide cross-sections of fission fragments in the reaction $^{208}Pb + p$ at 500 A MeV*, Nucl. Phys. A **747** (2005), 227.

[FL83] W. A. Friedman and W. G. Lynch, *Statistical formalism for particle emission*, Phys. Rev. C **28** (1983), 16.

[GAB⁺92] H. Geissel, P. Armbruster, K. H. Behr, A. Brunle, K. Burkard, M. Chen, H. Folger, B. Franczak, H. Keller, O. Klepper, B. Langenbeck, F. Nickel, E. Pfeng, M. Pfutzner, E. Roeckl, K. Rykaczewski, I. Schall, D. Schardt, C. Scheidenberger, K. H. Schmidt, A. Schroter, T. Schwab, K. Summerer, M. Weber, G. Munzenberg, T. Brohm, H. G. Clerc, M. Fauerbach, J. J. Gaimard, A. Grewe, E. Hanelt, B. Knodler, M. Steiner, B. Voss, J. Weckenmann, C. Ziegler, A. Magel, H. Wollnik, J. P. Dufour, Y. Fujita, D. J. Vieira, and B. Sherrill, *The GSI projectile fragment separator (FRS): a versatile magnetic system for relativistic heavy ions*, Nucl. Instr. Meth. (1992), 286.

[Gla59] R.J. Glauber, *Lectures in theoretical physics*, vol. 1, Interscience Publishers, New York, 1959.

[Gol74] A.S. Goldhaber, *Statistical models of fragmentation processes*, Phys. Lett. B **53** (1974), 306.

[GS91] J.-J. Gaimard and K.-H. Schmidt, *A reexamination of the abrasion-ablation model for the description of the nuclear fragmentation reaction*, Nucl. Phys. A **531** (1991), 709.

[GSS⁺04] M. Giacomelli, L. Sihver, J. Skvarc, N. Yasuda, and R. Ilic, *Projectilelike fragment emission angles in fragmentation reactions of light heavy ions in the energy region $\leqslant$ 200 MeV/nucleon: Modeling and simulations*, Phys. Rev. C **69** (2004), 064601.

[HAB⁺05] D. Henzlova, L. Audouin, J. Benlliure, A.S. Botvina, A. Boudard, E. Casarejos, J.E. Ducret, T. Enqvist, L.T. Got, A. Heinz, V. Henzl, A. Junghans, B. Jurado, A. Kelic, A. Krasa, T. Kurtukian, S. Leray, P. Napolitani, M.F. Ordonez, J. Pereira, R. Pleskac, F. Rejmund, M.V. Ricciardi, K.-H. Schmidt, Ch. Schmitt, C. Stephan, C. Villagrasa, C. Volant, A. Wagner, and O. Yordanov, *Isotopically resolved residues from the fragmentation of projectiles with largely different N/Z - the isospin-thermometer method*, Nucl. Phys. A **749** (2005), 110.

[Har92] B. G. Harvey, *Beam-velocity fragment yields and momenta in nucleus-nucleus collisions from 20 MeV/nucleon to 200 GeV/nucleon*, Phys. Rev. C **45** (1992), 1748.

[HBF$^+$84]   A. S. Hirsch, A. Bujak, J. E. Finn, L. J. Gutay, R. W. Minich, N. T. Porile, R. P. Scharenberg, B. C. Stringfellow, and F. Turkot, *Experimental results from high energy proton-nucleus interactions, critical phenomena, and the thermal liquid drop model of fragment production*, Phys. Rev. C **29** (1984), 508.

[HCLC89]   B. G. Harvey, H. J. Crawford, P. J. Lindstrom, and A. J. Cole, *Statistical decay of fragments from $C + {}^{12}C$, 2.1 GeV/nucleon*, Phys. Rev. C **39** (1989), 841.

[Hen05a]   V. Henzl, *Spectator response to the participant blast*, Ph.D. thesis, TU Prague, 2005.

[Hen05b]   D. Henzlova, *Systematic investigation of the isotopic distributions measured in the fragmentation of ${}^{124}Xe$ and ${}^{136}Xe$ projectiles*, Ph.D. thesis, TU Prague, 2005.

[HF52]   W. Hauser and H. Feshbach, *The inelastic scattering of neutrons*, Phys. Rev. **87** (1952), 366.

[HGS$^+$93]   E. Hanelt, A. Grewe, K.-H. Schmidt, T. Brohm, H.-G. Clerc, M. Dornik, M. Fauerbach, H. Geissel, A. Magel, G. Münzenberg, F. Nickel, M. Pfützner, C. Scheidenberger, M. Steiner, K. Sümmerer, B. Voss, M. Weber, J. Weckenmann, and C. Ziegler, *Momentum distributions of projectile fragments produced in the cold and hot fragmentation of relativistic ${}^{136}Xe$ and ${}^{197}Au$ projectiles*, Z. Phys. A **346** (1993), 43.

[HKL$^+$92]   J. Hubele, P. Kreutz, V. Lindenstruth, J. C. Adloff, M. Begemann-Blaich, P. Bouissou, G. Imme, I. Iori, G. J. Kunde, S. Leray, Z. Liu, U. Lynen, R. J. Meijer, U. Milkau, A. Moroni, W. F. J. Müller, C. Ngô, C. A. Ogilvie, J. Pochodzalla, G. Raciti, G. Rudolf, H. Sann, A. Schüttauf, W. Seidel, L. Stuttge, W. Trautmann, and A. Tucholski, *Statistical fragmentation of Au projectiles at E/A=600 MeV*, Phys. Rev. C **46** (1992), R1577.

[HSR$^+$]   D. Henzlova, K.-H. Schmidt, M. V. Ricciardi, A. Kelic, V. Henzl, P. Napolitani, L. Audouin, J. Benlliure, A. Boudard, E. Casarejos, J. E. Ducret, T. Enqvist, A. Heinz, A. Junghans, B. Jurado, A. Krasa, T. Kurtukian, S. Leray, M. F. Ordonez, J. Pereira, R. Pleskac, F. Rejmund, C. Schmitt, C. Stephan, L. Tassan-Got, C. Villagrasa, C. Volant, A. Wagner, and O. Yordanov, *Experimental investigation of the residues produced in the ${}^{136}Xe + Pb$ and ${}^{124}Xe + Pb$ fragmentation reactions at 1 A GeV*, arXiv:0801.3110v1.

[HSS75]   J. Hüfner, K. Schäfer, and B. Schürmann, *Abrasion-ablation in reactions between relativistic heavy ions*, Phys. Rev. C **12** (1975), 1888.

[JdJC+98]   A. R. Junghans, M. de Jong, H.-G. Clerc, A. V. Ignatyuk, G. A. Kudyaev, and K.-H. Schmidt, *Projectile-fragment yields as a probe for the collective enhancement in the nuclear level density*, Nucl. Phys. A **629** (1998), 635.

[Kar75]   Paul J. Karol, *Nucleus-nucleus reaction cross sections at high energies: Soft-spheres model*, Phys. Rev. C **11** (1975), 1203.

[Kar06]   V. A. Karnaukhov, *Nuclear multifragmentation and phase transitions in hot nuclei*, Physics of Particles and Nuclei **37** (2006), 165.

[KHSA07]   A. V. Karpov, R. M. Hiryanov, A. V. Sagdeev, and G. D. Adeev, *Dynamical treatment of fission fragment angular distribution*, J. Phys. G **34** (2007), 255.

[KLRM+95]   M. Kildir, G. La Rana, R. Moro, A. Brondi, E. Vardaci, A. D'Onofrio, D. Fessas, E. Perillo, V. Roca, M. Romano, F. Terrasi, G. Nebbia, G. Viesti, and G. Prete, *Ingoing-wave boundary condition versus optical model transmission coefficients: A systematic comparison with particle emission data*, Phys. Rev. C **51** (1995), 1873.

[Lin93]   V. Lindenstruth, *Dynamik der Multifragmentation*, Ph.D. thesis, Frankfurt-am-Main, 1993.

[MGV+94]   A. Magel, H. Geissel, B. Voss, P. Armbruster, T. Aumann, M. Bernas, B. Blank, T. Brohm, H.-G. Clerc, S. Czajkowski, H. Folger, A. Grewe, E. Hanelt, A. Heinz, H. Irnich, M. de Jong, A. Junghans, F. Nickel, M. Pfutzner, A. Piechaczek, C. Rohl, C. Scheidenberger, K.-H. Schmidt, W. Schwab, S. Steinhauser, K. Summerer, W. Trinder, H. Wollnik, and G. Munzenberg, *First spatial isotopic separation of relativistic uranium projectile fragments*, Nucl. Instr. Meth. B **94** (1994), 548.

[Mor75]   L.G. Moretto, *Statistical emission of large fragments: a general theoretical approach*, Nucl. Phys. A **247** (1975), 211.

[Mor89]   D.J. Morrissey, *Systematics of momentum distributions from reactions with relativistic ions*, Phys. Rev. C **39** (1989), 460.

[MS67]   W. D. Myers and W. J. Swiatecki, *Anomalies in nuclear masses*, Arkiv för Fysik **36** (1967), 343.

[MSW+71]   E. J. Moniz, I. Sick, R. R. Whitney, J. R. Ficenec, R. D. Kephart, and W. P. Trower, *Nuclear fermi momenta from quasielastic electron scattering*, Phys. Rev. Lett. **26** (1971), 445.

[NBD+87]   C. Ngô, R. Boisgard, J. Desbois, J. Nemeth, M. Barranco, and J. F. Mathiot, *From multifragmentation of nuclei to the quark-gluon plasma*, Nucl. Phys. A **471** (1987), 381.

[NPR00]   W. Nörenberg, G. Papp, and P. Rozmej, *Stability and instability of a hot and dilute nuclear droplet*, Eur. Phys. J. A **9** (2000), 327.

[NSB$^+$04]   P. Napolitani, K.-H. Schmidt, A. S. Botvina, F. Rejmund, L. Tassan-Got, and C. Villagrasa, *High-resolution velocity measurements on fully identified light nuclides produced in ^{56}Fe + hydrogen and ^{56}Fe + titanium*, Phys. Rev. C **70** (2004), 054607.

[NSTG$^+$07]   P. Napolitani, K.-H. Schmidt, L. Tassan-Got, P. Armbruster, T. Enqvist, A. Heinz, V. Henzl, D. Henzlova, A. Kelic, R. PleskaC, M. V. Ricciardi, C. Schmitt, O. Yordanov, L. Audouin, M. Bernas, A. Lafriaskh, F. Rejmund, C. Stephan, J. Benlliure, E. Casarejos, M. Fernandez Ordonez, J. Pereira, A. Boudard, B. Fernandez, S. Leray, C. Villagrasa, and C. Volant, *Measurement of the complete nuclide production and kinetic energies of the system ^{136}Xe+hydrogen at 1 GeV per nucleon*, Phys. Rev. C **76** (2007), 064609.

[NWH$^+$02]   J. B. Natowitz, R. Wada, K. Hagel, T. Keutgen, M. Murray, A. Makeev, L. Qin, P. Smith, and C. Hamilton, *Caloric curves and critical behavior in nuclei*, Phys. Rev. C **65** (2002), 034618.

[OBBB$^+$00]   T. Odeh, R. Bassini, M. Begemann-Blaich, S. Fritz, S. J. Gaff-Ejakov, D. Gourio, C. Groß, G. Immé, I. Iori, U. Kleinevoß, G. J. Kunde, W. D. Kunze, U. Lynen, V. Maddalena, M. Mahi, T. Möhlenkamp, A. Moroni, W. F. J. Müller, C. Nociforo, B. Ocker, F. Petruzzelli, J. Pochodzalla, G. Raciti, G. Riccobene, F. P. Romano, A. Saija, and M. Schnittker, *Fragment kinetic energies and modes of fragment formation*, Phys. Rev. Lett. **84** (2000), 4557.

[ODR79]   L. F. Oliveira, R. Donangelo, and J. O. Rasmussen, *Abrasion-ablation calculations of large fragment yields from relativistic heavy ion reactions*, Phys. Rev. C **19** (1979), 826.

[PBC$^+$07]   J. Pereira, J. Benlliure, E. Casarejos, P. Armbruster, M. Bernas, A. Boudard, S. Czajkowski, T. Enqvist, R. Legrain, S. Leray, B. Mustapha, M. Pravikoff, F. Rejmund, K.-H. Schmidt, C. Stephan, J. Taieb, L. Tassan-Got, C. Volant, and W. Wlazlo, *Isotopic production cross sections and recoil velocities of spallation-fission fragments in the reaction ^{238}U (1 A GeV) + d*, Phys. Rev. C **75** (2007), 014602.

[PMR$^+$95]   J. Pochodzalla, T. Möhlenkamp, T. Rubehn, A. Schüttauf, A. Wörner, E. Zude, M. Begemann-Blaich, Th. Blaich, H. Emling, A. Ferrero, C. Gross, G. Immé, I. Iori, G. J. Kunde, W. D. Kunze, V. Lindenstruth, U. Lynen, A. Moroni, W. F. J. Müller, B. Ocker, G. Raciti, H. Sann, C. Schwarz, W. Seidel, V. Serfling, J. Stroth, and W. Trautmann, *Probing the nuclear liquid-gas phase transition*, Phys. Rev. Lett. **75** (1995), 1040.

[RAB⁺06]   M. V. Ricciardi, P. Armbruster, J. Benlliure, M. Bernas, A. Boudard, S. Cza-jkowski, T. Enqvist, A. Kelic, S. Leray, R. Legrain, B. Mustapha, J. Pereira, F. Rejmund, K.-H. Schmidt, C. Stephan, L. Tassan-Got, C. Volant, and O. Yordanov, *Light nuclides produced in the proton-induced spallation of* ^{238}U *at 1 GeV*, Phys. Rev. C **73** (2006), 014607.

[REP⁺03]   M. V. Ricciardi, T. Enqvist, J. Pereira, J. Benlliure, M. Bernas, E. Casarejos, V. Henzl, A. Kelić, J. Taïeb, and K.-H. Schmidt, *Experimental indications for the response of the spectators to the participant blast*, Phys. Rev. Lett. **90** (2003), 212302.

[RFK⁺98]   J. Reinhold, J. Friese, H.-J. Körner, R. Schneider, K. Zeitelhack, H. Geissel, A. Magel, G. Münzenberg, and K. Sümmerer, *Projectile fragmentation of* ^{129}Xe *at Elab = 790A MeV*, Phys. Rev. C **58** (1998), 247.

[Ric04]   M. V. Ricciardi, *High-resolution measurements of light nuclides produced in 1 A GeV* ^{238}U*-induced reactions in hydrogen and in titanium*, Ph.D. thesis, Universidad de Santiago de Compostela, 2004.

[RMA⁺01]   F. Rejmund, B. Mustapha, P. Armbruster, J. Benlliure, M. Bernas, A. Boudard, J. P. Dufour, T. Enqvist, R. Legrain, S. Leray, K.-H. Schmidt, C. Stéphan, J. Taieb, L. Tassan-got, and C. Volant, *Measurement of isotopic cross sections of spallation residues in 800 A MeV* $^{197}Au + p$ *collisions*, Nucl. Phys. A **638** (2001), 540.

[RR97]   W. Reisdorf and H. G. Ritter, *Collective flow in heavy-ion collisions*, Annual Review of Nuclear and Particle Science **47** (1997), 663.

[RW92]   J. Richert and P. Wagner, *Transition rates and sequential decay of excited nuclei*, Z. Phys. A **341** (1992), 171.

[SBA⁺98]   W. Schwab, M. Bernas, P. Armbruster, S. Czajkowski, Ph. Dessagne, C. Donzaud, H. Geissel, A. Heinz, C. Kozhuharov, C. Miehé, G. Münzen-berg, M. Pfützner, C. Stéphan, K. Sümmerer, L. Tassan-Got, and B. Voss, *Fission of highly excited fragments from collisions of 750 AMeV* ^{238}U*-ions on* ^{208}Pb, Eur. Phys. J. A **2** (1998), 179.

[SBC⁺92]   M. Steiner, K. Blasche, H.-G. Clerc, H. Eickhoff, B. Franczak, H. Geissel, G. Munzenberg, K.-H. Schmidt, H. Stelzer, and K. Summerer, *Preliminary measurements of sis 18 beam parameters*, Nucl. Instr. Meth. A **312** (1992), 420.

[SBC⁺93]   K.-H. Schmidt, T. Brohm, H.-G. Clerc, M. Dornik, M. Fauerbach, H. Geissel, A. Grewe, E. Hanelt, A. Junghans, A. Magel, W. Morawek, G. Münzenberg, F. Nickel, M. Pfützner, C. Scheidenberger, K. Sümmerer, D. Vieira, B. Voss, and C. Ziegler, *Distribution of Ir and Pt isotopes produced as fragments of*

1AGeV ^{197}Au projectiles: a thermometer for peripheral nuclear collisions, Phys. Lett. B **300** (1993), 313.

[SDL01]   L. Shi, P. Danielewicz, and R. Lacey, *Spectator response to the participant blast*, Phys. Rev. C **64** (2001), 034601.

[Ser47]   R. Serber, *Nuclear reactions at high energies*, Phys. Rev. **72** (1947), 1114.

[SFF$^+$02]   A. Stolz, T. Faestermann, J. Friese, P. Kienle, H.-J. Körner, M. Münch, R. Schneider, E. Wefers, K. Zeitelhack, K. Sümmerer, H. Geissel, J. Gerl, G. Münzenberg, C. Schlegel, R. S. Simon, H. Weick, M. Hellström, M. N. Mineva, and P. Thirolf, *Projectile fragmentation of ^{112}Sn at Elab = 1A GeV*, Phys. Rev. C **65** (2002), 064603.

[SKW$^+$96]   A. Schüttauf, W. D. Kunze, A. Worner, M. Begemann-Blaich, Th. Blaich, D. R. Bowman, R. J. Charity, A. Cosmo, A. Ferrero, C. K. Gelbke, C. Gro[ss], W. C. Hsi, J. Hubele, G. Imme, I. Iori, J. Kempter, P. Kreutz, G. J. Kunde, V. Lindenstruth, M. A. Lisa, W. G. Lynch, U. Lynen, M. Mang, T. Mohlenkamp, A. Moroni, W. F. J. Muller, M. Neumann, B. Ocker, C. A. Ogilvie, G. F. Peaslee, J. Pochodzalla, G. Raciti, F. Rosenberger, Th. Rubehn, H. Sann, C. Schwarz, W. Seidel, V. Serfling, L. G. Sobotka, J. Stroth, L. Stuttge, S. Tomasevic, W. Trautmann, A. Trzcinski, M. B. Tsang, A. Tucholski, G. Verde, C. W. Williams, E. Zude, and B. Zwieglinski, *Universality of spectator fragmentation at relativistic bombarding energies*, Nucl. Phys. A **607** (1996), 457.

[SRBE02]   K.H. Schmidt, M.V. Ricciardi, A.S. Botvina, and T. Enqvist, *Production of neutron-rich heavy residues and the freeze-out temperature in the fragmentation of relativistic ^{238}U projectiles determined by the isospin thermometer*, Nucl. Phys. A **710** (2002), 157.

[SSB$^+$00]   K. H. Schmidt, S. Steinhauser, C. Bockstiegel, A. Grewe, A. Heinz, A. R. Junghans, J. Benlliure, H. G. Clerc, M. de Jong, J. Muller, M. Pfutzner, and B. Voss, *Relativistic radioactive beams: A new access to nuclear-fission studies*, Nucl. Phys. A **665** (2000), 221.

[Sto]   R. G. Stokstad, *The use of statistical models in heavy-ion reactions studies*, Treatise on Heavy-Ion Science vol. 3.

[Swi83]   W. J. Swiatecki, *Note on nuclear disintegration widths*, Aust. J. Phys. **36** (1983), 641.

[TBBB$^+$07]   W. Trautmann, R. Bassini, M. Begemann-Blaich, A. Ferrero, S. Fritz, S. J. Gaff-Ejakov, C. Gross, G. Imme, I. Iori, U. Kleinevoss, G. J. Kunde, W. D. Kunze, A. Le Fevre, V. Lindenstruth, J. Łukasik, U. Lynen, V. Maddalena, M. Mahi, T. Mohlenkamp, A. Moroni, W. F. J. Muller, C. Nociforo, B. Ocker,

T. Odeh, H. Orth, F. Petruzzelli, J. Pochodzalla, G. Raciti, G. Riccobene, F. P. Romano, Th. Rubehn, A. Saija, H. Sann, M. Schnittker, A. Schüttauf, C. Schwarz, W. Seidel, V. Serfling, C. Sfienti, A. Trzcinski, A. Tucholski, G. Verde, A. Worner, Hongfei Xi, and B. Zwieglinski ALADIN Collaboration, *Thermal and chemical freeze-out in spectator fragmentation*, Phys. Rev. C **76** (2007), 064606.

[TSC+03] J. Taieb, K.-H. Schmidt, E. Casarejos, L. Tassan-Got, P. Armbruster, J. Benlliure, M. Bernas, A. Boudard, E. Casarejos, S. Czajkowski, T. Enqvist, R. Legrain, S. Leray, B. Mustapha, M. Pravikoff, F. Rejmund, C. Stephan, C. Volant, and W. Wlazlo, *Evaporation residues produced in the spallation reaction $^{238}U + p$ at 1 A GeV*, Nucl. Phys. A **724** (2003), 413.

[VBC+95] B. Voss, T. Brohm, H.-G. Clerc, A. Grewe, E. Hanelt, A. Heinz, M. de Jong, A. Junghans, W. Morawek, C. Rohl, S. Steinhauser, C. Ziegler, K.-H. Schmidt, K.-H. Behr, H. Geissel, G. Munzenberg, F. Nickel, C. Scheidenberger, K. Summerer, A. Magel, and M. Pfutzner, *The scintillation-detector equipment of the GSI projectile-fragment separator*, Nucl. Instr. Meth. A **364** (1995), 150.

[VCBD+07] C. Villagrasa-Canton, A. Boudard, J.-E. Ducret, B. Fernandez, S. Leray, C. Volant, P. Armbruster, T. Enqvist, F. Hammache, K. Helariutta, B. Jurado, M. V. RIcciardi, K.-H. Schmidt, K. Suemmerer, F. Vives, O. Yordanov, L. Audouin, C.-O. Bacri, L. Ferrant, P. Napolitani, F. Rejmund, C. Stephan, L. Tassan-Got, J. Benliure, E. Casarejos, M. Fernandez-Ordonez, J. Pereira, S. Czajkowski, D. Karamanis, M. Pravikoff, J. S. George, R. A. Mewaldt, N. Yanasak, M. Wiedenbeck, J. J. Connell, T. Faestermann, A. Heinz, and A. Junghans, *Spallation residues in the reaction $^{56}Fe + p$ at 0.3 A, 0.5 A, 0.75 A, 1.0 A, and 1.5 A GeV*, Phys. Rev. C **75** (2007), 044603.

[VH93] R. Vandenbosch and J. R. Huizenga, *Nuclear fission*, Academic Press, New York, 1993.

[WDD+94] M. Weber, C. Donzaud, J.P. Dufour, H. Geissel, A. Grewe, D. Guillemaud-Mueller, H. Keller, M. Lewitowicz, A. Magel, A.C. Mueller, G. Munzenberg, F. Nickel, M. Pfutzner, A. Piechaczek, M. Pravikoff, E. Roeckl, K. Rykaczewski, M.G. Saint-Laurent, I. Schall, C. Stephan, K. Summerer, L. Tassan-Got, D.J. Vieira, and B. Voss, *Longitudinal momenta and production cross-sections of isotopes formed by fragmentation of a 500 AMeV ^{86}Kr beam*, Nucl. Phys. A **578** (1994), 659.

[WE40] V. F. Weisskopf and D. H. Ewing, *On the yield of nuclear reactions with heavy elements*, Phys. Rev. **57** (1940), 472 ; see also erratum in Phys. Rev. 57 (1940) 935.

[WSC76]   B. D. Wilkins, E. P. Steinberg, and R. R. Chasman, *Scission-point model of nuclear fission based on deformed-shell effects*, Phys. Rev. C **14** (1976), 1832.

[WSP⁺78]   G.D. Westfall, R.G. Sextro, A.M. Poskanzer, A.M. Zebelman, G.W. Butler, and E.K. Hyde, *Energy spectra of nuclear fragments produced by high energy protons*, Phys. Rev. C **17** (1978), 1368.

[YF79]   Y. Yariv and Z. Fraenkel, *Intranuclear cascade calculation of high-energy heavy-ion interactions*, Phys. Rev. C **20** (1979), 2227.

[ZLD07]   Y. Zhang, Z. Li, and P. Danielewicz, *In-medium nn cross sections determined from the nuclear stopping and collective flow in heavy-ion collisions at intermediate energies*, Phys. Rev. C **75** (2007), 034615.